DESIGN OPTIMIZATION OF COMPOSITE I-BEAM WING SPARS WITH CORRUGATED WEB

by

Doğan Çok

B.S., Mechanical Engineering, Doğuş University, 2014

Submitted to the Institute for Graduate Studies in
Science and Engineering in partial fulfillment of
the requirements for the degree of
Master of Science

Graduate Program in Mechanical Engineering

Boğaziçi University

2019

DESIGN OPTIMIZATION OF COMPOSITE I-BEAM WING SPARS WITH CORRUGATED WEB

APPROVED BY:

Prof. Fazıl Önder Sönmez ..... (Thesis Supervisor)

Prof. Halit Süleyman Türkmen .....

Assoc. Prof. Şebnem Özüpek .....

DATE OF APPROVAL: 15.01.2019

ACKNOWLEDGEMENTS

I would like to express gratitude to my thesis advisor Prof. Fazıl Önder Sönmez for his guidance and support throughout my thesis study.

I would also like to thank to Turkish Aerospace Industries for providing information required for this study.

Finally, I would like to thank to my family for all their help and support during my studies.

ABSTRACT

DESIGN OPTIMIZATION OF COMPOSITE I-BEAM WING SPARS WITH CORRUGATED WEB

The main goal of this study is to develop a methodology for optimum structural design of composite I-beam wing spars with wavy corrugated web to minimize mass and investigate their mechanical behaviors under aerodynamic loading conditions. For this purpose, Hürkuş Advanced Training Plane is selected as the plane model for which the spar is optimally designed. Accordingly, the wing dimensions are selected and the loads on the spar are evaluated. The lift as a non-uniformly distributed transverse load is calculated considering aircraft mass and directly applied to the spar. IM7/8552 carbon-fiber reinforced composite material is selected for the model because of its high strength with low density. Buckling analysis is carried out to determine the failure load levels considering that the most critical failure mode in I-beam spars is web buckling due to shear loads. Tsai-Wu criterion is used to predict static failure. By using ANSYS Parametric Design Language (APDL), codes are developed to implement the optimization algorithms and carry out structural analyses to determine the maximum load capacity of the spar. The web is designed like a multi-period wave with four parameters. These are the initial wavelength, the wavelength increment rate, the initial amplitude and the final amplitude. The shape of the web is defined by spline curves passing through key points having coordinates determined by the above-mentioned four parameters. The objective function to be minimized is chosen as the mass of the spar with the buckling strength constraint. The optimum shape of the web is found using modified simulated annealing algorithm, which is a stochastic global search algorithm. A considerable improvement is obtained in mechanical strength with much less use of material compared to the conventional wing spars.

ÖZET

DALGA PROFİLLİ KOMPOZİT KANAT ANA I-KİRİŞLERİNİN TASARIM ENİYİLEMESİ

Bu çalışmanın ana hedefi, dalga profilli kompozit uçak kanadı ana I-kirişleri için, aerodinamik yükleme koşulları altında kütle azaltımı amacıyla bir en iyi yapısal tasarım metodolojisi geliştirmek ve kirişlerin bu şartlar altındaki mekanik davranışlarını incelemektir. Bu amaçla, kanat ana kirişinin en iyi şekilde tasarlanması için model uçak olarak Hürkuş Gelişmiş Eğitim Uçağı seçilmiştir. Buna göre kanat ölçüleri seçilmiş ve kiriş üzerindeki yükler hesaplanmıştır. Uçak kütlesi dikkate alınarak hesaplanan kaldırma yükü, düzgün olmayan değişken bir şekilde dağılı yük olarak, kanat ana kiriş modeline uygulanmıştır. Malzeme olarak, yüksek mukavemetine karşın düşük yoğunluğu sebebiyle, IM7/8552 karbon fiber destekli kompozit seçilmiştir. Hata yükü seviyelerini belirlemek için, I-kanat kirişlerindeki en kritik hata modunun bağlantı levhasında oluşan kayma burkulması olduğu hesaba katılarak burkulma analizi uygulanmıştır. Statik hatanın belirlenmesi için Tsai-Wu kriteri kullanılmıştır. ANSYS Parametric Design Language (APDL) kullanılarak, eniyileme algoritmalarını uygulamak için ve kanat ana kirişinin maksimum yük kapasitesini belirlemek amacıyla yapısal analiz gerçekleştirmek için kodlar geliştirilmiştir. Bağlantı levhası, dört değişkenle çok periyotlu dalga gibi tasarlanmıştır. Bunlar ilk dalga boyu, dalga boyu artış oranı, ilk genlik ve son genliktir. Bağlantı levhasının şekli, yukarıda bahsi geçen dört değişkenle belirlenen koordinatlara sahip kilit noktalardan geçen eğriler vasıtasıyla tanımlanmıştır. Azaltılacak gaye fonksiyonu, burkulma dayanımı sınırlamasıyla, kütle olarak seçilmiştir. En iyi bağlantı levhası şekli, bir stokastik global arama algoritması olan, değiştirilmiş benzetilmiş tavlama algoritması kullanılarak bulunmuştur. Geleneksel kanat ana kirişleri ile kıyaslandığında, mekanik dayanımda, çok daha az malzeme kullanımı ile kayda değer gelişme elde edilmiştir.

TABLE OF CONTENTS

ACKNOWLEDGEMENTS iii
ABSTRACT iv
ÖZET v
LIST OF FIGURES viii
LIST OF TABLES xiv
LIST OF SYMBOLS xvi
LIST OF ACRONYMS/ABBREVIATIONS xxi
1. INTRODUCTION 1
1.1. Design and Material Types of Spars 2
1.2. Literature Review 4
1.3. Scope of The Thesis 7
2. THEORETICAL BACKGROUND 9
2.1. I-Beam Wing Spars 9
2.1.1. Failure Behaviors of I-Beam Wing Spars 10
2.2. Laminated Composite Materials 12
2.2.1. Critical Failure Mechanisms of Laminated Composites 12
2.2.2. Failure Criteria of Laminated Composites 13
2.3. Finite Element Method 17
2.3.1. Arc-Length Method 19
2.4. Optimization Methods 20
2.4.1. Modified Simulated Annealing 22
3. DESIGN PARAMETERS OF THE SPAR BEAM 23
3.1. General Wing Spar Design 23
3.2. Wing Spar Web Design 26
4. FINITE ELEMENT MODELING 28
4.1. Parts of the Spar Model 28
4.2. Selection of Element Types 29
4.3. Model Verification 30
4.4. Definition of Materials and Local Coordinate Systems 41

4.5. Boundary and Loading Conditions 48
4.5.1. Boundary Conditions 49
4.5.2. Loading Condition 51
5. OPTIMIZATION PROCESS 54
5.1. Coordinates of the Key Points 55
5.2. Optimization Algorithm 58
6. RESULTS AND DISCUSSION 64
6.1. Spar with Flat Web 64
6.2. Spars with Corrugated Web 67
6.2.1. Model with 1.5 mm Web Thickness 68
6.2.2. Model with 1.0 mm Web Thickness 72
6.3. Comparison of the Models 76
7. CONCLUSION 79
7.1. Future Work Recommendations 80
REFERENCES 81
APPENDIX A: SHEAR STRENGTH OF WAVY CORRUGATED WEBS . . 93
APPENDIX B: BEAMS UNDER THREE-POINT BENDING 96
APPENDIX C: FLOWCHART OF THE OPTIMIZATION ALGORITHM . . 101
APPENDIX D: MANUFACTURING 102

LIST OF FIGURES

Figure 1.1. Schematic representation of aircraft wing spars [3]. 1

Figure 1.2. Three general types of wing constructions with different number of spar [8]. 2

Figure 1.3. Typical wooden aircraft wing spar cross-sections [9]. 3

Figure 1.4. Some examples of metal aircraft wing spar designs [9]. 3

Figure 1.5. An illustration of an I-beam wing spar with sine wave web [9]. . . 4

Figure 2.1. Schematic representation of the stress distributions of an I-beam under bending load. (a) Normal and (b) shear stress. 9

Figure 2.2. Shear force diagram of a beam under uniformly distributed load [64]. 10

Figure 2.3. Some failure types of I-beams under bending. (a) Global buckling [65], (b1) local compressive flange buckling [66] and (b2) local shear web buckling [67]. 10

Figure 2.4. Schematic representation of a general wing structure [68]. 11

Figure 2.5. Schematic representation of the most common failures of laminated composite materials [69]. 13

Figure 2.6. A stress-strain graph example with elastic and plastic regions [76]. 18

Figure 2.7. Unstable systems under (a) load control (snap-through instability), (b) displacement control (Snap-Back Instability) and (c) both load and displacement control [77]. 19

Figure 2.8. A schematic representation of the Arc-Length method iterations. u and Λ represent a normalized displacement and the load increment parameter respectively [77]. 20

Figure 2.9. A schematic representation of a gradient-based optimization procedure on graph of a function [78]. 21

Figure 2.10. An example of a graph of a function with a global and local minimum and maximum points [78]. 21

Figure 3.1. Isometric view of a conventional I-beam wing spar with constantly corrugated web. 24

Figure 3.2. Various views of a spar beam. (a) Right view, (b) front view and (c) back view. 25

Figure 3.3. Spline curve of the web shape with all parameters. 27

Figure 4.1. Parts of the spar model. (A) Top flange, (B) web, (C) bottom flange and (D) free end cover. 28

Figure 4.2. Geometry, node locations, and the element coordinate system for SHELL181 [84]. 29

Figure 4.3. Node-to-surface bonded contact elements. 30

Figure 4.4. Two example of finite element models developed by Kiymaz *et al.* with 0.5 m and 1.0 m heights and web holes [85]. 31

Figure 4.5. A sample meshed model with boundary and loading conditions. . 35

Figure 4.6. A model with the buckled web from (a) isometric and (b) right views with displacement values in meters in the x-direction. 36

Figure 4.7. The final meshed model with a close view. 41

Figure 4.8. Schematic representation of a positive fiber orientation angle (θ) in relation to the reference axes [89]. 43

Figure 4.9. Display of the local coordinate systems at the fixed root from (a) isometric, (b) right and (c) top views. 44

Figure 4.10. Stacking sequences of each ply group of (a) the flanges and (b) the web. 47

Figure 4.11. Zero displacement boundary condition in the x-direction along the length. 50

Figure 4.12. Fixed boundary condition in all directions for displacement and rotation at the wing root. 50

Figure 4.13. The lift load distribution from the right view. 52

Figure 4.14. The loads applied on nodes at the center of the bottom flange from fixed root side with isotropic view. 53

Figure 4.15. An example of a buckled deformed model from isometric view with displacement values in meters in the x-direction. 53

Figure 5.1. Patterns of key points on the spline curve from (a) left and (b) top views. 54

Figure 6.1. The spar with flat web. 65

Figure 6.2. The distribution of the displacement in meters in the x-direction of the buckled spar with 4 mm-thick web from (a) isometric and (b) right views. 66

Figure 6.3. The distribution of Tsai-Wu index of the buckled spar with 4 mm-thick flat web from (a) isometric and (b) right views. 67

Figure 6.4. Initial design of the spar. 68

Figure 6.5. The last design of the spar with 1.5 mm-thick corrugated web with a close view from the fixed side. 69

Figure 6.6. The distribution of the displacement in meters in the x-direction of the spar with 1.5 mm-thick web under 112 kN from (a) isometric and (b) right views with closer one. 70

Figure 6.7. The distribution of Tsai-Wu index of the spar with 1.5 mm-thick web under 112 kN from (a) isometric and (b) right views with closer one. 71

Figure 6.8. The last design of the spar with 1.0 mm-thick corrugated web with a close view from the fixed side. 73

Figure 6.9. The distribution of the displacement in meters in the x-direction of the spar with 1.0 mm-thick web under 112 kN from (a) isometric and (b) right views with closer one. 74

Figure 6.10. The distribution of Tsai-Wu index of the spar with 1.0 mm-thick web under 112 kN from (a) isometric and (b) right views with closer one. 75

Figure 6.11. Comparison of the web masses of the four spars. 77

Figure 6.12. The change of total mass of the four spars. 78

Figure A.1. Critical web dimensions [86]. 94

Figure B.1. Shear-moment diagram of beams under three-point bending with force applied from the center [92]. 96

Figure B.2. Sectional shear force and moment of the beam after being cut from the region I. 98

Figure B.3. Sectional shear force and moment of the beam after being cut from the region II. 99

Figure C.1. Flowchart of the optimization algorithm [93]. 101

Figure D.1. All manufacturing phases of a carbon-fiber reinforced composite I-beam with corrugated web [94]. 102

Figure D.2. Vacuum bag setup for consolidation process [94]. 103

Figure D.3. Press forming process diagram [94]. 103

Figure D.4. Components of the beam [94]. 104

Figure D.5. Final product [94]. 104

LIST OF TABLES

Table 3.1. General determined design dimensions. 26

Table 3.2. Maximum and minimum limits of the web shape parameters. . . . 27

Table 4.1. Design features of the model selected for verification. 32

Table 4.2. Buckling analysis results for different ranges of the multiplier for the arc-length radius. 33

Table 4.3. Buckling analysis results for different vertical mesh sizes of the web. 37

Table 4.4. Buckling analysis results for various horizontal mesh sizes of the web. 38

Table 4.5. Buckling analysis results for different global mesh sizes of the flanges, end cover plates and central stiffener. 39

Table 4.6. Buckling analysis results for slightly changing horizontal mesh sizes of the web. 40

Table 4.7. Determined mesh sizes. 40

Table 4.8. Mechanical properties of unidirectional IM7/8552 laminae [89]. . . 42

Table 4.9. Load factor results of the spar designed with dimensions as average of design limits for various material properties. 45

Table 4.10. Load factor results of the spar with the most densely curved web for various material properties. 46

Table 4.11. Selected material configuration. 47

Table 4.12. Mesh verification for the spar beam made of orthotropic material. . 48

Table 6.1. Wave parameter values of the spar with 1.5 mm-thick corrugated web. 69

Table 6.2. Wave parameter values of the spar with 1.0 mm-thick corrugated web. 72

Table 6.3. Total and web masses of the spar beams used in this thesis. 76

LIST OF SYMBOLS

a	Amplitude
a_1	Initial amplitude
$a_{1,max}, a_{1,min}$	Maximum and minimum initial amplitudes
a'_1	Initial amplitude with a new value
$a_{1,ini}$	Initial value of the initial amplitude
a_f	Final amplitude
$a_{f,max}, a_{f,min}$	Maximum and minimum final amplitudes
a'_f	Final amplitude with a new value
$a_{f,ini}$	Initial value of the final amplitude
A	Perpendicular changing distance of the top flange from the fixed root in the y-direction
A_0	Perpendicular distance between the upper edges of the free end and the fixed root in the y-direction
A_{obj}	Acceptability of the objective function
B	Perpendicular changing distance of the bottom flange from the fixed root in the y-direction
B_0	Perpendicular distance between the lower edges of the free end and the fixed root in the y-direction
c_r	Reduction coefficient
C	Decrement of the amplitude
C_0	Perpendicular distance between the third key points of the first and final periods in the x-direction
$C_{A,k}$	Number of accepted configuration in the kth Markov chain
$C_{N,k}$	Number of newly tried configuration in the kth Markov chain
E_1	Longitudinal modulus
E_2	Transverse modulus
E_3	Through-thickness modulus
f	Final period number
f_{best}	The best objective function value

f_{obj}	Objective function value
f_{wst}	Objective function value of a randomly chosen configuration among the worst ones
F_0	Force applied to the first node
F_a	Applied load
F_c	Load the structure is able to carry
F_s	Load applied on the spar
F_t	Total critical lift load
$F(z_i)$	Varying force depending on the node location
g	Gravitational acceleration
g_L	g limit
G_{12}	In-plane shear modulus
G_{13}	Transverse shear modulus
G_{23}	Through-thickness shear modulus
h_B	Bottom height of the free end
$h_{E,t}$	Total height of the free end
$h_{R,t}$	Total height of the fixed root
i	Wavelength increment rate
i_{max}, i_{min}	Maximum and minimum wavelength increment rates
i'	Wavelength increment rate with a new value
i_{ini}	Initial value of the wavelength increment rate
L	Length of the spar
$L_{M,k}$	Length of the kth Markov chain
$L_{M,min}$	Minimum length of the Markov chain
LF	Load factor
m	Mass
n	Total number of variables
N	The number of configurations of each configuration set
N_{wst}	The number of worst configurations of a configuration set
p	Period number
P	Penalty value

r	Randomly chosen number between -1.0 and 1.0
R	Randomly chosen number between 0.0 and 1.0
$R_{A,k}$	Ratio of the numbers of accepted and newly tried configurations of the kth Markov chain
$R_{s,k}$	Ratio of the initial and the current step sizes kth Markov chain
$s_{w1,k}$	Initial wavelength step size of the kth Markov chain
$s_{w1}, s_i, s_{a1}, s_{af}$	Step sizes of the parameters
$s'_{w1}, s'_i, s'_{a1}, s'_{af}$	Step sizes of the parameters with new values
$s_{w1,ini}, s_{i,ini},$ $s_{a1,ini}, s_{af,ini}$	Initial step sizes of the parameters
$S_{w1}, S_i, S_{a1}, S_{af}$	Change amounts of the parameters
t_k	Temperature reduction factor of the kth Markov chain
t_{max}, t_{min}	Maximum and minimum temperature reduction factors
t_B, t_T	Thicknesses of the bottom and the top flanges
T_k	Temperature of the kth Markov chain
T_0	Initial temperature
u	Displacement
V_f	Fiber volume fraction
w	Wavelength
w_1	Initial wavelength
$w_{1,max}, w_{1,min}$	Maximum and minimum initial wavelengths
$w_{1,ini}$	Initial value of the initial wavelength
w'_1	Initial wavelength with a new value
w_p	Wavelength of the pth period
W_A	Weight of the aircraft
$x_{p,1}, x_{p,2}, x_{p,3}, x_{p,4}$	x coordinates of the key points of the current period
y_B	y coordinates of the key points on the bottom flange
y_T	y coordinates of the key points on the top flange
z	z coordinates of the key points
z_i	Changing location in the z-direction of the nodes force applied
$z_{p,1}, z_{p,2}, z_{p,3}, z_{p,4}$	z coordinates of the key points of the pth period

z'	Perpendicular distance between the third key points of the first period and current period in the z-direction
z''	Perpendicular distance between the third key points of the first period and final period in the z-direction
α	Slope angle of the top flange
β	Slope angle of the bottom flange
γ_{12}^{u}	In-plane shear failure strain
γ_{13}^{u}	Transverse shear failure strain
γ_{23}^{u}	Through-thickness shear failure strain
γ_6	Shear strain
γ_6^u	Ultimate allowable magnitude of shear strain
δ_1	First stopping criterion
δ_2	Second stopping criterion
Δl	Radius of the arc-length circle
Δu	Change of displacement
$\Delta\lambda$	Change of load
ε_1	Normal strain in fiber direction
ε_2	Normal strain in transverse direction
ε_{1t}	Longitudinal tensile failure strain
ε_{1c}	Longitudinal compressive failure strain
ε_{2t}	Transverse tensile failure strain
ε_{2c}	Transverse compressive failure strain
ε_{3t}	Through-thickness tensile failure strain
ε_{3c}	Through-thickness compressive failure strain
θ	Slope angle of an imaginary straight line passing through the key points of the amplitudes
λ	Load
ν_{12}	Major Poisson's ratio
ν_{13}	Major transverse Poisson's ratio
ν_{23}	Through-thickness Poisson's ratio
σ_1	Normal stress in fiber direction

σ_2	Normal stress in transverse direction
σ_6	Shear stress
σ_{1c}	Longitudinal compressive strength
σ_{1t}	Longitudinal tensile strength
σ_{2c}	Transverse compressive strength
σ_{2t}	Transverse tensile strength
σ_{3c}	Through-thickness compressive strength
σ_{3t}	Through-thickness tensile strength
σ_6^u	Ultimate allowable magnitude of shear stress
σ_c	Compressive stress
σ_t	Tensile stress
τ_{12}	In-plane shear strength
τ_{13}	Transverse shear strength
τ_{23}	Through-thickness shear strength

LIST OF ACRONYMS/ABBREVIATIONS

2D	Two dimensional
3D	Three dimensional
APDL	ANSYS Parametric Design Language
CFRP	Carbon-fiber reinforced polymer
DGAC	Directorate General for Civil Aviation
FRP	Fiber-reinforced polymer
GA	Genetic algorithm
GPa	Gigapascal
kg	Kilogram
kN	Kilonewton
m	Meter
min	Minute
mm	Milimeter
μm	Micrometer
MPa	Megapascal
MTOW	Maximum take-off weight
SA	Simulated annealing
SF	Safety factor
TAI	Turkish Aerospace Industries
TS	Tabu search

1. INTRODUCTION

Aviation is one of the most important means of transportation in today's global world. The number of passengers using airplanes has been increasing for the last 50 years [1]. Design of aircraft has been improving for years to satisfy the growing demand in cheaper and safer ways.

One of the most vital parts of an aircraft is wings, which contain fuel tanks and carry an important part of loads in various situations including take-off, climb, cruise, loiter, landing and touch-down [2]. In order to those loads, wings have structural parts called ribs and spars. This study focuses on spars particularly. A schematic representation of aircraft wing spars can be seen in Figure 1.1.

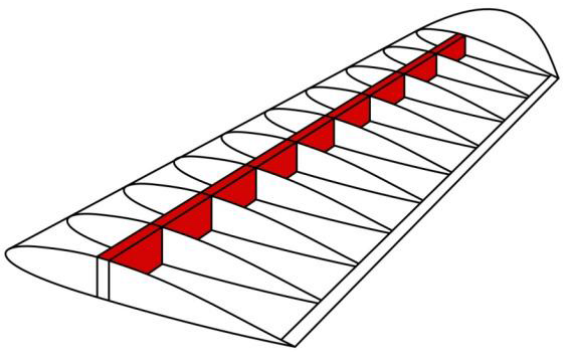

Figure 1.1. Schematic representation of aircraft wing spars [3].

Wing spars are the major load carrying structures of the wings. They support the flight loads and the weight of the wing while on the ground. Spars are fixed to fuselage; they extend through the wing to the free end. They can be placed perpendicularly or with an angle to the aircraft body [4].

The loads acting on wings can generally be classified as follows:

- Upward bending during flight due to the lift effect of the air which can be partially balanced by the weight of fuel tanks in the wing.
- Downward bending during stationary phase due to the weight of fuel tanks and engines if they are placed on the wings.
- Drag forces depending on the speed of wind, aircraft and its inertia.
- Rolling inertia effects.
- Chord wise twisting loads by virtue of aerodynamics effects at high speeds [5, 6].

Upward and downward bends and rolling inertia effects are predominantly carried by spars. On the other hand, drag forces and chord wise twisting loads are mainly carried by wing skin and ribs.

1.1. Design and Material Types of Spars

The main design parameters of spars are their geometry, number, location, and material. Position of spars considerably affects the stiffness, weight and flutter speed [7]. Use of different numbers of spars is possible as shown in Figure 1.2.

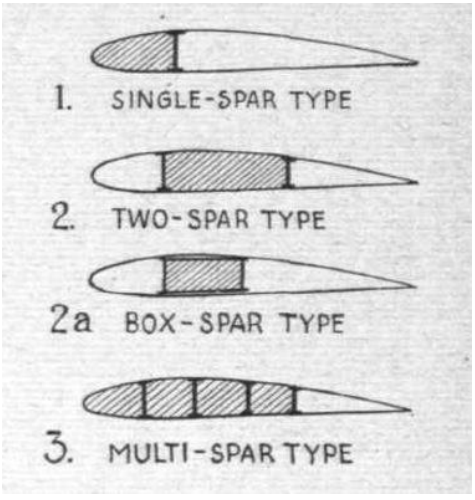

Figure 1.2. Three general types of wing constructions with different number of spar [8].

Single-spar wings are mostly used in light aircraft like sailplanes and multi-spar wings are used in heavy aircraft like air freighters in general. Two-spar wing types are usually used in single-engine or small commercial aeroplanes.

Spars may be made of various shapes and materials for specific purposes. Wood is used in small planes due to its ultra-low cost and weight; metals like aluminum alloy or titanium are used due to their high strength and relatively low weight; composites, especially carbon-fiber reinforced polymers, are used because of their very high strength-to-weight ratio in various-sized planes. Wooden ones are frequently used in five different designs as presented in Figure 1.3.

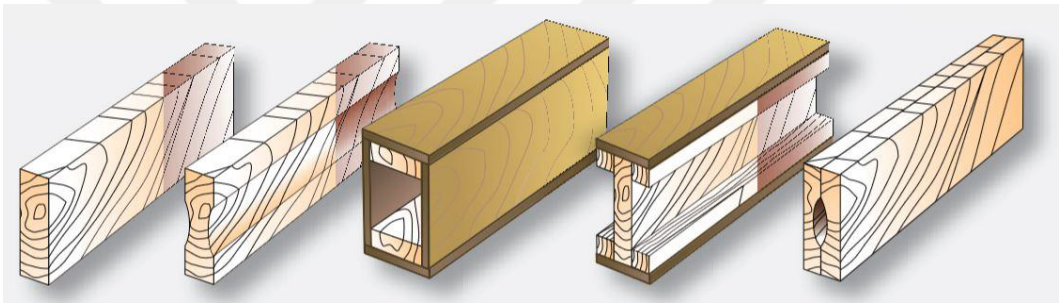

Figure 1.3. Typical wooden aircraft wing spar cross-sections [9].

Metal spars have more shape design possibilities than the wooden ones thanks to their manufacturability in many ways. Various designs can be seen in Figure 1.4 like I-beam with or without holes, stiffened I-beam, and truss-structured spars.

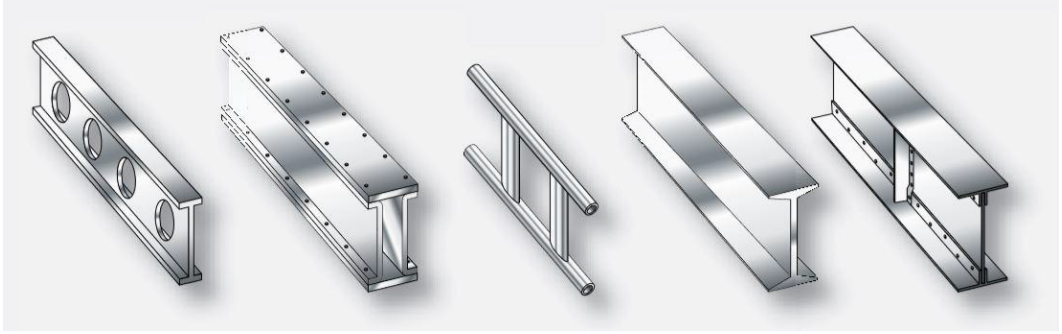

Figure 1.4. Some examples of metal aircraft wing spar designs [9].

Composite materials pose difficulties in manufacturing which leads to some design restrictions. Thus, composite spars are generally made in the shape of I-beam with a straight or corrugated web without stiffeners or holes. Figure 1.5 illustrates a composite I-beam spar with corrugated web.

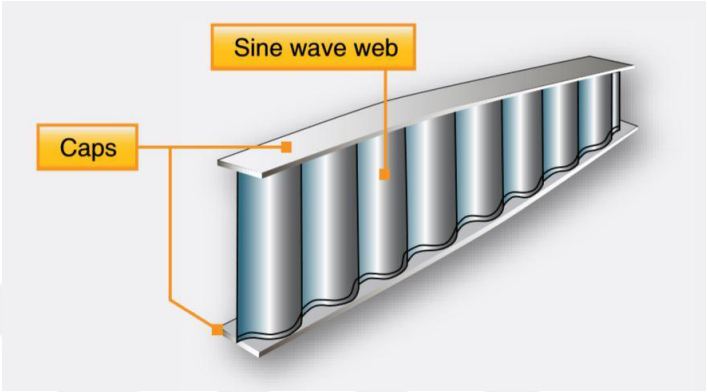

Figure 1.5. An illustration of an I-beam wing spar with sine wave web [9].

1.2. Literature Review

There are many studies in the literature on aircraft wings and spars having different features.

Most of them considered conventional spars, which can be classified according to their number, shape, and material. In the previous studies, single spars [10–15], two spars [2, 7, 16–24], wing boxes [25, 26], and multi spars [6, 25, 27–32] were used. Different cross sectional shapes were considered, I-shapes with flat web [2, 5, 10, 12, 13, 15, 16, 19, 22, 24, 27, 29, 31–39], C-shapes [2, 6, 25, 27–32, 40, 41], bar shapes [11, 23, 34], rectangular [28, 42, 43] and tubular shapes [14]. Different materials were used like wood [34], aluminum alloys [2,6,10,15,18,20–23,29,32,33,35–38,40,44], and steels [16], and glass-fiber reinforced polymers [5], carbon-fiber reinforced polymers [12–14, 19, 24, 26–28, 39, 41–43, 45], and for the web sandwich composites [12, 13, 27].

Some nonconventional spars were also considered in previous studies [45–61] for specific purposes such as span morphing to fly faster and more manoeuvrable with a

high aerodynamic performance, energy harvesting for longer flight distances with the same or less fuel, and new designs for getting stronger wings like curvilinear spars and ribs (SpaRibs).

Few of the aforementioned studies aimed optimum design of spar beams. One of them is carried out by Afifi *et al.* [44]. They developed a new approximation method of local and global ones including series expansion, reduced basis vector, matrix factorization, and Gram-Schmidt orthonormalization to determine the optimum shape design for tapered C-shaped wing spar made of an aluminum alloy. The spar was considered as a mass-spring system to simplify the problem for optimization in terms of its thickness, cap width and height. The masses were placed between the springs like a distributed load.

Bhachu *et al.* [31] developed a probabilistic cost model which explicitly models performance cost with manufacturing and quality tolerances for damage-tolerant aircraft structures. A wing model with I and C-shaped spars made of aluminum alloy was used for optimization. Error data collected from a business jet wing spar assemblies were used in that study. Total cost reduction of approximately 8% was obtained.

Xie and Rais-Rohani [38] developed a probabilistic design optimization method for aircraft structures with reliability, manufacturability and cost constraints. The method was applied to a tapered I-beam wing spar made from Aluminum 2024-T3 with three segments unified using two splices. The spar was under a uniformly distributed load along the length and it was fixed at its root. The results showed a considerable weight reduction.

Visnjic *et al.* [12] firstly investigated the changing effect of structural and geometrical design especially transition fillet between flanges and web, for shear-lag reduction and stiffness, and specific strength improvement of thin-walled composite I-beam wing spars using finite element method. Its web was made of sandwich composite with foam core, its caps and the skins of the web were made of carbon-fiber reinforced composite. The researchers achieved some critical results from their study. Increased web core

thickness has a greater effect on the distribution of the normal stress and the reduction of the shear-lag than fillet size. Extra weight due to the thicker core is not compensated enough by the stress concentration reduction. Greater transition fillet and web core thickness increase the optimum width to thickness ratio of flanges. Shear-lag decreases the strength of the spar more than its stiffness. Using this information, the researchers developed a combined shear-lag and weight optimization methodology to maximize the specific strength and stiffness of composite I-beam spars and under loads used in aerospace engineering.

Fleuret *et al.* [28] designed a wing spar made of carbon-fiber reinforced polymer for an aerobatic aircraft for which low weight is quite significant. As a requirement, the bonds between the composite parts had to transmit high loads them without failure. In that article, the researchers developed a new design for a multi-materials structure with a complex geometry of varying thickness. They used finite element and experimental models for a rectangular beam with the same boundary conditions, fixed from the root under distributed lift load and compared the results. Consequently, wing spar, central spar and central/wing bonding were improved by taking into account the DGAC's requirements (French Authorities for Civil Aviation).

Corrugated webs in I-beam spars have a larger load carrying capacity compared to straight webs. There are two patents on waved-web spars in the literature.

McCarville and Bahr [62] invented a method for forming sine wave web spars made of composite materials. According to that method, the sine wave web spar was formed of web, filler, separator and cap plies. In that invention, the sine wave web spar made of prepreg composite or unidirectional thermoplastic materials could be manufactured with reduced numbers of wrinkles, folds etc. in the individual layers.

Gillespie [63] developed a new design for sine wave web spars which includes a reduction of sine amplitude. The amplitude of corrugation was adjusted for the general stability of the spar and the fasteners. According to the new design, the fasteners on the caps were aligned onto the center line of corrugation. The advantage of this model

was being easier to manufacture than conventional corrugated web spar types, and it still satisfied the structural integrity requirement of the wings.

1.3. Scope of The Thesis

Shear web buckling is one of the most common problems needed to be solved for spars in I-shapes. It occurs due to bending under transverse load. To avoid the shear web buckling various methods are used like adding stiffeners along the beam or designing the web thicker but they cause an increase of mass that is not desired for aircraft. However, webs can also be designed as corrugated to deal with buckling failure.

Corrugated webs have an important advantage compared to flat ones. They are much stronger against shear buckling. In this way, webs do not need any support like stiffener and can be designed much thinner.

The primary goal of this project is to develop a general optimum design methodology for aircraft wing spars with wavy corrugated web for minimum mass irrespective of cost constraint and investigate their mechanical behaviors under aerodynamic load conditions. Because the increasing cost caused by materials or other reasons can easily be compensated by consuming less fuel with a lighter design.

One of the most significant contributions to the literature of this study is that the designed part has a web corrugation changing throughout the length and the redundant mass caused by dense corrugation at the free end is also avoided. The reason for this, the sectional shear force under transversely distributed load changes by decreasing along the beam. Conventional I-beam spars with constantly corrugated web are inefficient due to extra mass caused by redundant corrugation at the free end.

To simplify the problem, merely the spar beam is modeled rather than the entire airplane or wing due to the need for a great amount of time and energy for a very high computational burden. A wing spar is considered as a cantilever beam with a

wavy corrugated web fixed from the root and free from the end under a non-uniformly distributed load.

Firstly, a finite element model for a three-point bending of a beam with a corrugated web is developed to verify the mesh sizes. After obtaining the ideal mesh sizes by considering the analysis time and result accuracy, the main model of the spar is developed. The determined mesh size for the web that is the most critical part in this study is also verified on the spar model reducing by half for the orthotropic materials, too.

Secondly, the load and some dimensions of the spar is defined by using information of Hürkuş Advanced Training Plane that is selected as a model. The whole design is parameterized and the web shape parameters are used to optimize the changing wavy shape of the web throughout the spar.

Lastly, an optimization procedure is applied to the model, and the lightest one is obtained with the buckling failure constraint. It is also examined for the static failure with respect to Tsai-Wu criterion.

2. THEORETICAL BACKGROUND

2.1. I-Beam Wing Spars

Wing spars are the main beam-like parts of aircraft carrying a significant portion of loads due to lift and weight in different flight stages. They can be designed in various shapes with materials for diverse purposes. But the common problem to deal with is withstanding great bending loads occurring on the wings. Bending causes normal and shear stresses on the beams. One of the commonly used beams for dealing with these loads are I-beams since their structure is specially designed for them. Their flanges carry the normal stress and the web carries the shear stress mainly. The stress distributions can be seen in Figure 2.1.

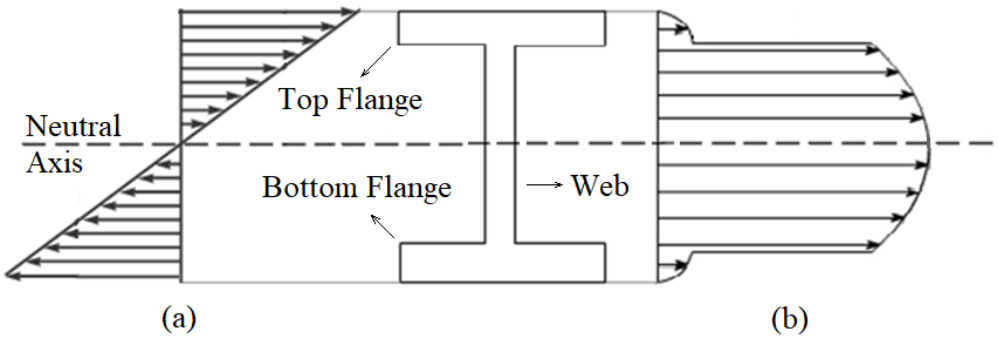

Figure 2.1. Schematic representation of the stress distributions of an I-beam under bending load. (a) Normal and (b) shear stress.

When a load is applied to a beam, also some sectional forces occur on it. The most critical one for this study, shear force is taken into consideration. Sectional shear forces along beams under distributed transverse load change decreasingly. A drawing represents this case for a cantilever beam in Figure 2.2.

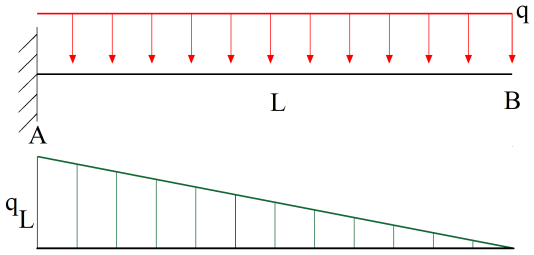

Figure 2.2. Shear force diagram of a beam under uniformly distributed load [64].

2.1.1. Failure Behaviors of I-Beam Wing Spars

There are two main types of failures to be taken into account for wing spar designs, which are the material and structural ones. For the material failure examination, the most critical locations of an I-beam wing spar under bending load as it can be seen in Figure 2.1 are the flanges due to high normal and the web due to high shear stress. Normal stresses are much higher than shear stresses in absolute value exposed to this type of load in general. Hence, flanges are mostly designed thicker than webs. In order to minimize the mass, spars are designed as thin as possible. However, there may occur buckling as a structural instability failure before reaching material failure stress value.

The most common buckling types observed on I-beams subjected to bending are local bucklings because of high compressive stresses on the flanges and high shear stresses on the web and global buckling. They are shown in Figure 2.3.

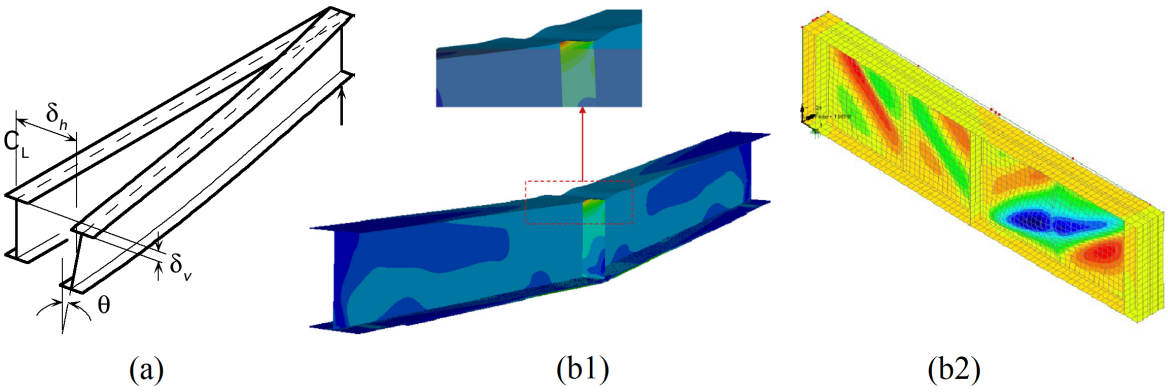

Figure 2.3. Some failure types of I-beams under bending. (a) Global buckling [65], (b1) local compressive flange buckling [66] and (b2) local shear web buckling [67].

Unlike the other applications of I-beams, the local flange buckling and the global buckling cannot happen on wing spars easily since the wing skin and ribs support the spar and prevent these failures. The depiction of a wing can be seen in Figure 2.4. But the shear web buckling due to the high shear stress on I-beams is still a serious problem to be solved. There are some ways to avoid the shear buckling of webs such as the use of stronger materials like steel, thicker web design or use of vertical stiffeners along the beam. However, these solutions also bring another problem, more weight.

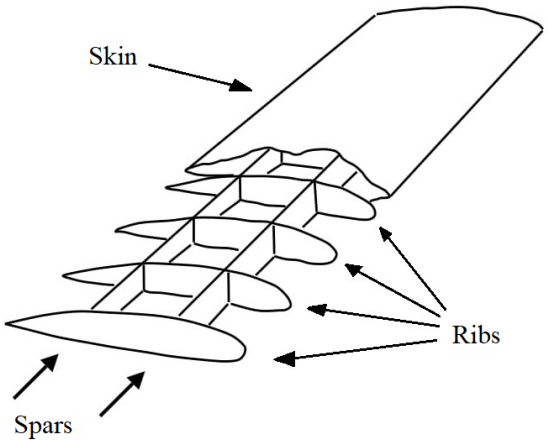

Figure 2.4. Schematic representation of a general wing structure [68].

Weight is a critical issue in aerospace industries. Even a little extra weight can cause a considerable increase in fuel consumption. The weight problem can easily be solved thanks to developing science and technology today. The most efficient way is to use composite materials taking advantage of their high strength with low density. On the other hand, modeling and manufacturing them is very challenging owing to their many constraints. For example, fiber-reinforced polymer I-beams can be produced but cannot be stiffened by vertical supports with ease.

The most effective way of making fiber-reinforced composite I-beams more resistant to shear buckling without any need for stiffener or thicker design is designing with wavy corrugated web [9]. This design also prevents the stress concentration of webs due to sharp edges like the one that trapezoidally shaped corrugated webs have. Furthermore, fiber-reinforced composite materials can also more easily be manufactured

in designs which do not include any sharp one.

2.2. Laminated Composite Materials

Materials are separated into three main types generally as metal, polymer and ceramic. Composite materials are obtained by using more than one material by composing them. There are two main types of composite materials in terms of their structures as sandwich-structured and laminate-structured ones. Laminated composites are used for this study due to their suitability of I-beam-like structures. They are made of more than one ply that have two main phases, the continuous phase (matrix) and the reinforced phase (fibers, particles). A carbon-fiber reinforced polymer material is selected for its high strength with low density.

Plies have multiple mechanical properties and strengths for different material directions. Each ply has more than one elastic modulus, shear modulus, and Poisson's ratio and many strength limits for compression, tension and shear separately. Fiber-reinforced composite materials fail under different types of loads according to their mechanical properties and strengths. Accurate prediction of failures is challenging owing to the structural complexity of fiber-reinforced composites. However, lots of researchers have been studied to failure modes of composite materials for years, and the most general failure types are identified.

2.2.1. Critical Failure Mechanisms of Laminated Composites

There are several critical failure mechanisms for laminated composite materials which can be classified with two main types; the failure of plies and laminates. The most common failure modes of plies usually under tension are fiber rupture, fiber pullout, bridging; under compression is fiber kinking and under any load are fiber-matrix debonding, matrix rupture. The most common failure of laminates under any load is delamination. Their illustrations are presented in Figure 2.5.

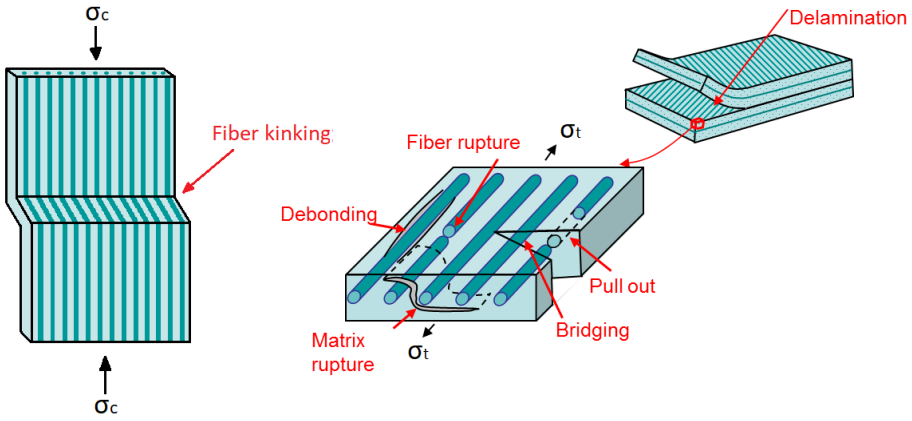

Figure 2.5. Schematic representation of the most common failures of laminated composite materials [69].

To summarize the failure mechanisms, matrix rupture is the most commonly encountered failure type since matrices are usually much weaker than fibers in terms of many properties [70]. Fibers and matrix have quite different mechanical properties that they show dissimilar deformation behaviour under a load. This situation induces debonding of the fiber and matrix. Another common failure is fiber rupture. If the fiber fractures all the structure fails because it is the reinforcement part of the material. Therefore, fiber rupture is one of the most critical failure types even though it is not the furthest encountered one. The last common fiber failure type is fiber kinking. This failure appears under compressive loads. If the fibers are not oriented on the compression axis, there will probably occur a microbuckling and fiber kinking [71]. As a laminate failure, delamination is the separation of plies from interfaces due to the merging of coincidentally formed matrix cracks [72]. Various methods have been developed so far to prevent delamination like 3D weaving.

2.2.2. Failure Criteria of Laminated Composites

The failure load prediction is critical for engineering design because a precise prediction without manufacturing prototypes and performing tests can prevent from a great waste of time and money. Hence, lots of researchers have been developed

some failure prediction methods. However, each method can be insufficient in some problems owing to very high mechanical complexity of composite materials. For this reason, analyses of composite materials are generally carried out with respect to more than one failure criterion to obtain more accurate results.

The most widely used failure criteria are the maximum stress and maximum strain criteria. Each one has five sub-criteria. They define the maximum stress and strain limits for the longitudinal (fiber direction) tension and compression, the transverse tension and compression and the shear conditions. If anyone of them reaches its limit, the material fails [73]. As the first of them, sub-criteria of the maximum stress criterion equations are presented below.

$$\sigma_1 \geq \sigma_{1t} \tag{2.1}$$

$$\sigma_2 \geq \sigma_{2t} \tag{2.2}$$

$$\sigma_1 \leq \sigma_{1c} \tag{2.3}$$

$$\sigma_2 \leq \sigma_{2c} \tag{2.4}$$

$$|\sigma_6| \geq \sigma_6^u \tag{2.5}$$

where σ_1 and σ_2 symbolize the normal stress values respectively in the fiber and transverse directions and σ_6 symbolizes the shear stress value obtained from the orthotropic material analyzed. σ_{1t} is the maximum allowable tensile stress in the fiber and σ_{2t} is the one in the transverse direction. Their signs are positive since the values of tensile stresses are positive, too. Hence, the material is considered failed when σ_1 is equal to or greater than σ_{1t} and/or σ_2 is equal to or greater than σ_{2t} according to Eq. 2.1 and Eq. 2.2. σ_{1c} is the maximum allowable compressive stress in the fiber and σ_{2c} is the one in the transverse direction. Their signs are negative since the values of compressive stresses are negative, too. On account of this, the material is considered failed when σ_1 is equal to or less than σ_{1c} and/or σ_2 is equal to or less than σ_{2c} according to Eq. 2.3 and Eq. 2.4. Lastly, σ_6^u is the ultimate allowable magnitude of the shear stress independent of the direction and the sign of the stress. For that reason, if the absolute value of σ_6 reaches or exceeds the σ_6^u value, the material is considered as failed

according to Eq. 2.5 [74].

Likewise the maximum stress criterion, the maximum strain criterion has also five equations similar to ones expressed above. They are aligned below.

$$\varepsilon_1 \geq \varepsilon_{1t} \tag{2.6}$$

$$\varepsilon_2 \geq \varepsilon_{2t} \tag{2.7}$$

$$\varepsilon_1 \leq \varepsilon_{1c} \tag{2.8}$$

$$\varepsilon_2 \leq \varepsilon_{2c} \tag{2.9}$$

$$|\gamma_6| \geq \gamma_6^u \tag{2.10}$$

where ε_1 and ε_2 symbolize the normal strain values respectively in the fiber and transverse directions and γ_6 symbolizes the shear strain value obtained from the orthotropic material analyzed. ε_{1t} is the maximum allowable tensile strain in the fiber and ε_{2t} is the one in the transverse direction. Their signs are positive since the values of tensile strains are positive, too. Accordingly, the material is considered failed when ε_1 is equal to or greater than ε_{1t} and/or ε_2 is equal to or greater than ε_{2t} according to Eq. 2.6 and Eq. 2.7. ε_{1c} is the maximum allowable compressive strain in the fiber and ε_{2c} is the one in the transverse direction. Their signs are negative since the values of compressive strains are negative, too. Therefore, the material is considered failed when ε_1 is equal to or less than ε_{1c} and/or ε_2 is equal to or less than ε_{2c} according to Eq. 2.8 and Eq. 2.9. Finally, γ_6^u is the ultimate allowable magnitude of shear strain independent of the direction and the sign of the strain. That's why, if the absolute value of γ_6 reaches or exceeds the γ_6^u value, the material is considered as failed according to Eq. 2.10 [74].

The maximum stress and the maximum strain criteria are good enough for failure predictions under uniaxial loads. Nevertheless, they may give different results under multi-axial loading conditions. To solve this problem, some interactive failure criteria have been developed. They use the stress and strain values together for failure examination. Tsai-Wu as one of the mostly used criterion is selected in this study [75]. When the index reaches 1, Tsai-Wu criterion predicts the laminate as failed. The equation of

this criterion for orthotropic materials is given below.

$$\begin{aligned} &F_1\sigma_1 + F_2\sigma_2 + F_3\sigma_3 + F_4\sigma_4 + F_5\sigma_5 + F_6\sigma_6 \\ &+F_{11}\sigma_1^2 + F_{22}\sigma_2^2 + F_{33}\sigma_3^2 + F_{44}\sigma_4^2 + F_{55}\sigma_5^2 + F_{66}\sigma_6^2 \\ &+2F_{12}\sigma_1\sigma_2 + 2F_{13}\sigma_1\sigma_3 + 2F_{23}\sigma_2\sigma_3 \leq 1 \end{aligned} \tag{2.11}$$

If the shear strengths in three planes τ_{12}, τ_{13} and τ_{23} are assumed as they have the same magnitudes on a plane that are with opposite signs, F_1, F_2, F_3, F_{11}, F_{22}, F_{33}, F_{44}, F_{55}, F_{66} coefficients are obtained as follows.

$$F_1 = \frac{1}{\sigma_{1t}} - \frac{1}{\sigma_{1c}} \tag{2.12}$$

$$F_2 = \frac{1}{\sigma_{2t}} - \frac{1}{\sigma_{2c}} \tag{2.13}$$

$$F_3 = \frac{1}{\sigma_{3t}} - \frac{1}{\sigma_{3c}} \tag{2.14}$$

$$F_4 = 0 \tag{2.15}$$

$$F_5 = 0 \tag{2.16}$$

$$F_6 = 0 \tag{2.17}$$

$$F_{11} = \frac{1}{\sigma_{1t}\sigma_{1c}} \tag{2.18}$$

$$F_{22} = \frac{1}{\sigma_{2t}\sigma_{2c}} \tag{2.19}$$

$$F_{33} = \frac{1}{\sigma_{3t}\sigma_{3c}} \tag{2.20}$$

$$F_{44} = \frac{1}{\tau_{23}^2} \tag{2.21}$$

$$F_{55} = \frac{1}{\tau_{31}^2} \tag{2.22}$$

$$F_{66} = \frac{1}{\tau_{12}^2} \tag{2.23}$$

If the strengths in equibiaxial tension are assumed as $\sigma_1 = \sigma_2 = \sigma_{b12}$, $\sigma_1 = \sigma_3 = \sigma_{b13}$ and $\sigma_2 = \sigma_3 = \sigma_{b23}$ then F_{12}, F_{13} and F_{23} can be found as follows.

$$F_{12} = \frac{1}{2\sigma_{b12}^2}[1 - \sigma_{b12}(F_1 + F_2) - \sigma_{b12}^2(F_{11} + F_{22})] \tag{2.24}$$

$$F_{13} = \frac{1}{2\sigma_{b13}^2}[1 - \sigma_{b12}(F_1 + F_3) - \sigma_{b13}^2(F_{11} + F_{33})] \tag{2.25}$$

$$F_{23} = \frac{1}{2\sigma_{b23}^2}[1 - \sigma_{b23}(F_2 + F_3) - \sigma_{b23}^2(F_{22} + F_{33})] \tag{2.26}$$

2.3. Finite Element Method

The finite element method is a solution type of complex problems by separating them into simpler sub-problems. Each one is solved in itself and thus the complete solution is reached. This method has a significant place in various engineering sectors today because of its advantages. It is used for simulating real-world problems in computer systems. In this way, an enormous waste of time and money due to the manufacturing of prototypes and doing experiments on them are avoided. To meet the growing demand for different purposes, various finite element modeling software applications have been developed and are widening their area of use every day.

There are several types of analyses that can be carried out by today's finite element modeling programs. In this study, structural analyses are used. They are mainly separated into two categories as explicit and implicit. Explicit analyses are dynamic and depending on time, and implicit analyses are static. Because the major goal of this project is to model and optimize a wing spar against static loading, static structural analysis is selected. It can be applied linearly or nonlinearly.

In linear analyses, models are handled as deformed in the only elastic region by ignoring all nonlinearities like plasticity. This provides a remarkable time-saving. Nevertheless, most of the real-world problems are not convenient for linear analyses owing to permanent deformations after some critical load levels. An example graph of a stress-strain relation before and after a failure can be seen in Figure 2.6.

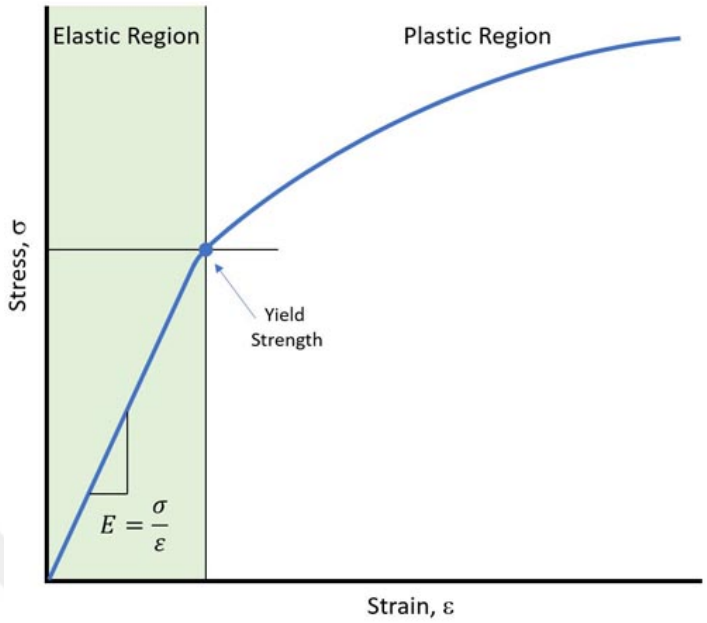

Figure 2.6. A stress-strain graph example with elastic and plastic regions [76].

As seen in the figure above, elastic modulus E is the ratio of the change of stress to the change of strain in the elastic region. Only small, temporary deformations occur there and the graph shows a linear change. However, after large deformations, a failure occurs and the stress-strain ratio begins to change nonlinearly.

Every structure has a maximum load capacity before undergoing failure. It may yield, fracture or buckle under too high loads according to its material and structure properties, and the type of load applied. In this thesis, buckling is handled as a critical stability failure mainly.

In the stability problems, structures show various displacements and reaction forces via changing shape, amount of load and deflection. Unstable systems can be classified into three categories that can be seen in Figure 2.7. λ, u and the points on the curve represent the load, displacement and limit points as locations of the change of the graph direction respectively.

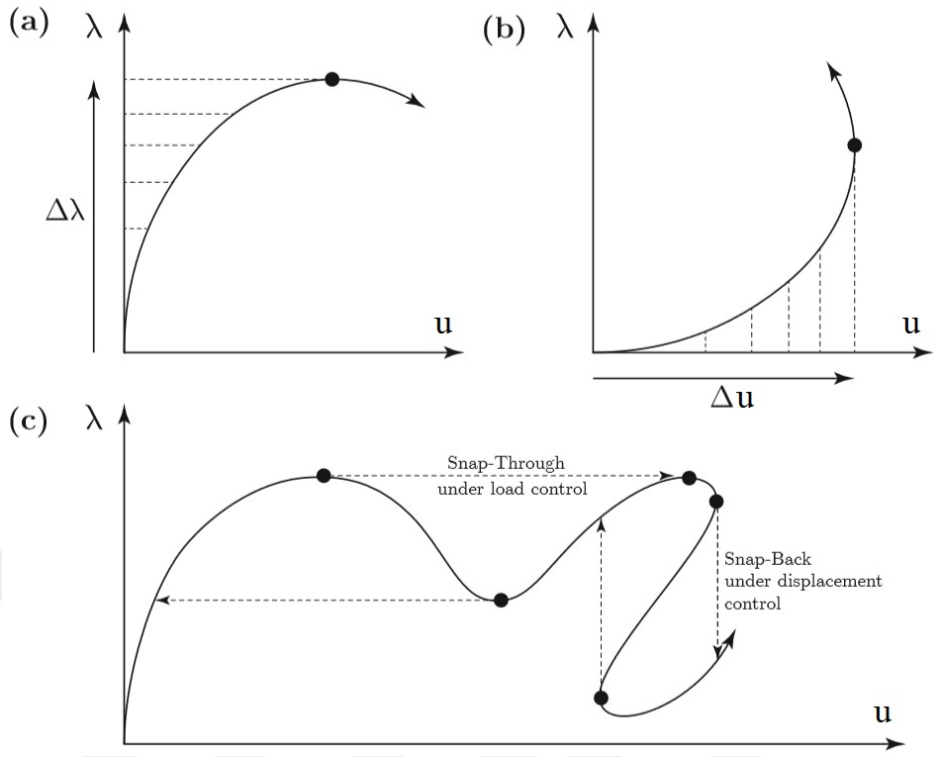

Figure 2.7. Unstable systems under (a) load control (snap-through instability), (b) displacement control (Snap-Back Instability) and (c) both load and displacement control [77].

In the finite element method, if a load higher than the capacity of the structure is applied using nonlinear analysis, the model cannot converge to a solution. Thus, the best way to find the maximum buckling load capacity is to apply gradually increasing loads and terminate the analysis at the point model cannot converge. The program used in this thesis APDL has a very useful method to find the maximum load before the first failure behavior that is called the Arc-Length method.

2.3.1. Arc-Length Method

In the Arc-Length method, the load is divided into small portions and applied by being modified iteratively. The sizes of the load steps are controlled in each iteration using the radius of a created arc. Then the model is solved for both the load and displacement change. A schematic Arc-Length solution is shown in Figure 2.8.

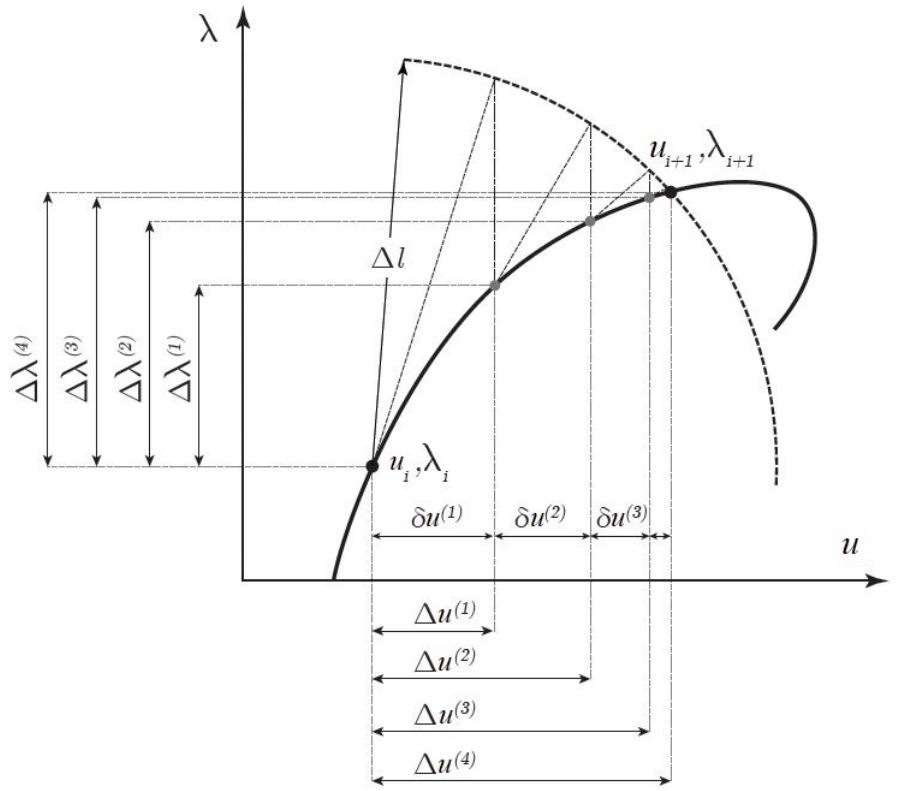

Figure 2.8. A schematic representation of the Arc-Length method iterations. u and Λ represent a normalized displacement and the load increment parameter respectively [77].

This method is used in APDL by defining the maximum and minimum load multipliers for optimum analysis time and result accuracy. Then, an optimization algorithm including the Arc-Length buckling analysis code is developed. The optimization method is discussed in the next section.

2.4. Optimization Methods

Optimization is generally defined as the minimization or maximization of a function that may have one or more linear or exponential parameters. There are various optimization methods today. They can mainly be classified as gradient-based and heuristic methods [78]. An example of gradient-based optimization process is presented in Figure 2.9.

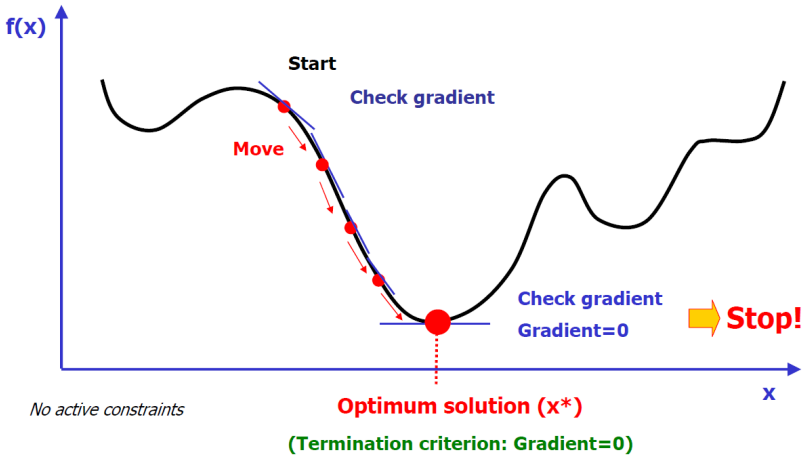

Figure 2.9. A schematic representation of a gradient-based optimization procedure on graph of a function [78].

Gradient-based optimization methods are quick. They prevent a great waste of time and energy consumption. But they find the closest minimum and maximum (extremum) points. This causes missing the global extremum point sometimes and is not a desired situation for most of the engineering problems.

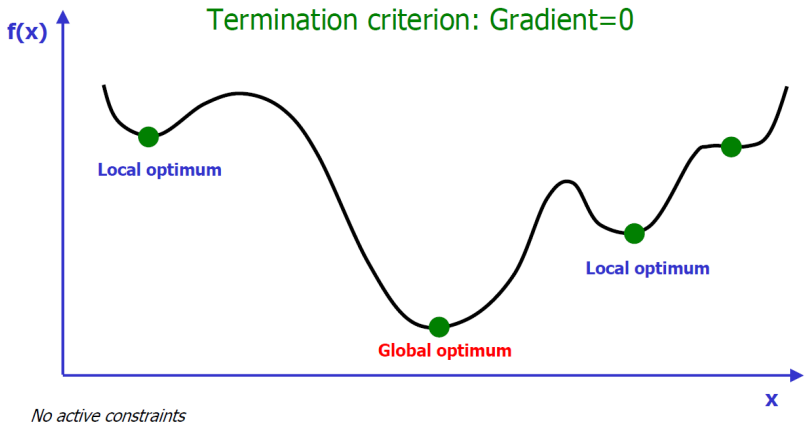

Figure 2.10. An example of a graph of a function with a global and local minimum and maximum points [78].

Heuristic methods have been developed for problems like these. They are very useful for finding the global optimum point without getting stuck in local extremum

points. Therefore, heuristic methods are usually preferred for engineering optimization studies. Three most common heuristic optimization techniques are:

- Genetic algorithms (GA)
- Simulated annealing (SA)
- Tabu search (TS)

2.4.1. Modified Simulated Annealing

A modified simulated annealing optimization algorithm [79] is selected for optimization procedure because of its considerable advantages. The most important ones can be sorted as follows:

- It can solve highly nonlinear models with lots of constraints.
- It can easily be implemented. A mathematical model is not required.
- It generally needs less time owing to reduced computational effort [80, 81]

As can be understood from the name of the algorithm, its way of working is similar to annealing process that uses temperature decrease like a hot metal waiting for cooling. In the optimization procedure, high temperature decreases with improving the design by probabilistically given various values to parameters. The global optimum point is obtained with the minimum temperature reached.

3. DESIGN PARAMETERS OF THE SPAR BEAM

APDL, the programming language used in this study, allows users to design any finite element model parametrically. The geometry is defined by assigning coordinates to key points in optional coordinate systems (Cartesian, cylindrical, spherical and toroidal). After that, lines, areas and volumes are generated for the desired model.

Modeling a wing spar with corrugated web depending on variables is described in this chapter.

3.1. General Wing Spar Design

The primary goal of this project is to develop a design optimization methodology for composite I-beam wing spars with a wavy corrugated web and examine their mechanical behaviors under aerodynamic loads. A baseline spar model is needed to start optimization. For this purpose, Hürkuş Advanced Training Plane is considered to select main dimensions of the spar beam and to determine the loads. Its approximate spar dimensions are given by Turkish Aerospace Industries (TAI) in a presentation [82], and other required properties are obtained from a brochure [83] published by TAI about the aircraft.

In this study, a component level of design is considered. The full model of the airplane or wing and also L-joints between the web and flanges are not modeled and optimized because of huge computational burden. Only the spar bar is considered in isolation of the other parts and the loads transmitted by the other parts are applied to the spar model. The most complex part of the spar is its corrugated web. The caps having straight shape can be designed using conventional methods or its design can be optimized separately. Hence, optimum shape design for general spar dimensions like flange width and thickness are determined by a parametric study and optimization method is developed for the web shape. General spar beam design details are discussed in this section firstly.

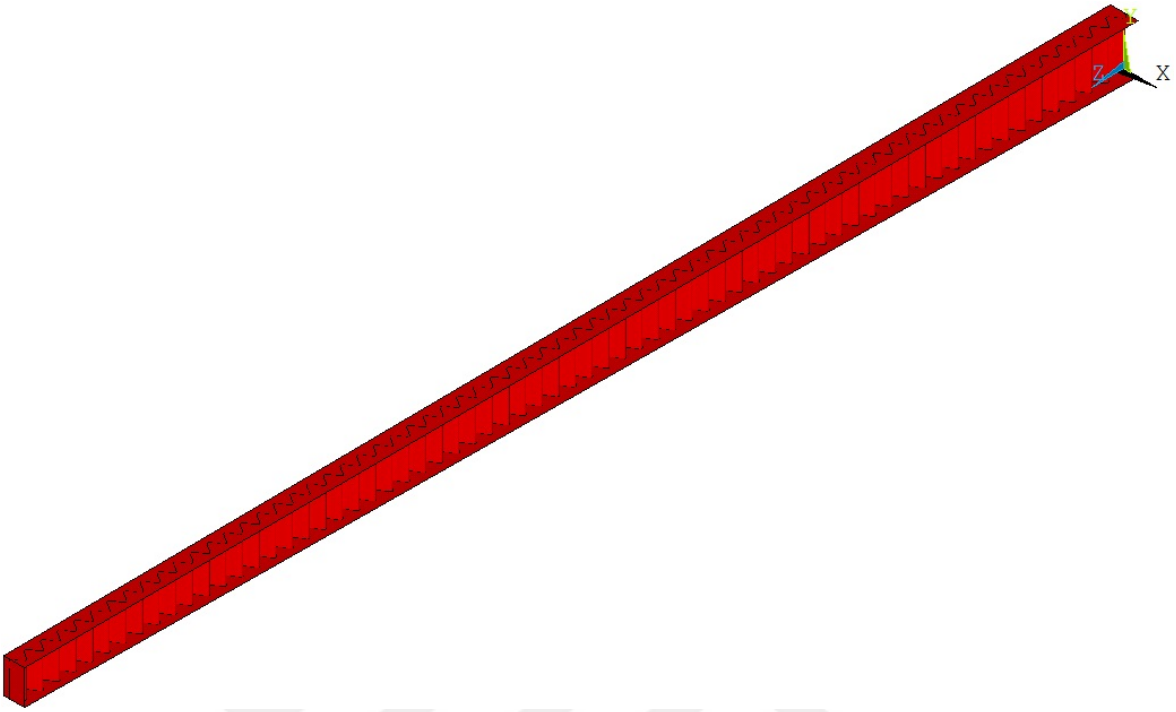

Figure 3.1. Isometric view of a conventional I-beam wing spar with constantly corrugated web.

The spar is considered as a tapered I-beam. Outer dimensions are defined by its length, total height at the root and the end (height of the web and thicknesses of the flanges together), top flange width and bottom flange widths of the fixed root (fuselage side) and the free end (wing tip) separately and bottom height of the free end. They can clearly be seen in Figure 3.2.

The wingspan of Hürkuş Advanced Training Plane is 10.91 meters [83]. There is no detailed information about the entire parts of the plane. That's why the length of each spar by taking into account the width of the fuselage and its connection structures to the wings is considered roughly 4.0 meters (Spar is determined as short as possible to save time in finite element analysis). According to the information provided by TAI, the spar heights for the trainer type aircraft are in the range of 40 mm - 300 mm, widths of I-beam spar flanges should be higher than 70 mm. There is no hard upper limit for the width of flanges but should be less than 200 mm because higher than 200 mm is out of the feasible zone. The dimensions defined within are given in Table 3.1

Shell elements are designed in 2D firstly. Then thicknesses are assigned them. ANSYS gives three offset options for shells thicknesses that can be defined as top, mid or bottom. If top or bottom is chosen for a shell element with a thickness, the whole thickness is generated towards top or bottom. On the other hand, if the mid option is selected, the total thickness is separated into two equal parts and generated towards both sides of the shell. As can be seen in Figure 3.2 shell thickness offsets are defined as top, bottom and mid for the top flange, the bottom flange, and the web respectively.

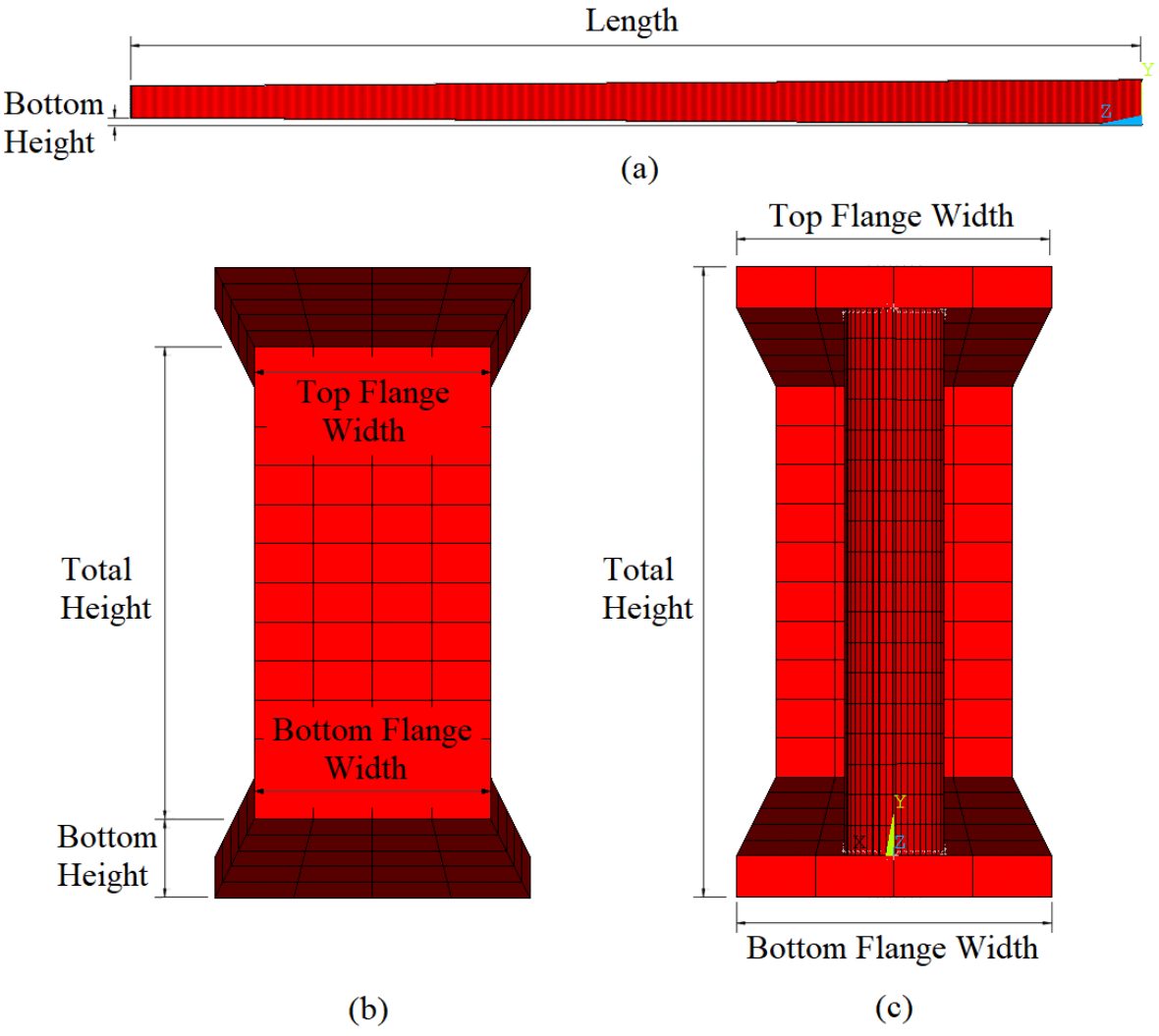

Figure 3.2. Various views of a spar beam. (a) Right view, (b) front view and (c) back view.

Table 3.1. General determined design dimensions.

	Fixed Root [mm]	**Free End [mm]**
Total Height	200	150
Top Flange Width	100	100
Bottom Flange Width	75	75
Bottom Height	-	25

All the dimensions are defined parametrically and can be changed with ease by the developed code.

3.2. Wing Spar Web Design

The corrugated web is considered as a wave with a given wavelength and amplitude and it is defined by a spline curve. There are some works about conventional I-shaped spars with corrugated webs. However, their corrugation wave shape is constant along the beam. An example one can be seen in Figure 3.1. In this study, a methodology is developed to obtain the optimum shape for wing spar beam having a corrugated web with varying wavelength and amplitude throughout the length. For this reason, the shape of the wavy corrugated web is defined with four parameters that are the initial wavelength w_1, wavelength increment rate i, initial amplitude a_i and final amplitude a_f. They are schematically depicted in Figure 3.3.

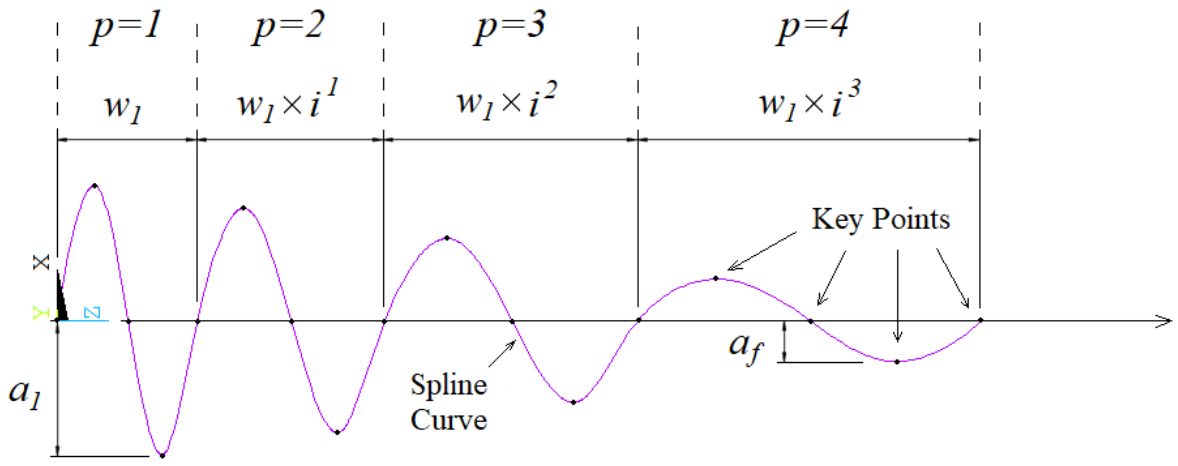

Figure 3.3. Spline curve of the web shape with all parameters.

Parameter p in Figure 3.3 is the period number. As can be seen from the image, waveform of the web is changing depending on the increasing wavelength and decreasing amplitude from the fixed root to free end with the growing number of periods. Since the transverse shear force on cantilevered beams decreases towards the end under distributed loads. The maximum and minimum limits of these parameters given in Table 3.2 selected based on the flange widths.

Table 3.2. Maximum and minimum limits of the web shape parameters.

	Minimum	**Maximum**
Initial Wavelength w_1 **[mm]**	20	100
Wavelength Increment Rate i	1.00	1.05
Initial Amplitude a_1 **[mm]**	0	35
Final Amplitude a_f **[mm]**	0	35

4. FINITE ELEMENT MODELING

In this study, a structural model is created for wing spars using a finite element modeling program, ANSYS. Nonlinear buckling analyses are carried out by a code developed in APDL for parametric design and analysis. After some trial and error process, approximate limits for design are determined. Lastly, a design optimization algorithm that searches the global optimum shape iteratively is integrated to the parametric model for minimization of mass under a given load as stated in the theoretical background chapter.

4.1. Parts of the Spar Model

Spar beam has a high length-thickness ratio. Thus, it is designed as shell to reduce the computational time for analysis. The model has four parts that are the top flange, the bottom flange, the free end cover and the web. Figure 4.1 depicts them separately.

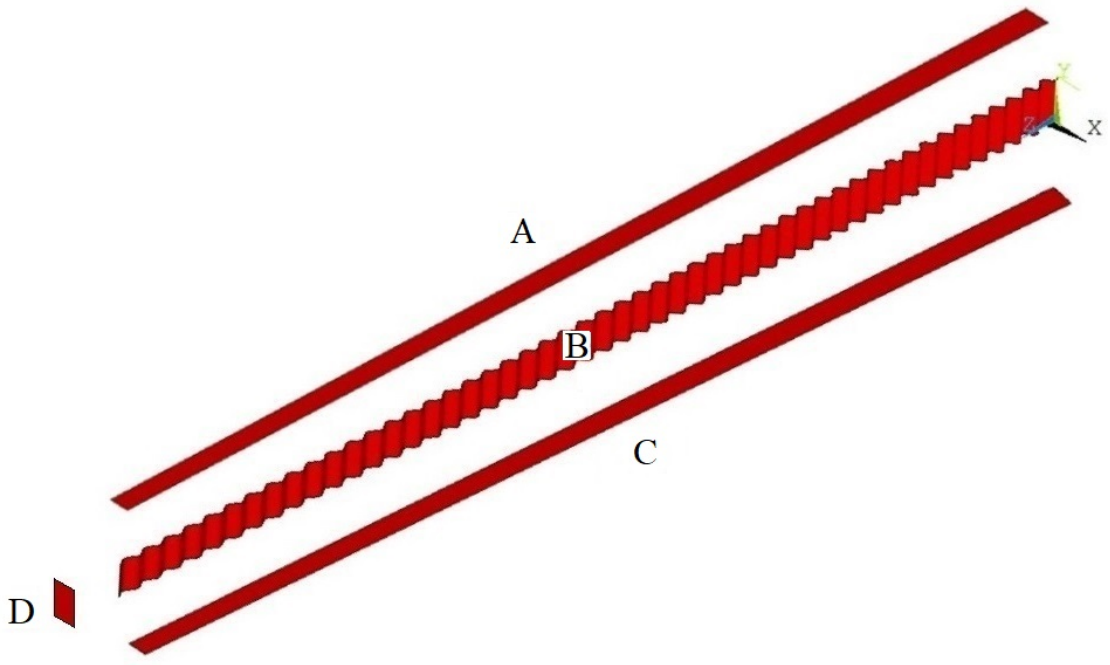

Figure 4.1. Parts of the spar model. (A) Top flange, (B) web, (C) bottom flange and (D) free end cover.

After drawing of the parts, element types are selected, mesh sizes are determined, materials and local coordinate systems (for flanges and web separately), contact and boundary conditions are defined respectively. Finally, optimization procedure is applied using buckling analysis. All steps will be discussed further in the next sections.

4.2. Selection of Element Types

Due to the high length-thickness ratio, the spar is meshed using shell elements. APDL has multiple types of them for various problems, which are classified as axisymmetric-harmonic, explicit thin, general axisymmetric and general structural with 2, 3, 4 and 8 nodes for 2D and 3D spaces.

In this study, structural analysis is carried out for a fiber-reinforced composite material. Hence, SHELL181 and SHELL281 are considered suitable for the model since the elements support orthotropic material properties for structural analyses. The main distinction between them is the number of nodes they have. SHELL181 is a 4-node structural shell element while the other is an 8-node one. SHELL181 is selected for modelling because node number has a critical effect on analysis time in direct proportion. Each analysis requires a considerable amount of time and optimization algorithm needs lots of analyses to find the global optimum design. Besides, 8-node shells are especially useful for highly complex shaped designs but it is unnecessary for a spar beam.

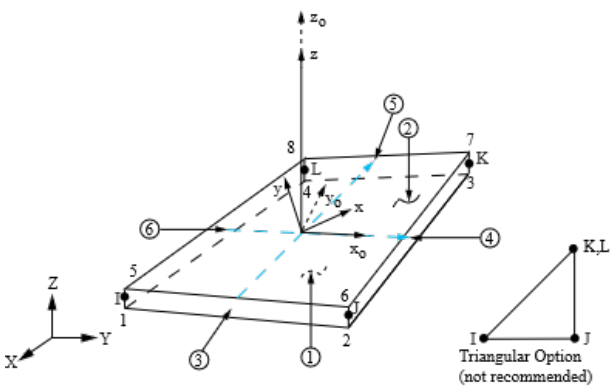

Figure 4.2. Geometry, node locations, and the element coordinate system for SHELL181 [84].

The individual parts are separately meshed, and then bonded contacts are defined between the surfaces of flanges and cover and edges of the web. There are many types of contact and target elements but the contacts created in this model can only be defined as node-to-surface ones as can be seen in Figure 4.3. There is merely one contact-target couple supporting node-to-surface which is CONTA175-TARGE170. Therefore, they are selected for creating the bonded contact.

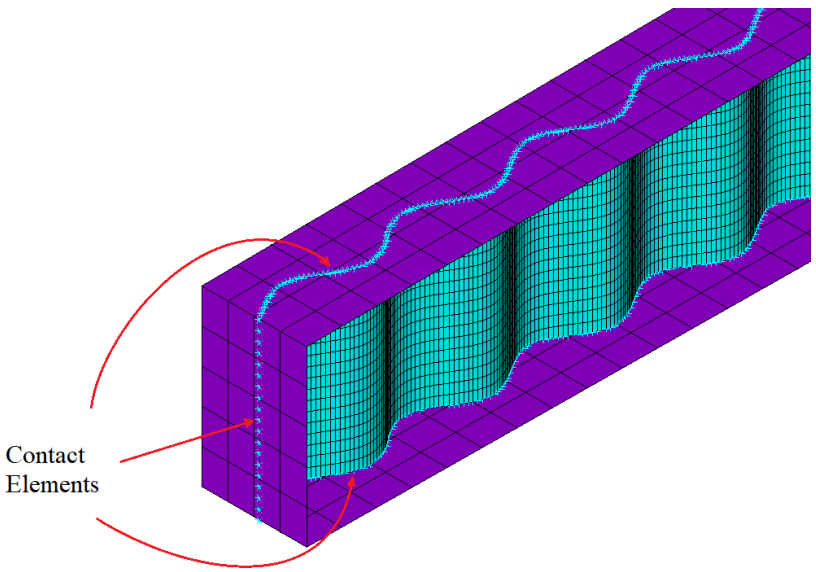

Figure 4.3. Node-to-surface bonded contact elements.

4.3. Model Verification

Meshing is one of the most critical phases of finite element modelings. Types, sizes and shapes of meshes significantly affect the accuracy of results and analysis time. Thus, they should be carefully chosen and implemented to obtain the results accurately in a reasonable time.

In this study, a finite element model with an isotropic material is developed similar to the model used by Kiymaz *et al.* [85] initially. A mathematical model utilized by the researchers is used for checking the accuracy of the results. They modelled various beams made of steel having a yield strength of 235 MPa, elastic modulus 200 GPa and Poisson's ratio 0.3. These I-beams have sinusoidally corrugated web with different

corrugation densities, heights and most of them have holes of various diameters in the webs. Then, the researchers carried out three-point bending analyses to observe the buckling behavior. The results obtained from the analyses were compared with the values calculated using mathematical equations. The method for buckling strength calculation of I-beams with wavy corrugated web is given in Appendix A. The results are also verified by using a technical document [86] having tables of strength values for variously sized beams with a corrugated web.

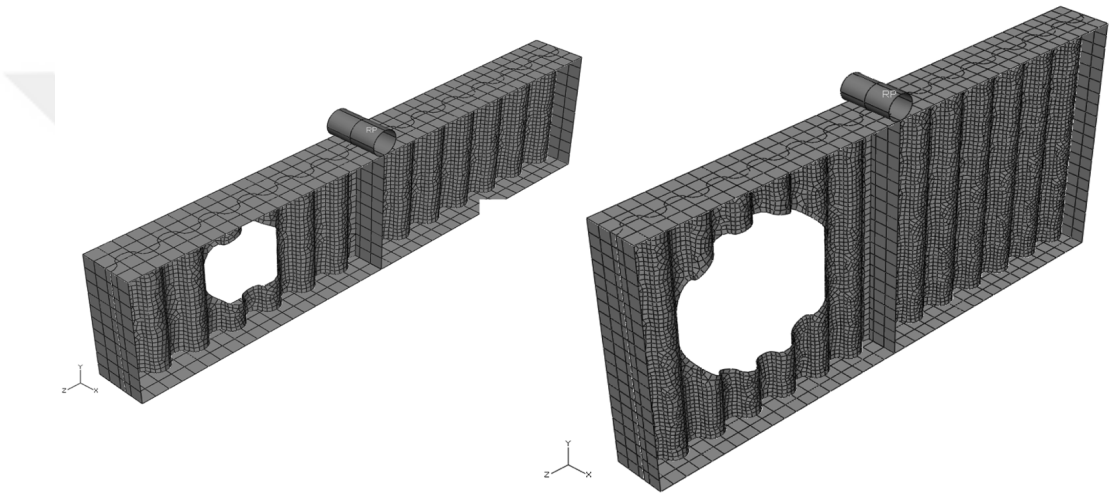

Figure 4.4. Two example of finite element models developed by Kiymaz *et al.* with 0.5 m and 1.0 m heights and web holes [85].

A model without a hole is selected among 15 models for comparison of the results. Then the optimum mesh sizes for maximum accuracy with minimum time are determined by trying various ones. Design features of the selected model are shown in Table 4.1.

Table 4.1. Design features of the model selected for verification.

Web Height [mm]	500
Flange Width [mm]	200
End Cover Plate Width [mm]	200
Central Stiffener Width [mm]	200
Beam Length [m]	2
Web Thickness [mm]	2
Flange Thickness [mm]	12
End Cover Plate Thickness [mm]	12
Central Stiffener Thickness [mm]	20
Wavelength of the Web [mm]	150
Amplitude of the Web [mm]	50

As discussed in the theoretical background chapter, the Arc-Length method is used for buckling analysis. In APDL, that method is activated for load controlled (snap-through instability) nonlinear buckling analysis. This analysis applies the given load to the structure by increasing it beginning from 0 step by step until the model cannot converge to a solution or the load reaches 100% of the given load. The analysis gives a load factor value between 0.0 and 1.0 as the result. The load the structure can carry is found using the following equation.

$$F_c = F_a \times LF \tag{4.1}$$

where F_c and F_a are the load the structure can carry and the one applied to the structure. LF is the load factor.

The Arc-Length method needs selection of values of the maximum and minimum multipliers of the reference arc-length radius. They affect the accuracy of the results and the analysis time. Default maximum and minimum multipliers are 25 and 0.001

[87]. However, this configuration is not efficient in terms of accuracy and time. Hence, several analyses are carried out using different values for the multipliers. Then, the load factors and analysis times are compared.

A model (a sample meshed one is given in Figure 4.5), which is described below this section in detail is selected for the analysis. Initially chosen values for the mesh properties of the model are 50 mm × 50 mm for the flanges, the end cover plates and the stiffener. 2.5 mm is selected for the horizontal dimension and 10 mm for the vertical dimension of the web. For the design configuration given in Table 4.1, the buckling strength is calculated as 135.7 kN with the help of MATLAB, using the mathematical equations given in Appendix A. This is the ultimate sectional shear force the web can carry before buckling. For three-point bending analyses, the load applied to the middle of the beams exactly corresponds to the double of the sectional shear force (for theoretical explanation see Appendix B). Therefore, the maximum allowable load applied to the middle is obtained as 271.4 kN. Therefore, 300 kN is applied and 0.904515 load factor is calculated using Eq. 4.1 as the required one corresponding to 271.4 kN. The obtained values are presented in Table 4.2.

Table 4.2. Buckling analysis results for different ranges of the multiplier for the arc-length radius.

Maximum Multiplier	**Minimum Multiplier**	**Analysis Time [min]**	**Load Factor**
1.0	0.001	44	0.914077
1.0	0.01	27	0.913582
1.0	0.1	19	0.914017
1.0	0.4	14	0.914528
1.0	0.5	17	0.915603
2.0	0.4	16	0.919769
10.0	0.4	21	0.913198

As can be seen in the table, the change in the load factor is little. For this reason, 1.0 and 0.4 are chosen as the maximum and minimum values for the multiplier considering analysis times.

Analysis times are very long since the Arc-Length method uses lots of analyses to find the critical load applying the given load by slowly increasing it. It needs a long time to find the critical level while increasing from 0.0 to roughly 0.9. Because, there will be hundreds of analyses to find an optimum shape. To avoid this problem, 500 kN is applied to the model and corresponding to the load 271.4 kN, 0.542709 is calculated as the critical load factor using Eq. 4.1 for the next analyses.

Square elements are generated in the flanges, the end cover plates, and the central stiffeners; rectangular elements with different vertical and horizontal sizes are generated in the web. The size of the elements in the web in the horizontal direction is smaller than the vertical one, because of the particular corrugation shape, which is straight throughout the height but curved along the beam. There is a critical constraint about the size of square mesh in the flanges such that they should be divided in even numbers through the width. For example, if the flange width is 150 mm, mesh size can be 75 mm to divide it into two or 37.5 mm to divide it into four so that nodes can exist at the middle of the flanges throughout the length. Why it is needed will be discussed in the section of boundary conditions in detail. A sample model meshed according to the aforementioned criteria is shown in Figure 4.5.

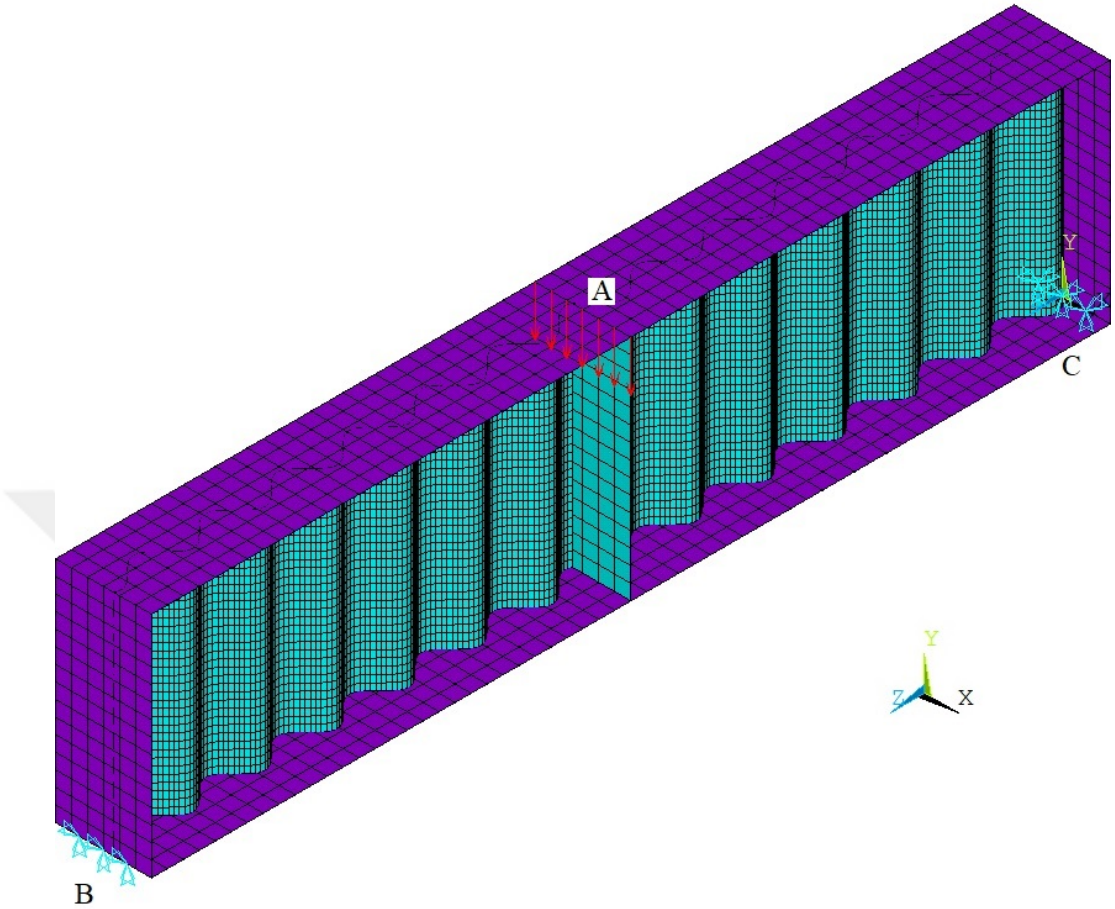

Figure 4.5. A sample meshed model with boundary and loading conditions.

As can be seen in Figure 4.5, for three-point bending analysis the load is applied at A (at the center of the top flange) by distributing it to the nodes equally. Displacement is restricted in x and y-directions in the nodes at B and in all directions at C. In this way, rigid body motion is prevented. A buckled model is presented in Figure 4.6.

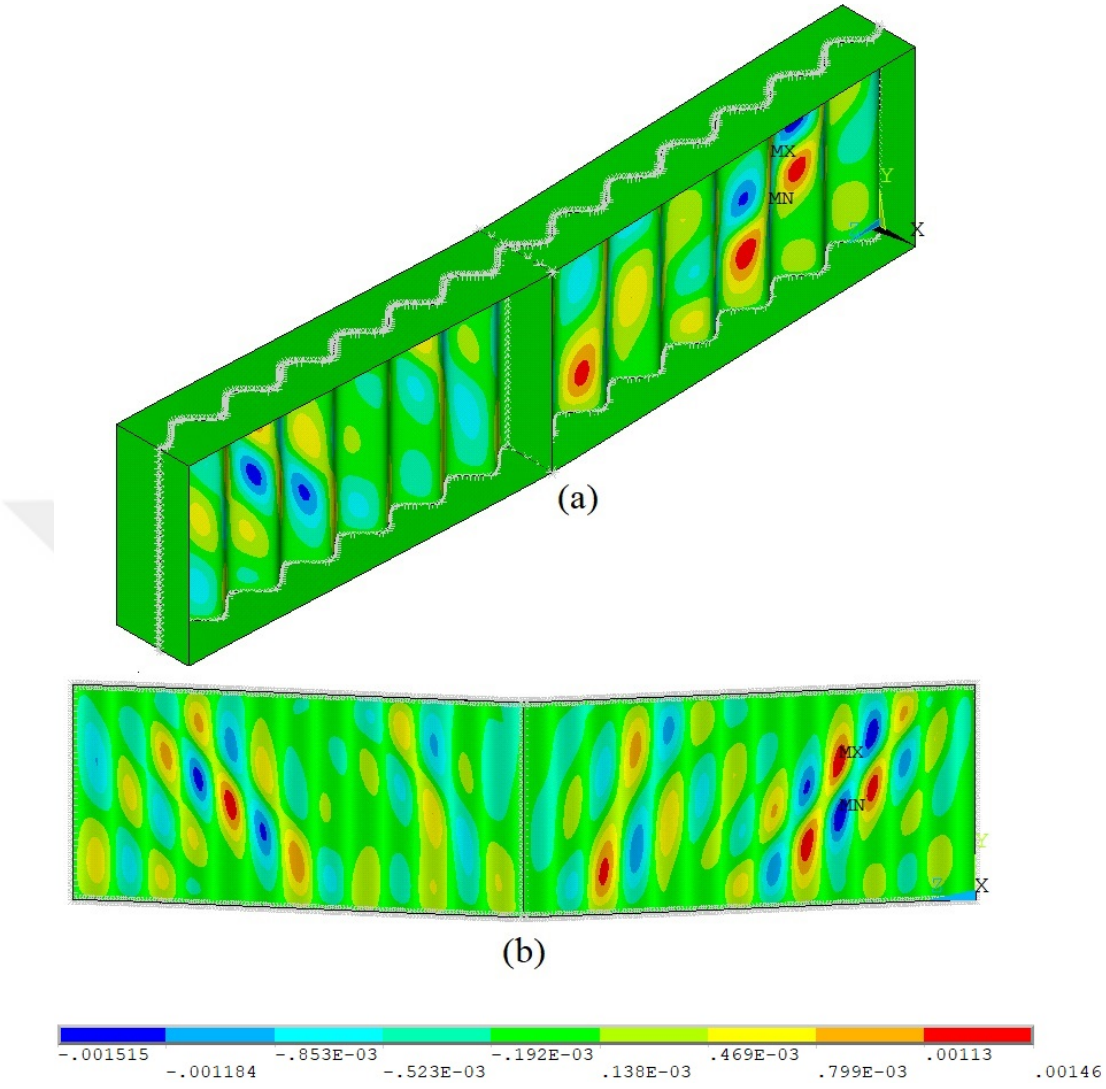

Figure 4.6. A model with the buckled web from (a) isometric and (b) right views with displacement values in meters in the x-direction.

Firstly, the size of the square elements in the caps and the horizontal length of the elements in the web are chosen as 25 mm and 2.5 mm (the mesh with greater than 3 mm horizontal size can not be generated in some densely curved shapes in optimization process) respectively. Then, several analyses for various vertical mesh sizes are carried out to observe the load factors and the analysis times (analysis times may vary depending on the computing power of the computer used). The results for different vertical sizes are given in Table 4.3.

Table 4.3. Buckling analysis results for different vertical mesh sizes of the web.

Vertical Size [mm]	**Analysis Time [min]**	**Load Factor**
8.0	16	0.525775
9.0	10	0.528192
10.0	8	0.552451
11.0	17	0.588721
12.0	18	0.620165
15.0	14	0.710074

As can be seen in Table 4.3, the results change slightly with a quickly increasing analysis time when the vertical mesh size gets smaller than 10 mm. This is because the analysis finds a critical load level causing mini local buckling at the corners between the central stiffener and the flanges. Because there is no stiffener on the spar beam, these results are ignored. 10 mm is selected as the vertical mesh size among the rest of the mesh sizes for low analysis time with an acceptably close load factor to 0.542709 as calculated before. After its selection, new analyses are carried out for various horizontal sizes. Their results are shown in Table 4.4.

Table 4.4. Buckling analysis results for various horizontal mesh sizes of the web.

Horizontal Size [mm]	**Analysis Time [min]**	**Load Factor**
2.0	12	0.526863
2.1	11	0.528783
2.2	13	0.526828
2.3	13	0.551259
2.4	20	0.548747
2.5	8	0.555614
2.6	11	0.568833
2.7	9	0.583603

As seen in Table 4.4 the models horizontal mesh sizes less than 2.3 mm are used in show less load factor values than the required one due to the same problem as mentioned above. For this reason, these values are ignored. From the rest, models with 2.4 mm and 2.5 mm horizontal sizes give the closest load factor values. Nevertheless, the model with 2.5 mm is selected due to its very low analysis time with acceptably close load factor compared to the other model. Then, the results of four analyses for different global mesh sizes are obtained for the determination of ideal global mesh size for flanges. They can be seen in Table 4.5.

Table 4.5. Buckling analysis results for different global mesh sizes of the flanges, end cover plates and central stiffener.

Global Size [mm]	**Analysis Time [min]**	**Load Factor**
20.0	11	0.616193
25.0	8	0.555615
33.3	8	0.528442
50.0	21	0.552578

As seen in Table 4.5, the load factor results for 20.0 mm and 33.3 mm mesh sizes are very different because the program found buckling failure on other parts than the web that do not exist in the spar model. Therefore, these results are ignored, too. The models with 25.0 mm and 50.0 mm mesh sizes give almost the same load factor results but the former one is selected for further analyses due to its much less analysis time when compared to the other one. After determining the mesh size for flanges, new analyses are carried out for the last sensitive mesh size specification. Results obtained from analyses by using slightly changing horizontal mesh sizes of the web is presented in Table 4.6.

Table 4.6. Buckling analysis results for slightly changing horizontal mesh sizes of the web.

Horizontal Size [mm]	**Analysis Time [min]**	**Load Factor**
2.50	8	0.555615
2.51	9	0.554940
2.52	8	0.556371
2.53	10	0.555209
2.54	8	0.556985
2.55	6	0.557058
2.56	11	0.563832
2.57	10	0.563851
2.58	10	0.563837
2.59	11	0.568830
2.60	11	0.568833

All the load factor results given in Table 4.6 are very close to each other and the required one 0.542709. Thus, the model with 2.55 mm horizontal mesh size is selected because of its low analysis time when compared to the other ones. Consequently, the selected mesh configuration and meshed part can be seen in Table 4.7 and Figure 4.7 respectively.

Table 4.7. Determined mesh sizes.

Flange Global Size [mm]	25
End Cover Plate Global Size [mm]	25
Central Stiffener Global Size [mm]	25
Web Vertical Size [mm]	10
Web Horizontal Size [mm]	2.55

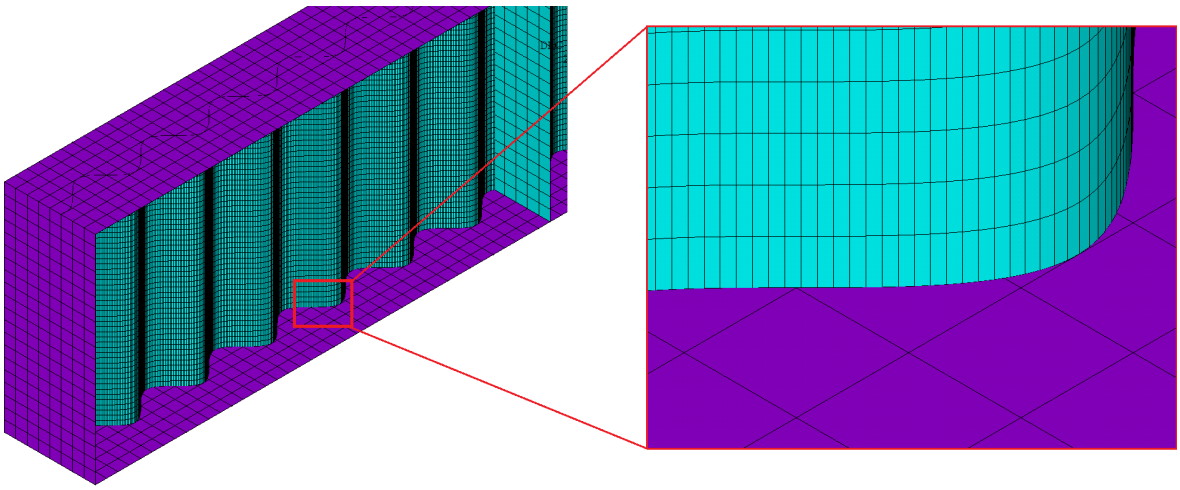

Figure 4.7. The final meshed model with a close view.

These mesh sizes are also examined on the spar beam made of orthotropic material in the next section. The obtained results can be seen in Table 4.12.

4.4. Definition of Materials and Local Coordinate Systems

CFRP's are commonly used in aircraft owing to their high strength-density ratio. IM7 is one of the mostly used carbon-fiber in aerospace applications [88]. Moreover, Kaddour *et al.* [89] gave reliable and detailed information related to IM7 reinforced composite with 8552 matrix. For this reason, IM7/8552 CFRP is used with different stacking sequences for the flanges, the cover and the web. Its material properties are given in Table 4.8

Fibers and plies in reference [89] have 4.5 μm diameter and 0.125 mm thickness respectively. Thus, ply thicknesses are taken as 0.125 mm in this thesis study. The density of the whole material is 1600 kg/m^3.

Table 4.8. Mechanical properties of unidirectional IM7/8552 laminae [89].

Fibre Volume Fraction V_f [%]	60
Longitudinal Modulus E_1 [GPa]	165
Transverse Modulus E_2 [GPa]	9
Through-Thickness Modulus E_3 [GPa]	9
In-Plane Shear Modulus G_{12} [GPa]	5.6
Transverse Shear Modulus G_{13} [GPa]	5.6
Through-Thickness Shear Modulus G_{23} [GPa]	2.8
Major Poisson's Ratio ν_{12}	0.34
Major Transverse Poisson's Ratio ν_{13}	0.34
Through-Thickness Poisson's Ratio ν_{23}	0.5
Longitudinal Tensile Strength σ_{1t} [MPa]	2560
Longitudinal Compressive Strength σ_{1c} [MPa]	1590
Transverse Tensile Strength σ_{2t} [MPa]	73
Transverse Compressive Strength σ_{2c} [MPa]	185
Through-Thickness Tensile Strength σ_{3t} [MPa]	63
Through-Thickness Compressive Strength σ_{3c} [MPa]	185
In-Plane Shear Strength τ_{12} [MPa]	90
Transverse Shear Strength τ_{13} [MPa]	90
Through-Thickness Shear Strength τ_{23} [MPa]	57
Longitudinal Tensile Failure Strain ε_{1t} [%]	1.551
Longitudinal Compressive Failure Strain ε_{1c} [%]	1.1
Transverse Tensile Failure Strain ε_{2t} [%]	0.81
Transverse Compressive Failure Strain ε_{2c} [%]	3.2
Through-Thickness Tensile Failure Strain ε_{3t} [%]	0.7
Through-Thickness Compressive Failure Strain ε_{3c} [%]	3.2
In-Plane Shear Failure Strain γ_{12}^u [%]	5
Transverse Shear Failure Strain γ_{13}^u [%]	5
Through-Thickness Shear Failure Strain γ_{23}^u [%]	2.1

Local coordinate systems are created for each flange and the web for the definition of fiber orientations. Because the free end cover plate is not a critical part, which is just used to prevent flanges from rotating, the local coordinate system is not defined and the bottom flange material properties are used for it.

New coordinate systems are defined such that x-axes are longitudinal along the length while y-axes are transverse and z-axes are through-thickness of material. Because in APDL, fiber orientation system is defined as the rotation angle of fibers from the x-axis (0° start axis) to the y-axis. An illustration about fiber orientation angle is shown in Figure 4.8.

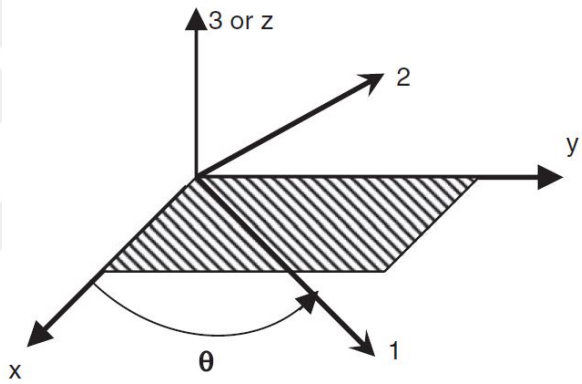

Figure 4.8. Schematic representation of a positive fiber orientation angle (θ) in relation to the reference axes [89].

Local coordinate systems of the top flange, the web and the bottom flange are numbered as 11, 12, and 13 respectively. Each one changes its location and direction with respect to the shape of the general spar and web corrugation. Their locations for a spar can be seen in Figure 4.9.

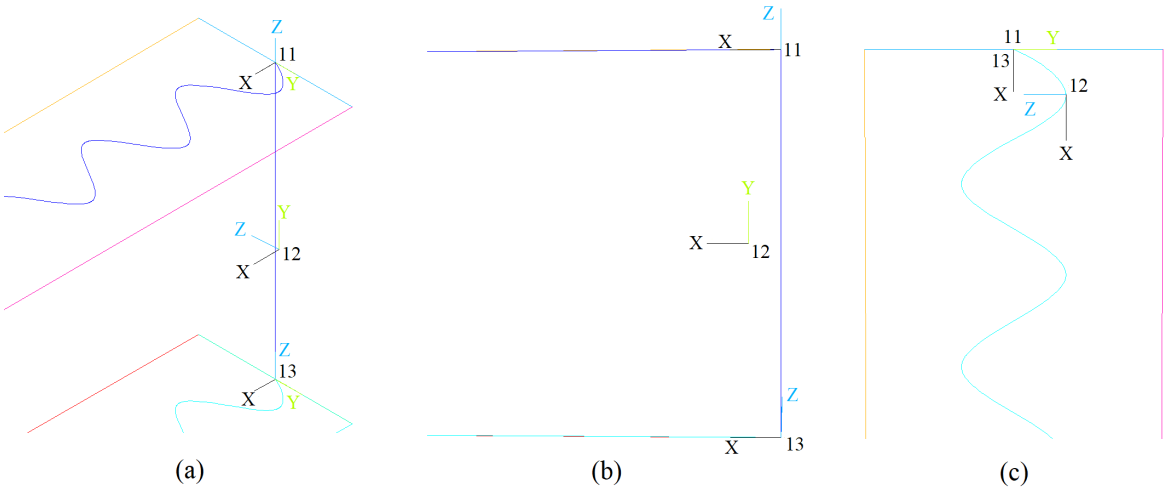

Figure 4.9. Display of the local coordinate systems at the fixed root from (a) isometric, (b) right and (c) top views.

After calculating the required load to be applied as approximately 112 kN, which will be discussed in the load and boundary conditions section in detail, some nonlinear buckling and static pre-analyses are carried out for various configurations using IM7/8552 to determine ply numbers and fiber orientations for each ply.

As mentioned before buckling analyses are carried out using the Arc-Length method. According to failure examination, the load factor has to be greater than 0.6 and the maximum Tsai-Wu index has to be less than 1.0 as discussed in failure criteria of laminated composites section.

Flanges and webs of beams under bending are predominantly exposed to normal and shear stresses respectively. Therefore, laminate lay-ups of the flanges should consist of mainly 0° plies and without 90° fibers. On the other hand, the stacking sequence of the web is defined as ±45° [28].

Critical buckling load is evaluated higher than the required one 112 kN, as 120 kN. Since, after multiple analyses for randomly designed spar beams with isotropic and orthotropic materials, it was found that the structures are able to carry a little

higher loads after the material failure begins until reaching an ultimate load of the buckling behavior. 200 kN is applied to the structure with 0.6 critical load factor to be able to see how much load greater than 120 kN the structure can carry. Firstly, nonlinear buckling analyses are carried out by using 200 kN load with completely 0° and $[+45^\circ/0^\circ/-45^\circ/0^\circ]_S$ flange laminate lay-ups for the different flange and web thicknesses. The results are obtained for the average values of the design limits and are presented in Table 4.9.

Table 4.9. Load factor results of the spar designed with dimensions as average of design limits for various material properties.

Laminate Lay-Up of the Flanges	**Thickness [mm]**		**Load Factor**
	Flange	**Web**	
0°	11	1	0.248212
		1.5	0.546808
		2	1.000000
	12	1	0.248194
		1.5	0.546663
		2	1.000000
	13	1	0.248205
		1.5	0.546776
		2	1.000000
$[+45^\circ/0^\circ/-45^\circ/0^\circ]_S$	11	1	0.248422
		1.5	0.547375
		2	0.948103
	12	1	0.248560
		1.5	0.547440
		2	1.000000
	13	1	0.248600
		1.5	0.547441
		2	0.997290

1.5 mm web thickness seems to be a suitable one when weight and strength are taken into consideration together. Because, the load factors are close enough to the critical value 0.6, so, they can easily be designed stronger than the critical level by optimizing the shape parameters. However, they also need to be examined in the most densely curved shape corresponding to the limit values of the parameters for their reaction to ensure suitability of the chosen value. Initially, buckling analyses under 200 kN are carried out. All load factor values are obtained above the critical level. Then, the actual load to be carried 112 kN is applied to each one and the maximum value of Tsai-Wu index is investigated. All the load factors obtained for 200 kN and Tsai-Wu index values obtained for 112 kN are given in Table 4.10.

Table 4.10. Load factor results of the spar with the most densely curved web for various material properties.

Laminate Lay-Up of the Flanges	**Thickness [mm]**		**Load Factor**	**Maximum Tsai-Wu Index**
	Flange	**Web**		
$0°$	11	1.5	0.646540	0.683673
	12		0.745923	0.668620
	13		0.845250	0.658367
$[+45°/0°/-45°/0°]_S$	11		0.747742	0.858528
	12		0.797547	0.818036
	13		1.000000	0.733000

As seen in Table 4.10, the part having 13 mm-thick flange with stacking sequence $[+45°/0°/-45°/0°]_S$ and 1.5 mm-thick web is the strongest one. It can carry more than 200 kN. Although its maximum Tsai-Wu index is somewhat greater than the part completely made of $0°$ oriented FRP, it can be ignored thanks to very high buckling strength of the other one. Finally decided configuration can be seen in Table 4.11 and schematic representations of lay-ups for each ply group are presented in Figure 4.10.

Table 4.11. Selected material configuration.

	Flanges	**Web**
Lay-Up	$[+45°/0°/-45°/0°]_S$	$[+45°/-45°]_S$
Number of Plies	104	12
Thickness [mm]	13	1.5

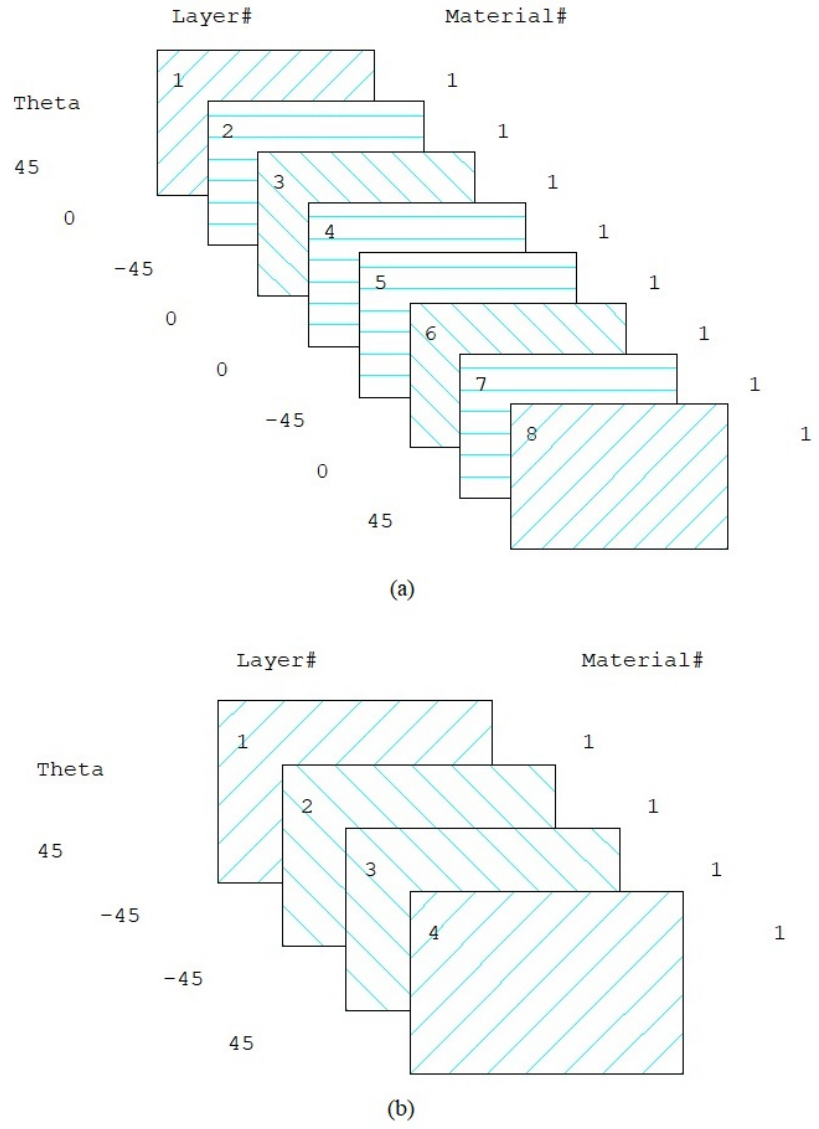

Figure 4.10. Stacking sequences of each ply group of (a) the flanges and (b) the web.

Finally, the determined mesh sizes for the web that is the most critical part in this study are checked again for the defined orthotropic material on the spar model shown in Figure 6.4. Firstly, a buckling analysis is applied for 200 kN. Although, the vertical and the horizontal mesh sizes are reduced by half the buckling result is obtained almost the same. The ultimate load is calculated by multiplying the load factors with 200 kN as roughly 110 kN. A relatively less load 105 kN is applied again the parts with smaller mesh sizes. The resultant maximum Tsai-Wu indexes are also obtained acceptably close compared to analysis times. The results are given in Table 4.12.

Table 4.12. Mesh verification for the spar beam made of orthotropic material.

Mesh Size [mm × mm]	**Analysis Time [min]**	**Load Factor**	**Maximum Tsai-Wu Index**
2.550 × 10.0	5	0.547441	0.817182
2.550 × 5.0	11	0.547622	0.911605
1.275 × 5.0	28	0.547690	0.921445

The maximum and minimum multiplier values and the mesh sizes are determined for the analysis time as short as possible with an acceptably accurate model to examine the developed method on an imaginary design. For an actual spar design much more precise results can be acquired by using lower minimum multiplier values and finer mesh sizes.

4.5. Boundary and Loading Conditions

The boundary and loading conditions are one of the other most critical parts of finite element modeling. They must be selected and applied carefully to simulate the physical conditions as much realistic as possible. The boundary and loading conditions of the wing spar considered in this study are discussed in detail in this section.

4.5.1. Boundary Conditions

As mentioned before, spars are the parts of aircraft wings fixed to the fuselage and free at the other end. They are supported by ribs and wing skin against torsional loads and local buckling failures on flanges. Hence, two boundary conditions are used to simulate the wing spar. The first one is the prevention of displacement and rotation in all directions at the wing root. And the second one is the restriction of movement in the x-direction from the center nodes along the length.

To place the nodes at the center of the flanges, they are meshed by using line division along the length. Flanges are divided into 160 along the length and 4 along the width to obtain 25 mm $\times$ 25 mm element size. These parts are narrowing along the spar, but it has minimal effect on varying mesh size.

The purpose of restraining movement in the transverse direction is to prevent the global buckling failure due to torsional loads explained in failure behaviors of I-beam wing spars section. No torsional load is applied in this study to the model, but the spar can show a global buckling behavior like under torsion load due to very slight unequal mass distribution of the web wave to both sides of the z-axis. The boundary condition is applied to the nodes at the center of the flanges and free end cover. It can clearly be seen in Figure 4.11.

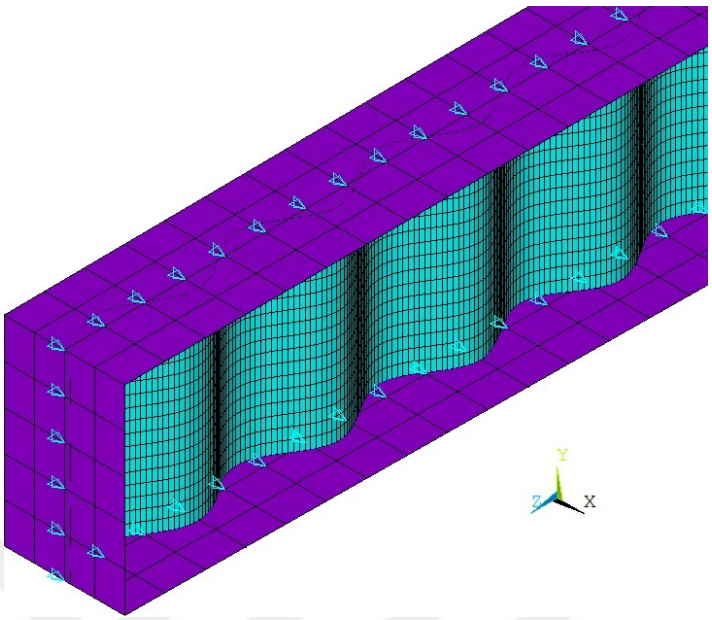

Figure 4.11. Zero displacement boundary condition in the x-direction along the length.

The fixed boundary condition at the root simulates the rigid joint between the wing and fuselage. The fixed root is shown in Figure 4.12.

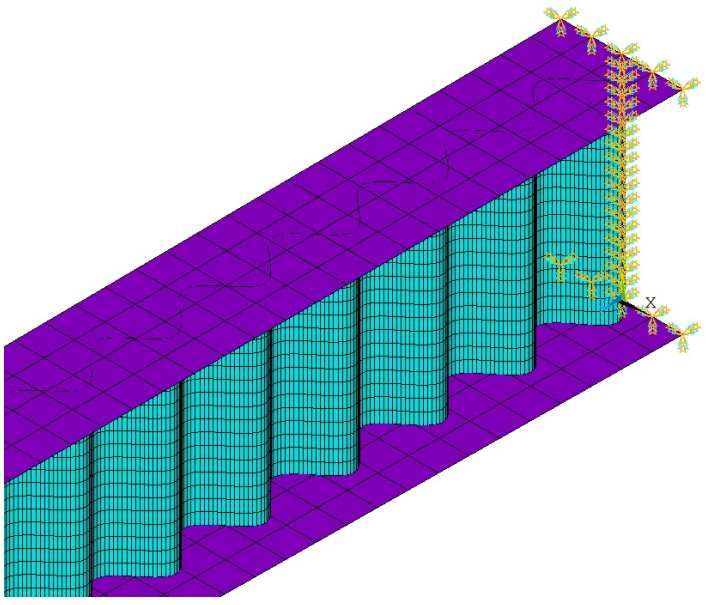

Figure 4.12. Fixed boundary condition in all directions for displacement and rotation at the wing root.

4.5.2. Loading Condition

Spars are the main parts resisting bending particularly due to lift loads in the aeroplane wings as specified in I-beam wing spars section. For this reason, firstly the lift load to be applied is calculated, then the load is distributed using a formulation throughout the spar.

The load is calculated considering Hürkuş Advanced Training Plane as the model. It has no payload on its wings and its engine is attached to the fuselage. Its maximum takeoff weight (MTOW) is 3650 kg, and the positive and negative g limits are +7g/-3.5g [83]. The evaluation process of the applied load based on the information is presented below step by step. Maximum total weight of the aircraft is determined by Eq. 4.2.

$$W_A = MTOW \times g \tag{4.2}$$

The maximum weight of the aircraft is calculated as 37.8 kN. The aircraft are subjected to some critical loads because of g-force effects, especially in sudden maneuvers. Thus, they are designed to be able to carry them. In order to calculate these critical loads, g limits are used. g limits that are positive and negative for different movements are the load factors and they vary from one aircraft to another. They are provided by TAI as mentioned above and the most critical one, +7 is used in this study for optimization. The total critical lift load F_t can be formulated as in Eq. 4.3.

$$F_t = W_A \times g_L \times SF \tag{4.3}$$

where g_L is the g limit and SF is the safety factor, which is used as 1.5 [22]. By using this information, the total load is obtained as 375 kN. In aircraft, approximately 80% of the total lift load is carried by the wings and the rest is carried by the fuselage. Therefore, the lift on a wing is roughly 40% of the total one. This load is carried by several parts of the wing such as the main spar, other smaller spars, ribs or wing skin.

Nevertheless, it is considered that about 75% of it is carried by the main spar [22]. This can simply be formulated as Eq. 4.4.

$$F_s = F_t \times 0.4 \times 0.75 \tag{4.4}$$

As a result, the lift load F_s to be applied to the spar is calculated as 112 kN. This load is distributed along the length considering the spar is subjected to the load directly from wing skin. The distribution is calculated by using a formula given in Eq. 4.5 [12] and applied to the bottom in the upward direction.

$$F(z_i) = \frac{F_0}{L}\sqrt{L^2 - z_i^2} \tag{4.5}$$

where $F(z_i)$ is the varying force depending on the node location, F_0 is the force applied to the first node, L is the spar length and z_i is the changing location in the z-direction of the nodes force applied.

The loads are applied on the nodes at center of the bottom flange. Since the flange bends along the width when loads are applied to all nodes. The applied load distribution can clearly be seen in Figure 4.13. Each force applied on nodes at the center of the bottom flange can also be seen in Figure 4.14.

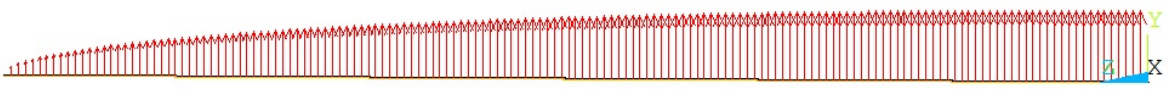

Figure 4.13. The lift load distribution from the right view.

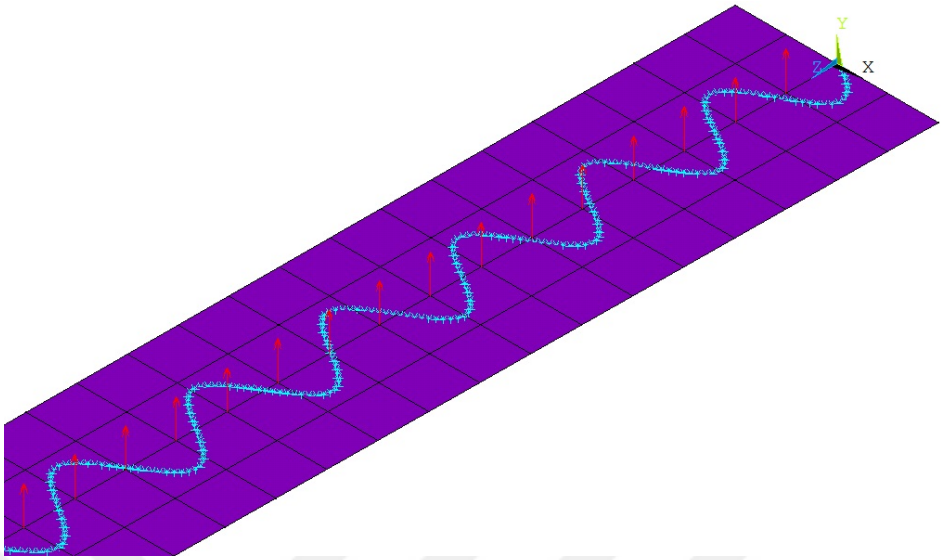

Figure 4.14. The loads applied on nodes at the center of the bottom flange from fixed root side with isotropic view.

A buckled part example under bending is presented in Figure 4.15.

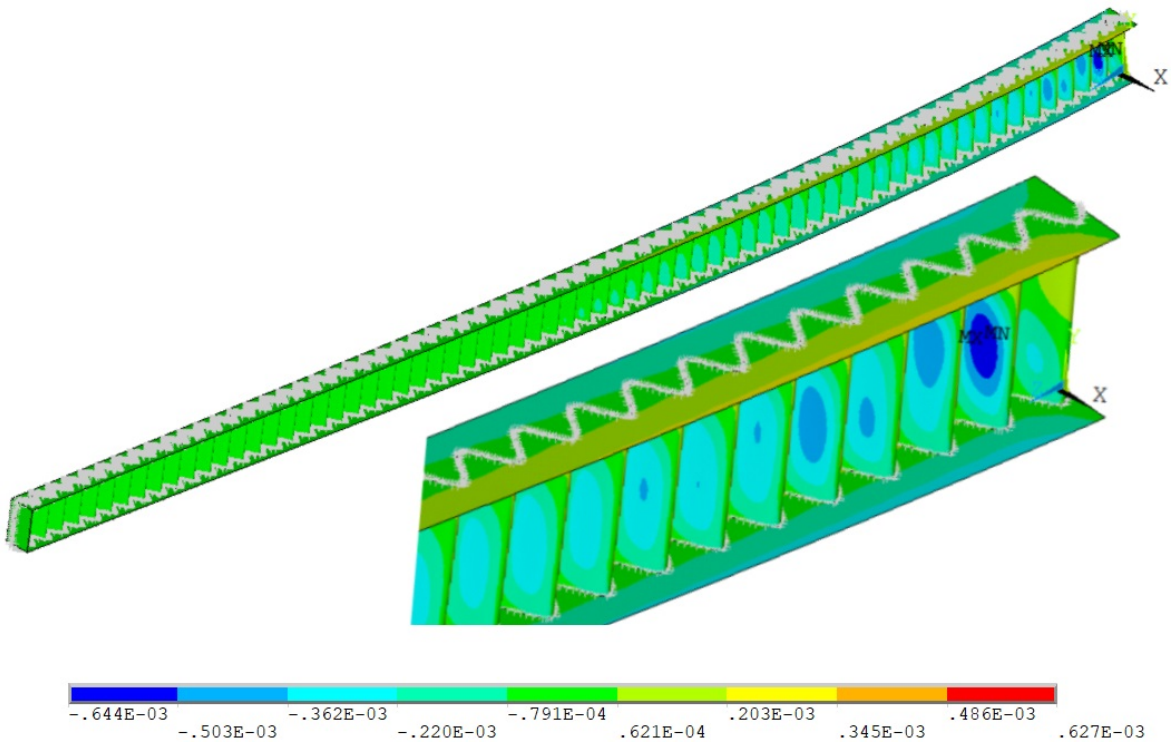

Figure 4.15. An example of a buckled deformed model from isometric view with displacement values in meters in the x-direction.

5. OPTIMIZATION PROCESS

The optimization is carried out for the corrugated web design. The web is defined as a wavy shell area, swept through a straight line between two spline curves on each flange. Design parameters of the web are the initial wavelength w_1, wavelength increment rate i, initial amplitude a_1 and final amplitude a_f. According to defined parameters and general spar dimensions, key points are assigned, and spline curves are generated by passing through these key points. The total number of key points change depending on the initial wavelength and wavelength increment rate. Because they affect the number of wave periods for the unchanging spar length. Lines of a coarse model is shown in Figure 5.1. There can easily be seen how to determine the coordinates of the key points.

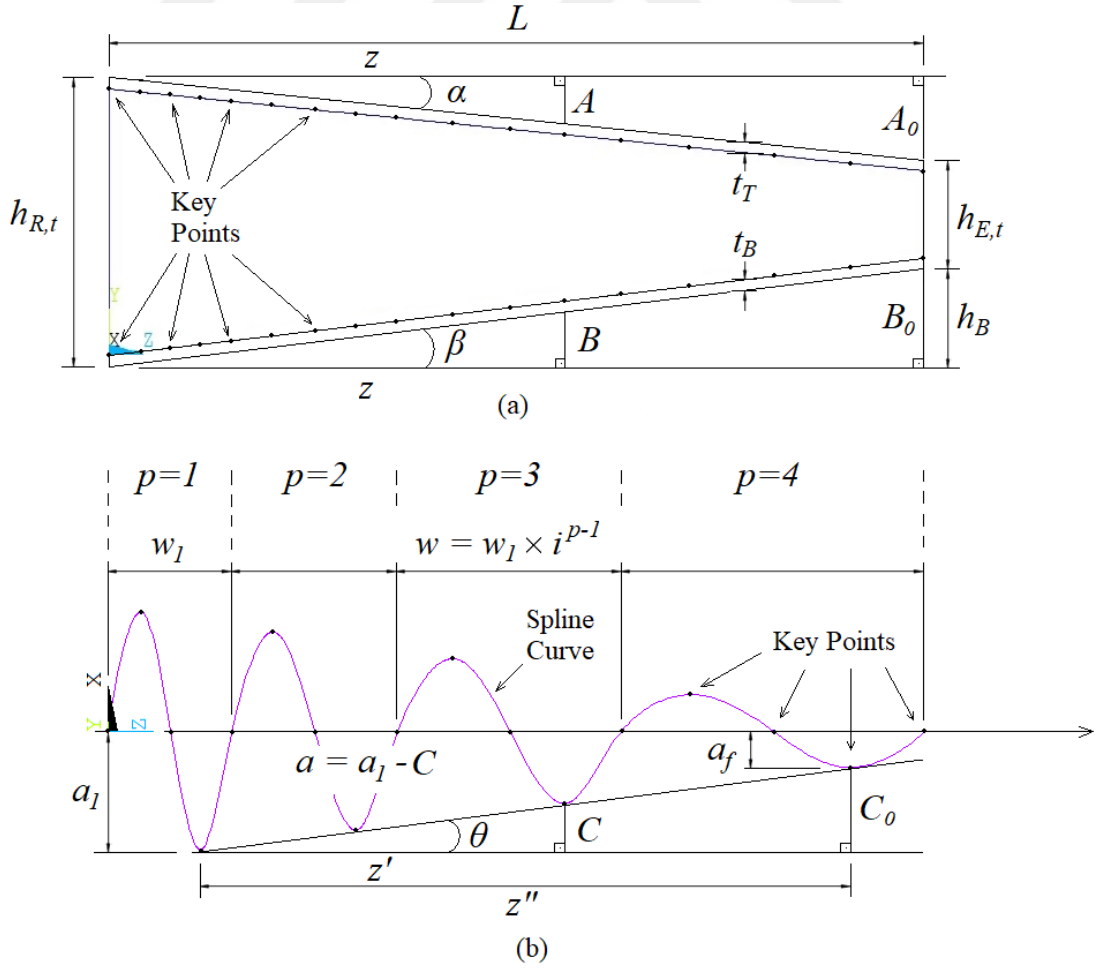

Figure 5.1. Patterns of key points on the spline curve from (a) left and (b) top views.

5.1. Coordinates of the Key Points

Coordinates of the key points presented in Figure 5.1 are depending on several values defined from the beginning according to wing dimensions the spar will be used in. Their y coordinates are changing linearly through the flanges and formulated as the equations below.

$$y_T = h_{R,t} - (t_T + t_B + A) \tag{5.1}$$

$$y_B = B \tag{5.2}$$

where y_T and y_B are y coordinates of the key points on the top and bottom flanges respectively. $h_{R,t}$ is the total height of the fixed root. t_T and t_B are thicknesses of the top and bottom flanges. A and B are the changing distances of the top and bottom flanges respectively from the fixed root in the y-direction. They can easily be found using geometrical similarity rule as follows.

$$A = z \times tan(\alpha) \tag{5.3}$$

$$B = z \times tan(\beta) \tag{5.4}$$

where z parameters are the z coordinates of the key points. α and β are the slope angles of the top and bottom flanges respectively. Tangents are slopes of the flanges. They are calculated by the equations given below.

$$tan(\alpha) = \frac{A_0}{L} \tag{5.5}$$

$$tan(\beta) = \frac{B_0}{L} \tag{5.6}$$

where A_0 and B_0 are perpendicular distances in the y-direction. A_0 is the one between the upper edges of the free end and the fixed root, and B_0 is the height of the free end

in the y-direction. They can simply be found by using Eq. 5.7 and 5.8.

$$A_0 = h_{R,t} - (h_{E,t} + h_B) \tag{5.7}$$

$$B_0 = h_B \tag{5.8}$$

where $h_{E,t}$ is the total height of the free end and h_B is the bottom height of the free end as defined in the general spar design section. The coordinates of the key points in x and z-directions are also needed to be calculated by some mathematical equations. z coordinates of the key points are found by using sizes of wavelengths. Every wave consists of periods. To design the model easily, the wave shape of the web is designed with each period separately. The wavelength of each period is calculated as follows.

$$w_p = w_1 \times i^{p-1} \tag{5.9}$$

where w_1 and i are the initial wavelength and wavelength increment rate as design parameters respectively, and p represents the number of the current period. A key point that has x and z coordinates as zero is assigned at the beginning of the wave to draw the web shape. Then four key points are assigned for each period. The first key point is in the positive x-region for the first amplitude, the second one is on the z-axis at the center of the period, the third one is in the negative x-region for the second amplitude, and the last one is on the z-axis at the end of the period. z coordinates of the key points for each period with two subscripts, the first one means the number of the current period and the second one means the number of the key point in that period, can be calculated as follows respectively. For the initial period, $p = 1$;

$$z_{1,1} = \frac{1}{4} w_1 \tag{5.10}$$

$$z_{1,2} = \frac{1}{2} w_1 \tag{5.11}$$

$$z_{1,3} = \frac{3}{4} w_1 \tag{5.12}$$

$$z_{1,4} = w_1 \tag{5.13}$$

For the other periods, $p > 1$;

$$z_{p,1} = \sum_{k=1}^{p-1} w_k + \frac{1}{4} w_p \tag{5.14}$$

$$z_{p,2} = \sum_{k=1}^{p-1} w_k + \frac{1}{2} w_p \tag{5.15}$$

$$z_{p,3} = \sum_{k=1}^{p-1} w_k + \frac{3}{4} w_p \tag{5.16}$$

$$z_{p,4} = \sum_{k=1}^{p} w_k \tag{5.17}$$

In a period, the second and fourth key points are on the z-axis. Hence, their x coordinates are zero. On the other hand, the first and third key points have opposite sign values with the same magnitudes depending on the amplitude of the current period. x coordinates of each key point can be calculated by using the equations below.

$$x_{p,1} = a_1 - C \tag{5.18}$$

$$x_{p,2} = 0 \tag{5.19}$$

$$x_{p,3} = -x_{p,1} \tag{5.20}$$

$$x_{p,4} = 0 \tag{5.21}$$

where a_1 represents the initial amplitude and C is the decrement of the amplitude. To find the amplitude of each period, C can be calculated by using geometrical similarity as follows.

$$C = z' \times tan(\theta) \tag{5.22}$$

where z' is the perpendicular distance between the third key point of the first period and the one of the current period in the z-direction. The tangent of the theta angle is the slope of an imaginary straight line passing through the key points of the amplitudes

as shown in Figure 5.1. They are found by the formula given below.

$$tan(\theta) = \frac{C_0}{z''} \tag{5.23}$$

$$z' = z_{p,3} - z_{1,3} \tag{5.24}$$

where C_0 and z'' are the perpendicular distances between the third key points of the initial and the final periods in x and z-directions respectively. They can be calculated by using the following equations.

$$C_0 = a_1 - a_f \tag{5.25}$$

$$z'' = z_{f,3} - z_{1,3} \tag{5.26}$$

where the subscript f is the number of the final period. After definition of all the equations for parametric design, the optimization is applied to the model.

5.2. Optimization Algorithm

To find an optimum design, a modified simulated annealing algorithm is selected as discussed in the theoretical background chapter. This algorithm uses sets of configurations by changing the values of parameters randomly and carries out analyses. New values of the parameters are calculated by using the equations given below.

$$w_1' = w_1 + S_{w1} \tag{5.27}$$

$$i' = i + S_i \tag{5.28}$$

$$a_1' = a_1 + S_{a1} \tag{5.29}$$

$$a_f' = a_f + S_{af} \tag{5.30}$$

where S values are the change amounts of the parameters that are determined randomly with some constraints. Firstly, the value of each parameter has to be in its maximum and minimum limits as a general one. In addition to that, there are two critical

constraints as given below.

$$a_1 < \frac{w_1}{3.5} \tag{5.31}$$

$$a_f \leq a_1 \tag{5.32}$$

The constraint given in Eq. 5.31 is critical because some denser corrugations cannot be meshed by APDL. Moreover, it may cause problems in the manufacturing process of the spar with highly dense corrugation. The one given in Eq. 5.32 is also significant because the corrugation density has to decrease towards to free end due to the decreasing sectional shear force. Thus, the final amplitude always has to be equal to or less than the initial amplitude. Within these constraints, all the S values are calculated by the following equations.

$$S_{w1} = s_{w1} \times r \tag{5.33}$$

$$S_i = s_i \times r \tag{5.34}$$

$$S_{a1} = s_{a1} \times r \tag{5.35}$$

$$S_{af} = s_{af} \times r \tag{5.36}$$

where r values are the randomly chosen numbers between -1.0 and 1.0 and s values are the step sizes. A certain amount of step size for each parameter is determined initially and reduced during the optimization. Firstly, they are determined as sufficiently large as possible to examine all the search domain in an ideal time. Initial values are defined depending on the search domain as follows.

$$s_{w1,ini} = \frac{w_{1,max} - w_{1,min}}{4} \tag{5.37}$$

$$s_{i,ini} = \frac{i_{max} - i_{min}}{4} \tag{5.38}$$

$$s_{a1,ini} = \frac{a_{1,max} - a_{1,min}}{4} \tag{5.39}$$

$$s_{af,ini} = \frac{a_{f,max} - a_{f,min}}{4} \tag{5.40}$$

where the maximum and minimum values are presented in the parametric design chapter for each parameter. The step sizes become rather small towards the end of the optimization to find the optimum point more accurately. Step sizes are reduced by the algorithm when the total number of improvements is less than 4% of the total trials in a Markov chain as follows.

$$s'_{w1} = s_{w1} \times c_r \tag{5.41}$$

$$s'_i = s_i \times c_r \tag{5.42}$$

$$s'_{a1} = s_{a1} \times c_r \tag{5.43}$$

$$s'_{af} = s_{af} \times c_r \tag{5.44}$$

where c_r is the reduction coefficient. It is defined as 0.95 but can be selected closer to 1.0 for more accurate results. However, optimization time directly depends on it. If it is much closer to 1.0, the time will be much longer.

After the formulation of parameters and their change, firstly the number of configurations for each set is determined as follows.

$$N = 9n \tag{5.45}$$

where n is the total number of variables. These sets of configurations are updated in every iteration. After the generation of new configurations, objective function values are calculated for each one by using the equation given below.

$$f_{obj} = \begin{cases} m & , LF \geq 0.6 \\ m + P \times (0.6 - LF) & , LF < 0.6 \end{cases} \tag{5.46}$$

where m is the mass, P is the penalty value and LF is the load factor. P is determined as 5 considering the mass of the web. The value of the objective function f_{obj} is checked

for its acceptability as follows.

$$A_{obj} = \begin{cases} 1 & , f_{obj} \leq f_{wst} \\ exp(\frac{f_{wst} - f_{obj}}{T_k}) & , f_{obj} > f_{wst} \end{cases} \tag{5.47}$$

where f_{wst} is the objective function value of a randomly chosen configuration among the worst ones. A new configuration is accepted when it has an objective function value lower than f_{wst}. If not, the acceptance of the configuration is determined depending on A_{obj} and a randomly created number R between 0.0 and 1.0. If A_{obj} is equal to or greater than R the configuration is accepted. When a new configuration is accepted, it is replaced with a randomly chosen worst one. The current configurations are ordered again and all the objective function values are updated with each iteration.

T_k is a checking temperature parameter of the possibility of acceptance. It has the maximum value T_0 that is determined 10^5 before the optimization, at the beginning and decreases during the optimization procedure. In this way, a worse configuration has a higher chance to be accepted while the optimization is in its initial phases. Using higher beginning temperatures provides a possibility to search the whole domain in more detail. Created set configurations at a given temperature is called Markov chain. The value of temperature decreases at the end of each Markov chain. The temperature reduction can be calculated as follows.

$$T_{k+1} = t_{k+1} \times T_k \tag{5.48}$$

where T values are the temperatures, t is the reduction factor. The subscripts show the number of Markov chains. The temperature must decrease with an ideal speed. If it decreases too quickly, the algorithm may miss the global optimum point and be stuck in a local optimum configuration. On the other hand, if it decreases too slowly, the algorithm will need enormous time and energy. Therefore, an ideal one should be selected.

The temperature reduction parameter t takes a value between t_{max} and t_{min} according to the equations given below.

$$t_{k+1} = \begin{cases} t_{max} & , R_{A,k} < R_{s,k} \\ t_{min} & , R_{A,k} \geq R_{s,k} \end{cases} \tag{5.49}$$

where t_{max} and t_{min} are the maximum and minimum reduction factors and defined as 0.9999 and 0.9 respectively. R_A and R_s are ratios calculated using some data in the kth Markov chain as follows.

$$R_{A,k} = \frac{C_{A,k}}{C_{N,k}} \tag{5.50}$$

$$R_{s,k} = \frac{s_{w1,k}}{s_{w1,ini}} + 0.01 \tag{5.51}$$

where C_A and C_N are the numbers of accepted and newly tried configurations in the kth Markov chain respectively. s_{w1} and $s_{w1,ini}$ are the step sizes and they are found by using Eq. 5.37 and 5.41. Temperature does not reduce only when two values, the minimum and current length of Markov chains, $L_{M,min}$ and L_M are equal to each other. They are calculated using the equations below.

$$L_{M,min} = 4n \tag{5.52}$$

$$L_{M,k} = NINT\left[L_{M,min}\left(1 + 2 \times \frac{s_{w1,k}}{s_{w1,ini}}\right)\right] \tag{5.53}$$

where $NINT$ is an APDL command that is used to obtain the nearest integer of the value in the paranthesis.

The SA algorithm used in this study has a different replacement procedure than a conventional one. Initially, N number of configurations that are created before the optimization process are ordered with respect to their cost values (Cost values are the classified ones of objective functions as best, worse, worstbest and worst.). Then, a number of worst configurations are selected from the set of configurations. This number

is simply calculated as follows.

$$N_{wst} = n + 1 \tag{5.54}$$

A randomly selected configuration is replaced among N_{wst} number of worst ones when a randomly created configuration is accepted. So, N_{wst} number of worst configurations become new candidates to be replaced rather than one worst configuration. Iterations continue till all the stopping criteria are satisfied. Two of them are determined as follows.

$$f_{wst} - f_{best} < \delta_1 \tag{5.55}$$

$$T_k < \delta_2 \tag{5.56}$$

where δ_1 and δ_2 are defined as 10^{-4} and 10^{-3}. Their values can be changed and adapted for another model to be optimized.

The flowchart of the optimization procedure can be seen in Appendix C.

6. RESULTS AND DISCUSSION

Spar beam is the main part carrying a considerable amount of the total lift load. The lift load causes bending on it. Due to the bending, a considerable amount of normal stresses on the flanges and shear stress on the web occur as shown schematically in Figure 2.1. To prevent the web from shear buckling, it can be designed thicker or can be supported by vertical stiffeners along the length. But these designs add more weight to the structure. The best way to prevent the shear failure with less weight is to design the web as corrugated due to much higher stability than the flat one and use carbon-fiber reinforced composite as material owing to its high strength to density ratio. The material properties are discussed in Section 4.4 in detail.

The lift load is calculated for the main spar approximately using a training airplane as model. It is directly applied to the spar as a non-uniformly distributed transverse load. Then the boundary conditions are applied and the optimization procedure is carried out. The most complex part of the beam, wavy corrugated web is optimized for minimum mass by defining the web wave depending on four parameters as initial wavelength w_1, wavelength increment rate i, initial amplitude a_1 and final amplitude a_f. More detailed information about the optimization procedure can be obtained from the optimization process chapter.

In this chapter, the displacement and Tsai-Wu results obtained from the spar beams with flat web and the optimally designed ones with the corrugated web are presented. These results are discussed and some solution methods to the possible problems are proposed.

6.1. Spar with Flat Web

At first, the load is applied to spars with the flat web to find the required flat web thickness. A spar with 4.0 mm-thick web carried the total load at the limit. It is shown in Figure 6.1

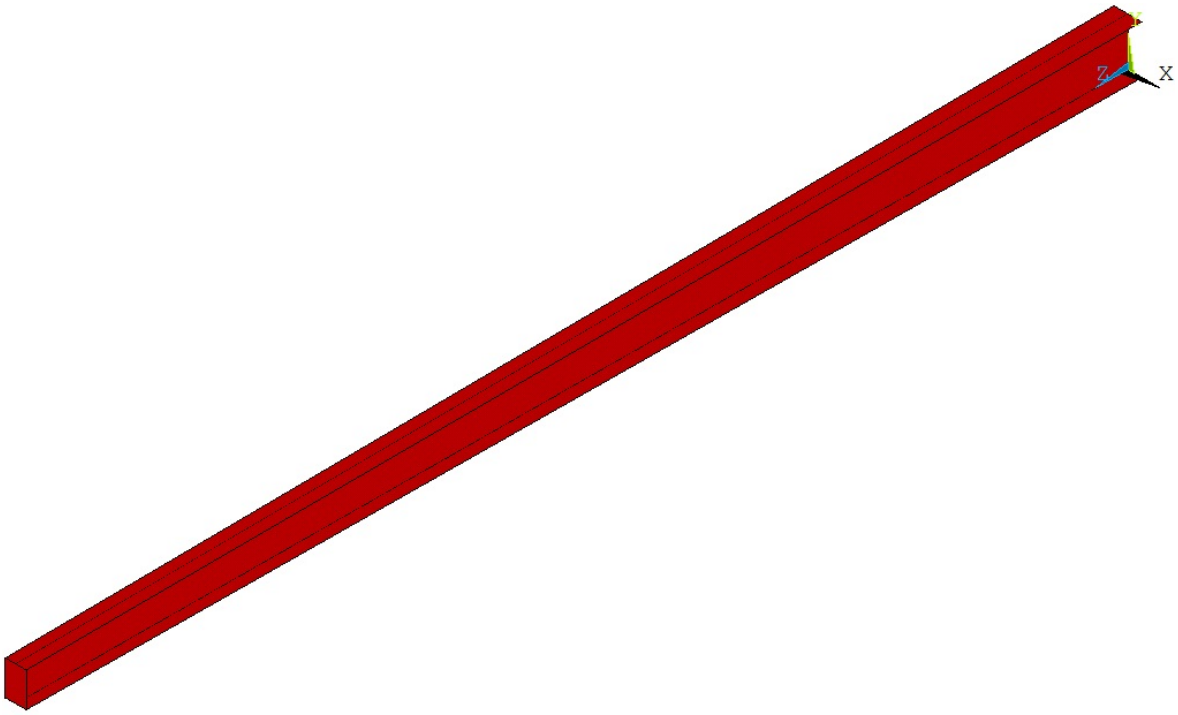

Figure 6.1. The spar with flat web.

Its displacement and Tsai-Wu results with buckled shape are presented in Figure 6.2 and 6.3 respectively.

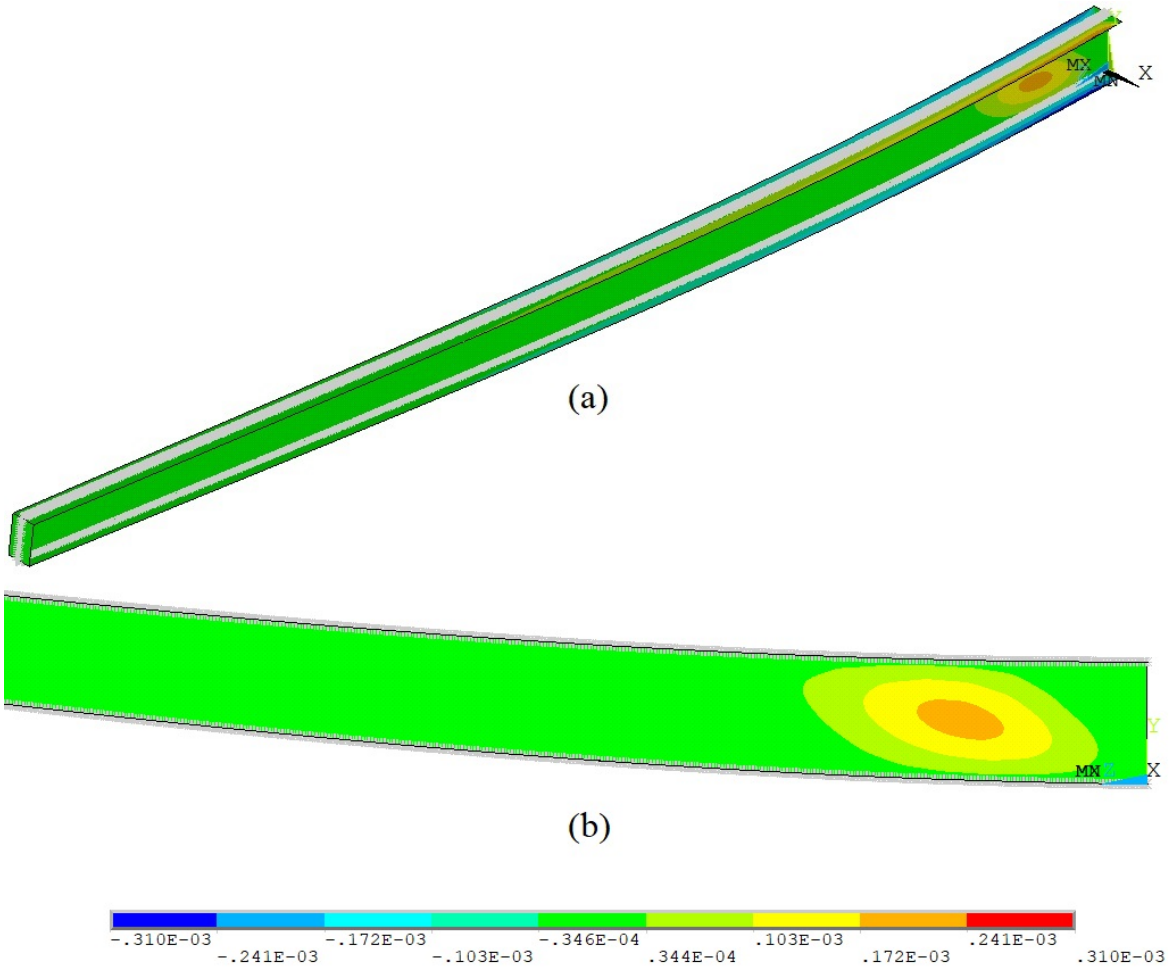

Figure 6.2. The distribution of the displacement in meters in the x-direction of the buckled spar with 4 mm-thick web from (a) isometric and (b) right views.

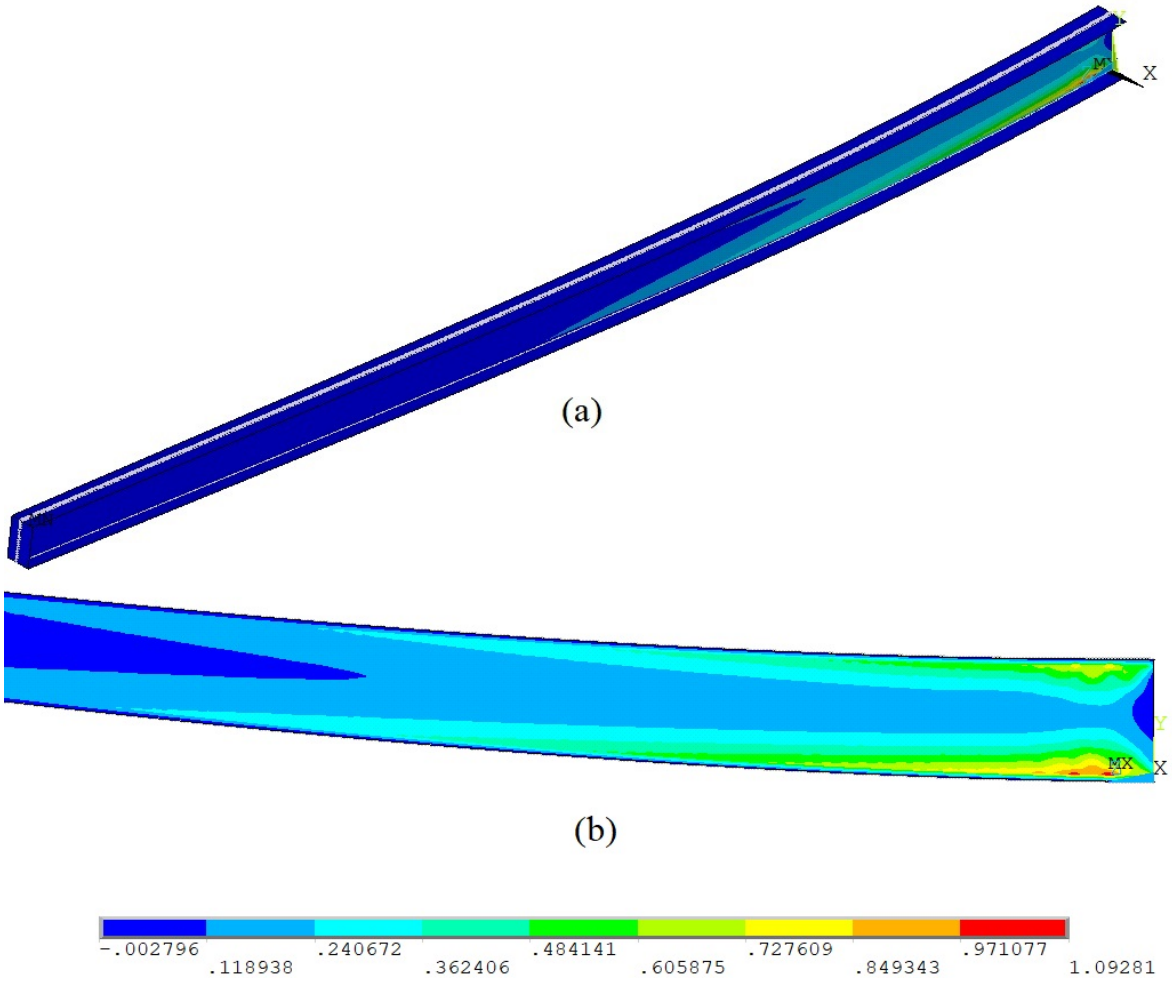

Figure 6.3. The distribution of Tsai-Wu index of the buckled spar with 4 mm-thick flat web from (a) isometric and (b) right views.

After obtaining the results for the spar with the flat web, the optimized spars with corrugated one are analyzed and their results are presented in the next sections.

6.2. Spars with Corrugated Web

The optimization procedure is applied to the model with a 1.5 mm-thick web. Besides, a spar beam with 1.0 mm-thick web is optimized to see whether it can support the load without buckling. The optimum designs of the spar beams for both of thicknesses are examined in this chapter.

To start the optimization process, a model is selected firstly for both spars. Their design parameter values are calculated as follows.

$$w_{1,ini} = \frac{w_{1,max} + w_{1,min}}{2} \tag{6.1}$$

$$i_{ini} = \frac{i_{max} + i_{min}}{2} \tag{6.2}$$

$$a_{1,ini} = \frac{a_{1,max} + a_{1,min}}{2} \tag{6.3}$$

$$a_{f,ini} = \frac{a_{f,max} + a_{f,min}}{2} \tag{6.4}$$

The model with these design parameter values is shown in Figure 6.4.

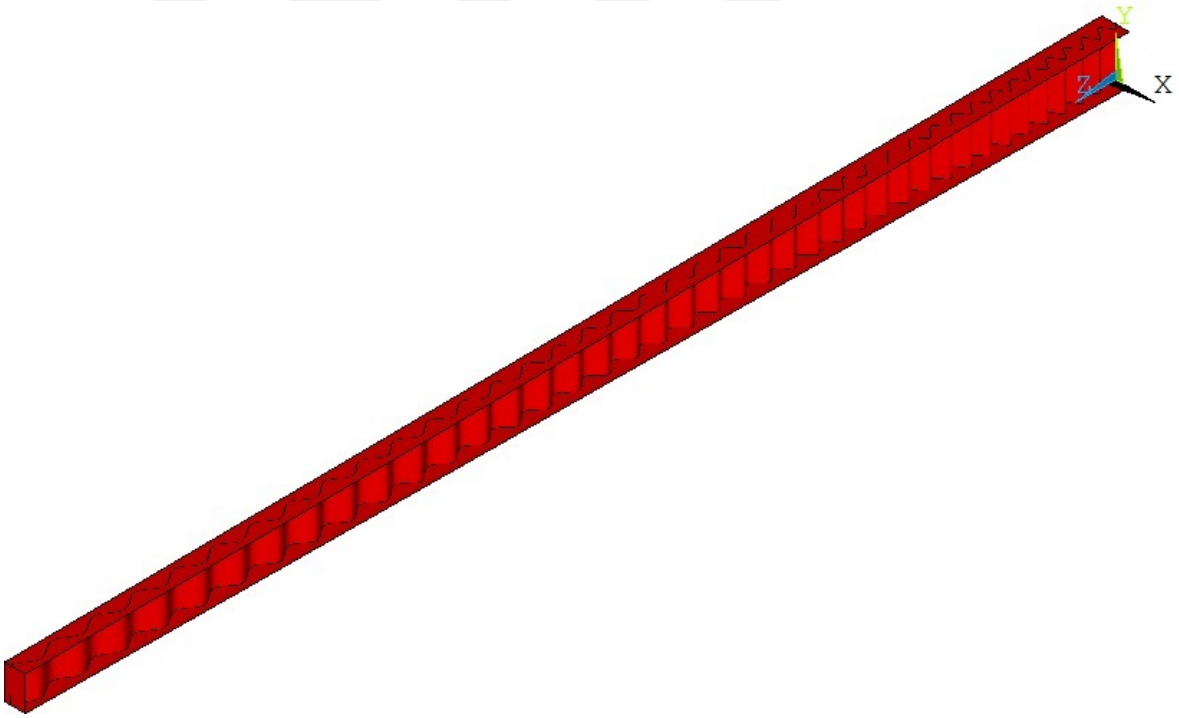

Figure 6.4. Initial design of the spar.

6.2.1. Model with 1.5 mm Web Thickness

After applying the optimization procedure, the optimally shaped spar beam with 1.5 mm web thickness is obtained with the web wave parameter values given in Table 6.1.

Table 6.1. Wave parameter values of the spar with 1.5 mm-thick corrugated web.

Initial Wavelength w_1 **[mm]**	70.641
Wavelength Increment Rate i	1.006
Initial Amplitude a_1 **[mm]**	3.990
Final Amplitude a_f **[mm]**	0.423

The model with these parameter values is presented in Figure 6.5.

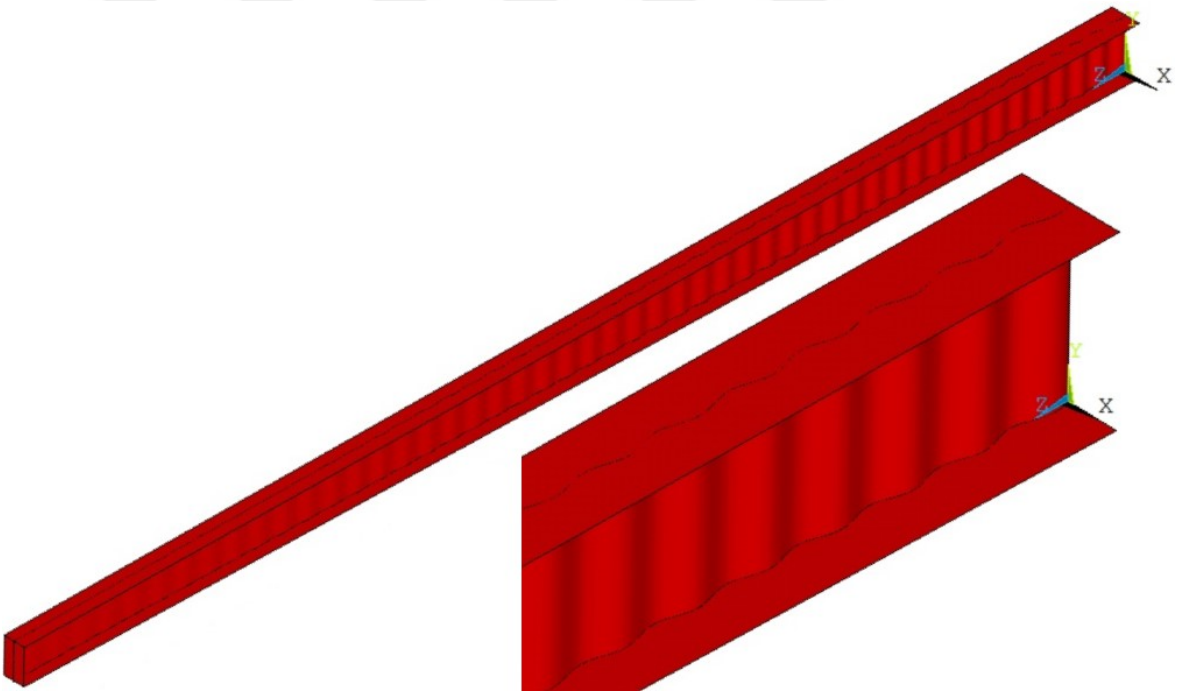

Figure 6.5. The last design of the spar with 1.5 mm-thick corrugated web with a close view from the fixed side.

The actual load 112 kN is applied to the optimized beam to examine its failure behavior. The displacement in the x-direction and Tsai-Wu index distributions of the buckled beam under 112 kN are given in Figure 6.6 and 6.7 respectively.

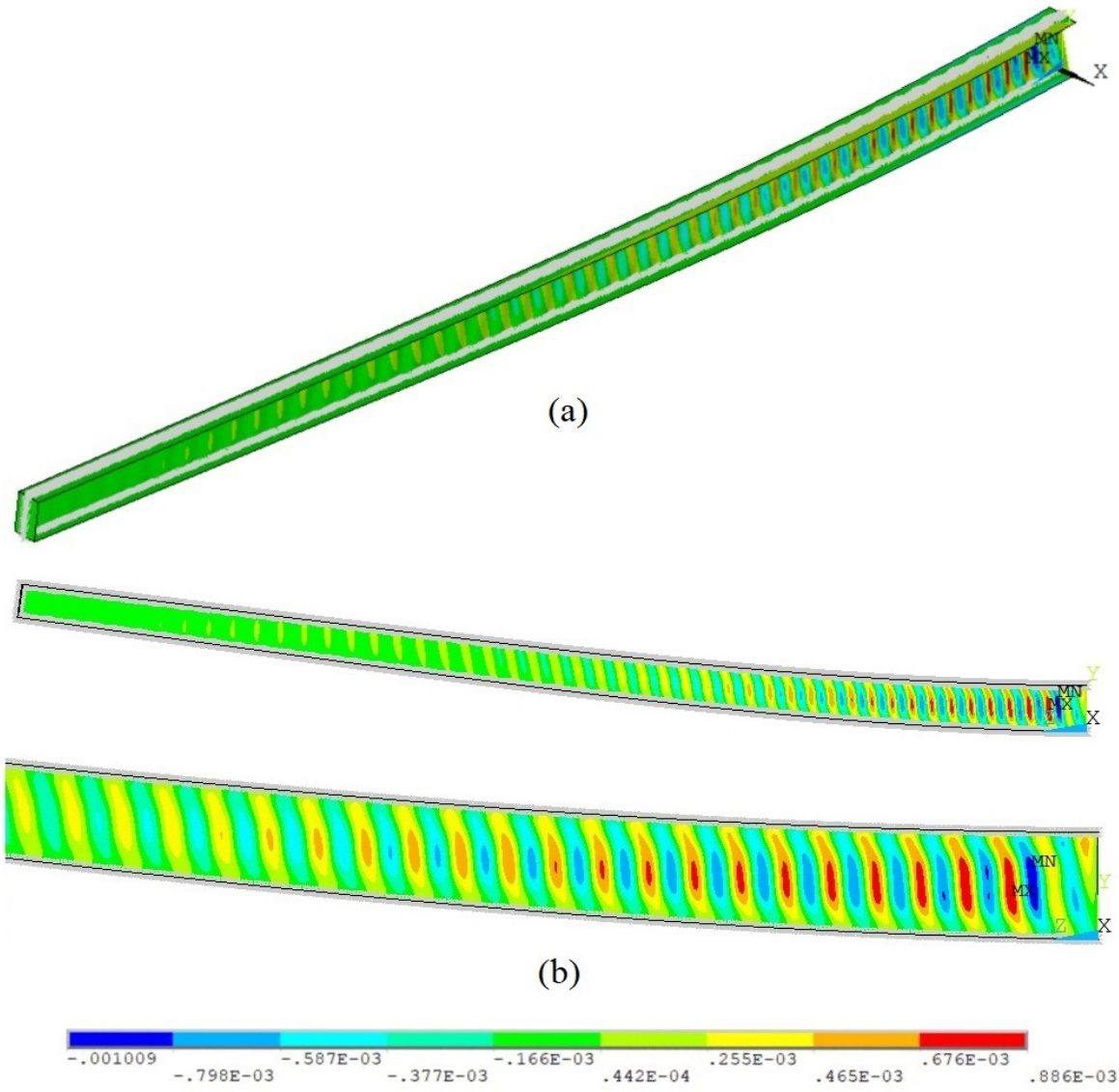

Figure 6.6. The distribution of the displacement in meters in the x-direction of the spar with 1.5 mm-thick web under 112 kN from (a) isometric and (b) right views with closer one.

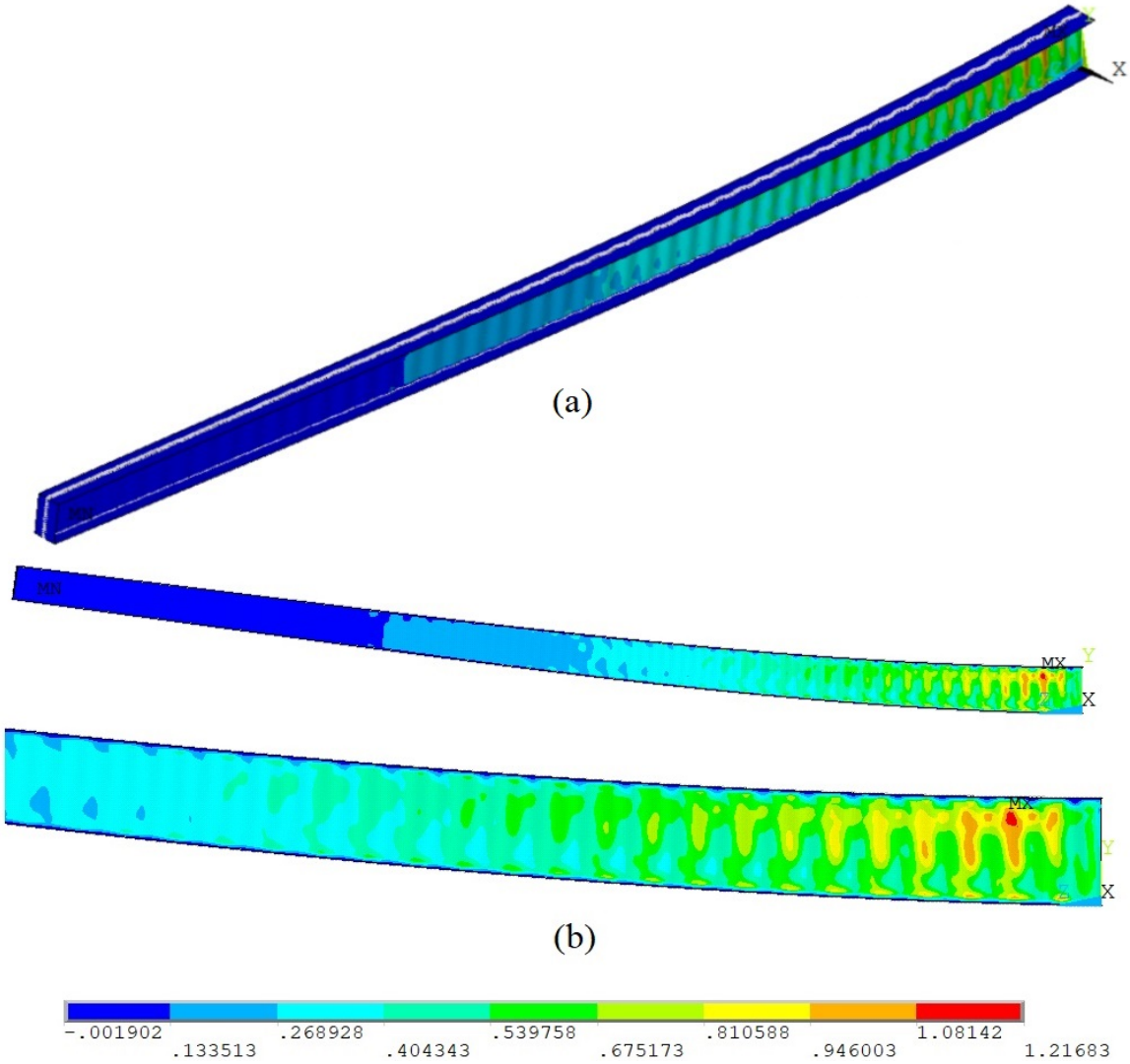

Figure 6.7. The distribution of Tsai-Wu index of the spar with 1.5 mm-thick web under 112 kN from (a) isometric and (b) right views with closer one.

As can be seen in Figure 6.6 and Figure 6.7, buckling and material failure started at 112 kN before the critical buckling load of 120 kN. However, the load factor of this part is obtained as 0.64630789. Being greater than 0.6 shows that this spar can carry the load a little bit more until a considerably high deformation occurs or high Tsai-Wu index value is reached. This is probably because of the high stability of the corrugated structure.

As be clearly seen from Figure 6.7, the most critical region of the beam in terms of the material failure is the upper and fixed root side of the web. It is due to the compression effect in that area. But this situation does not create a problem since there will be used L-joints between the flanges and the web to attach them together in real life usage. Those elements provide great support to the parts from the edges. Furthermore, the fixed side of the beam can be strengthened by extra several plies.

6.2.2. Model with 1.0 mm Web Thickness

After optimizing the spar with 1.5 mm-thick web, the same optimization procedure is also applied to the spar beam with 1.0 mm web thickness. The optimally shaped spar web has the dimensions given in Table 6.2.

Table 6.2. Wave parameter values of the spar with 1.0 mm-thick corrugated web.

Initial Wavelength w_1 **[mm]**	36.731
Wavelength Increment Rate i	1.013
Initial Amplitude a_1 **[mm]**	5.448
Final Amplitude a_f **[mm]**	0.263

As seen in Table 6.2 and Figure 6.8 this spar has more dense corrugation at the fixed root side than the former one.

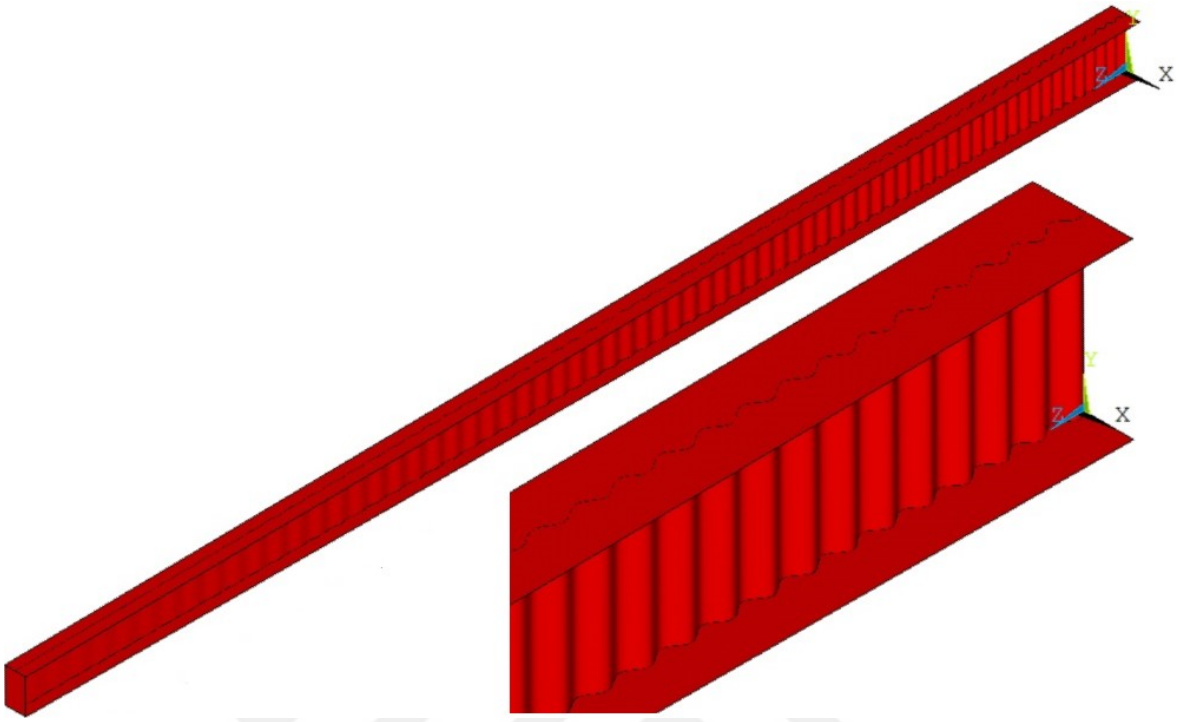

Figure 6.8. The last design of the spar with 1.0 mm-thick corrugated web with a close view from the fixed side.

The actual load 112 kN is applied to the optimized beam to examine its failure behavior. The displacement in the x-direction and Tsai-Wu index distributions of the buckled spar under 112 kN are given in Figure 6.9 and 6.10 respectively.

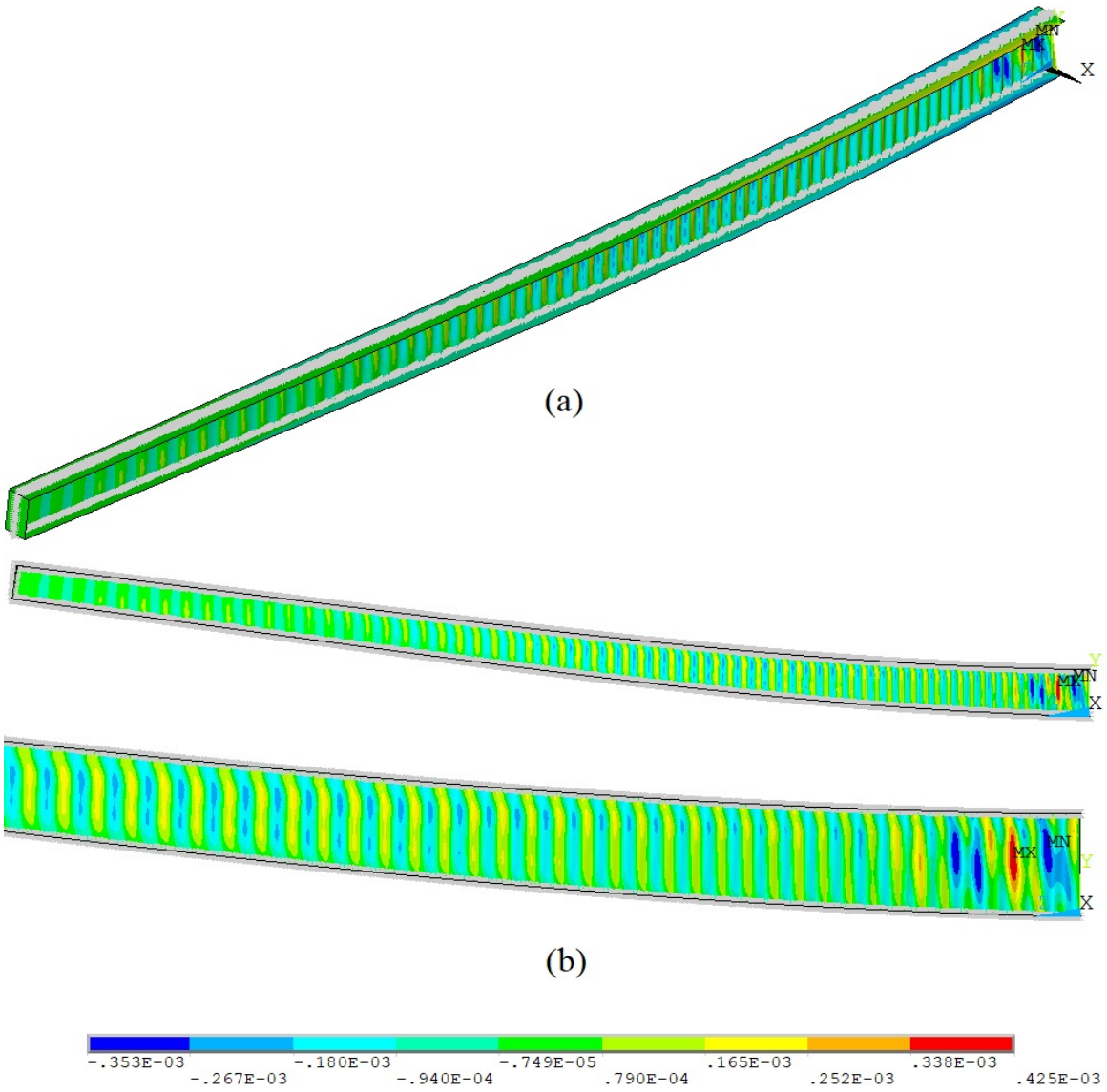

Figure 6.9. The distribution of the displacement in meters in the x-direction of the spar with 1.0 mm-thick web under 112 kN from (a) isometric and (b) right views with closer one.

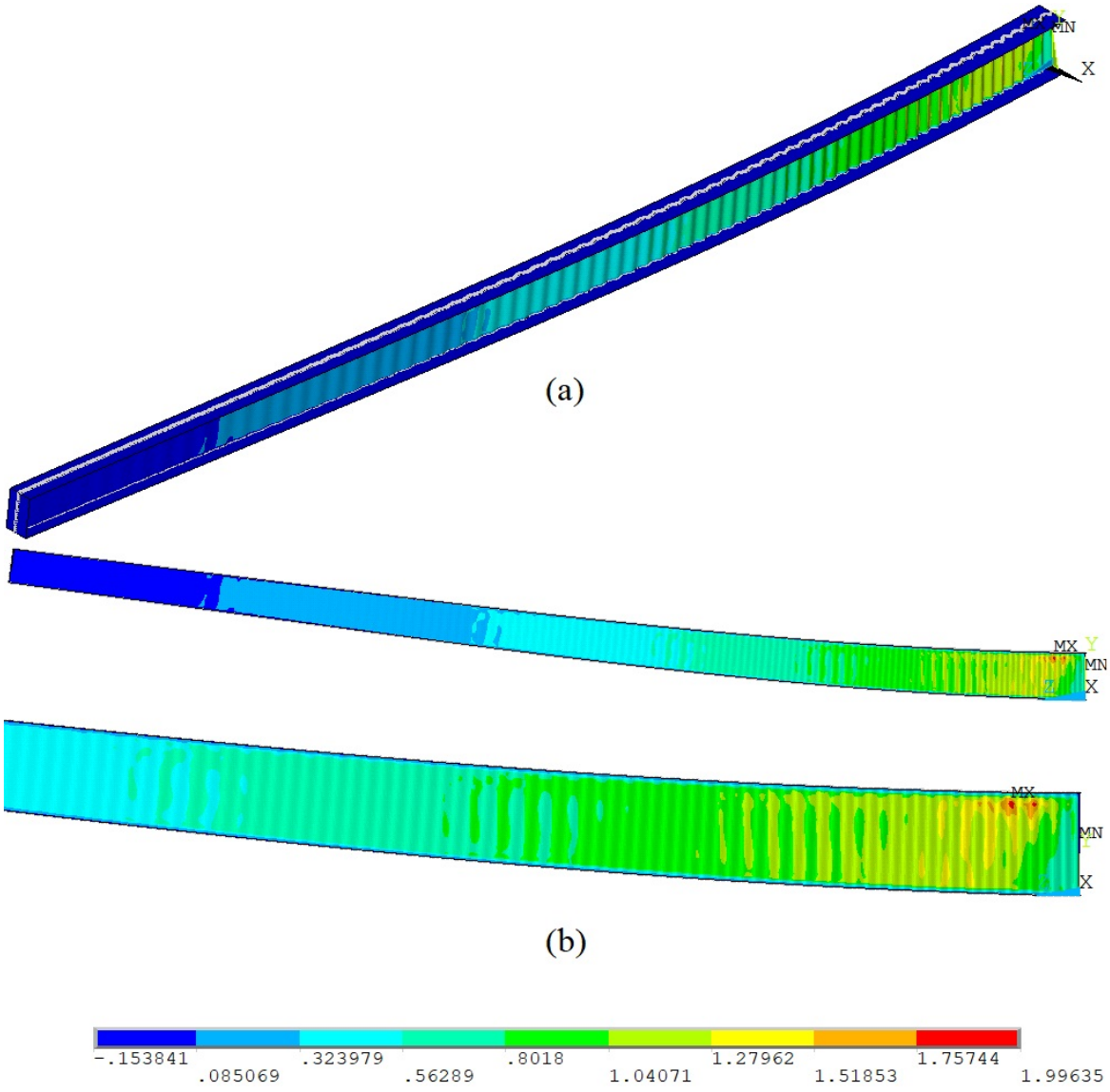

Figure 6.10. The distribution of Tsai-Wu index of the spar with 1.0 mm-thick web under 112 kN from (a) isometric and (b) right views with closer one.

As can be seen in Figure 6.9 and Figure 6.10, buckling and material failure started at 112 kN before the critical buckling load 120 kN. However, it can carry the load a little bit more until a large deformation occurs or high Tsai-Wu index value is reached. This is presumably because of the high stability of the wavy corrugated structure.

Likewise the spar with 1.5 mm-thick corrugated web, as seen in Figure 6.10 the most critical region for the material failure is top and fixed root side of the web of this

spar, too. Nevertheless, it will not be a problem thanks to the support of the joint elements and the fixed side can also be supported with extra plies as mentioned in the previous section.

6.3. Comparison of the Models

To compare the masses of these alternative designs, spar beams with various web shapes and thicknesses are given in Table 6.3 with their total and web masses.

Table 6.3. Total and web masses of the spar beams used in this thesis.

	Spar Number	**Web Mass [kg]**	**Total Mass [kg]**
4.0 mm-thick Flat Web	1	3.814	18.568
1.5 mm-thick Web with Constant Corrugation	2	2.267	17.021
1.5 mm-thick Web with Optimized Corrugation	3	1.444	16.198
1.0 mm-thick Web with Optimized Corrugation	4	0.994	15.743

The spar having web with constant corrugation is added to Table 6.3 to see the difference between the spars with web having constant and varying wave shapes through the length. $w_{1,ini}$ and $a_{1,ini}$ values given in Eq. 6.1 and 6.3 are used for its constant wave shape parameters.

Considering number two the conventional spar and number three the optimized one with the methodology developed in this study, the mass of the web is decreased by 36.3%. Additionally, a spar with 1.0 mm web thickness could also be designed according to this method and 56.2% mass reduction is obtained with this new design.

These two optimized spar webs especially provide a great reduction in mass when compared with the beam having a flat web. The mass of the web of number three spar is 62.1% and the other one is 73.9% less than the mass of the flat web. The mass change can more easily be seen from Figure 6.11.

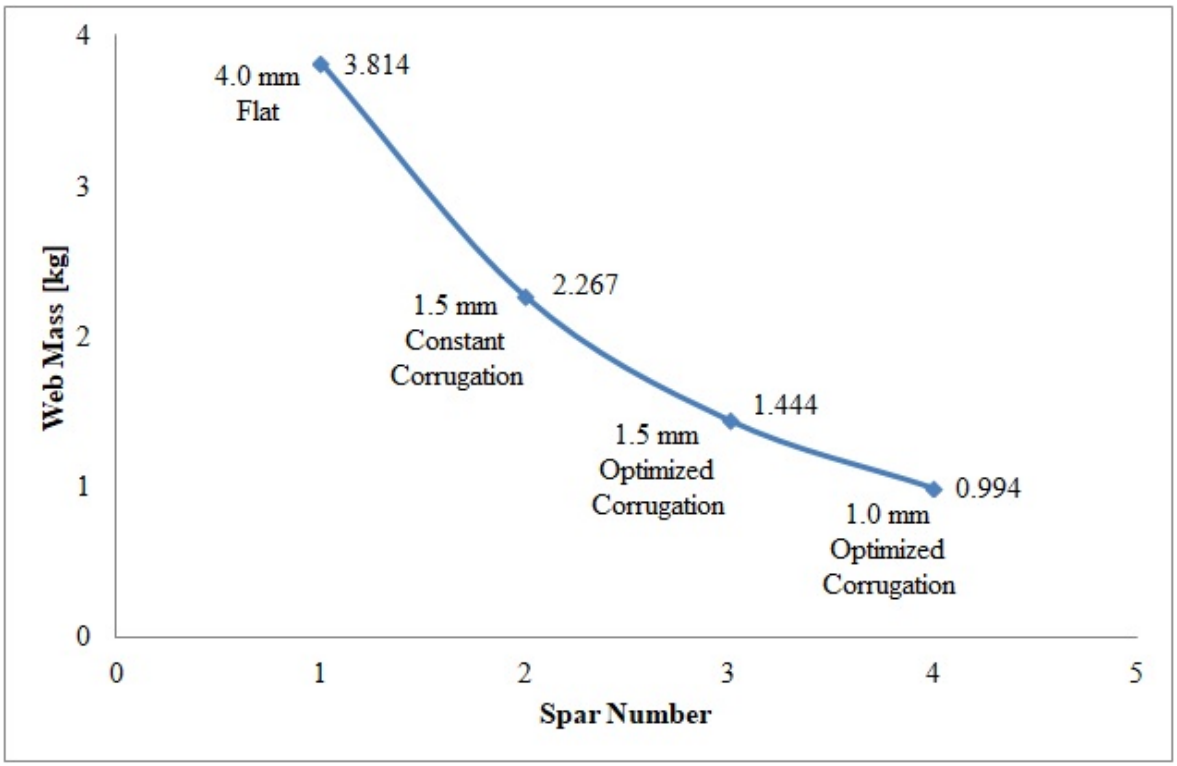

Figure 6.11. Comparison of the web masses of the four spars.

On the other hand, if the spars are compared with their total masses by adding the flanges and free end cover the differences in terms of the mass is relatively less because the thicknesses of the flanges are much greater than the web. The change graph is shown in Figure 6.12.

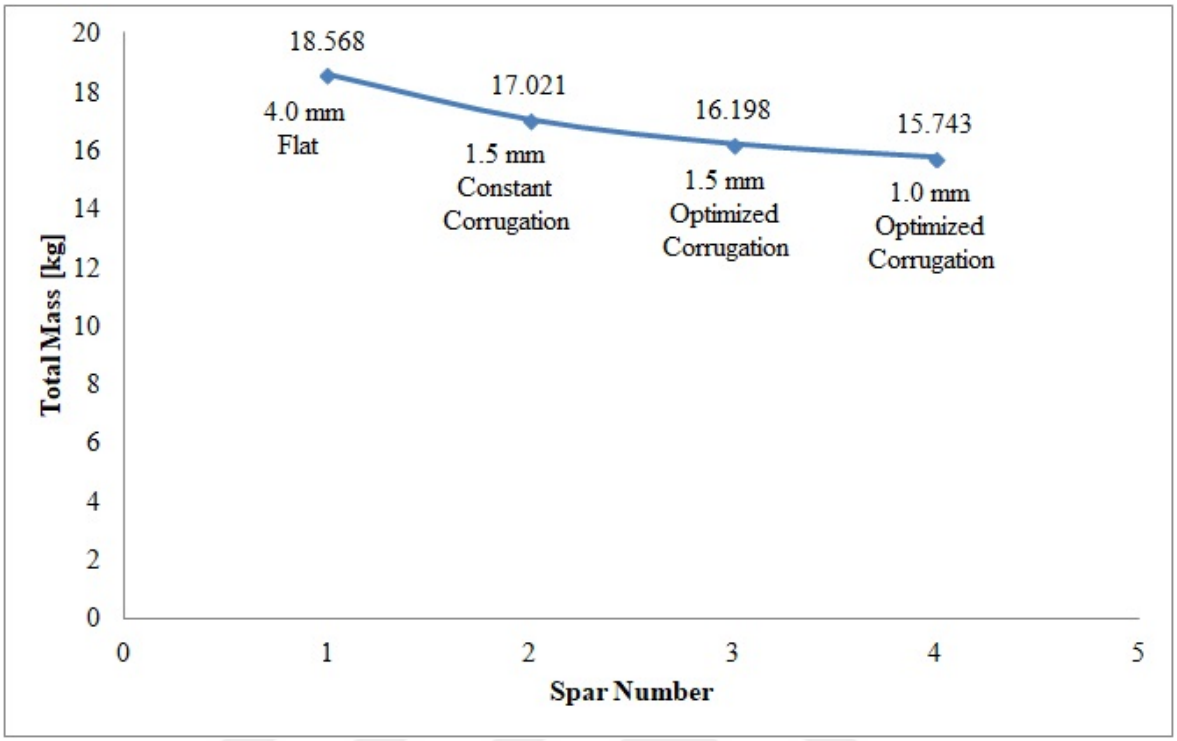

Figure 6.12. The change of total mass of the four spars.

The effect of the web mass change can be increased by designing the flanges and the cover thinner by changing their fiber orientation or material type. But this is out of the scope of this thesis.

7. CONCLUSION

In this study, a parametric model using codes in APDL and a design optimization methodology are developed for composite I-beam wing spars with a wavy corrugated web to minimize the mass by optimizing the shape of its web. The mechanical behavior of the beam under aerodynamic loading conditions is determined using finite element method.

The web is designed as a wave with varying wavelength and amplitude through the beam. According to the assigned values for these web parameters and the general spar dimensions, the key points are defined, and spline curves are generated by passing through these key points. Since the total number of key points changes depending on the assigned values for initial wavelength and wavelength increment rate, the key point numbers are defined as variable.

Because the main failure mode for thin webs is shear buckling, nonlinear buckling analyses are carried out by increasing loads step by step using the Arc-Length method. The mesh sizes are firstly determined by comparing the results obtained from a model with a wavy corrugated web made of an isotropic material under three-point bending with the ones obtained from the mathematical formulations and experimental data given in various technical documents. The accuracy of the results is found to be within acceptable limits. Then, the selected mesh sizes are adapted to the composite wing spar model.

The lift as the most dominant load carried by spars is applied to the model. It is analytically calculated considering the maximum g limits and a generally used safety factor. The calculated load is distributed non-uniformly along the length using a formula in the literature. Number of plies and fiber orientations are determined via a parametric study.

At last, the design optimization procedure is applied to two spar models with

different web thicknesses using a modified simulated annealing method that searches directly the globally optimal design rather than the local ones. The developed code found a design having denser web corrugation for the spar with a thinner web than the other one. Both of the optimally designed spar webs showed a significant decrease in mass. These models are also examined for the static failure using Tsai-Wu criterion. In this way, the most critical regions on the optimized spar beams in terms of the material failure are determined as the upper and fixed root side of the web due to the compression effect in that area. Solutions are discussed on these cases.

Consequently, the developed methodology works properly for the goal. Thanks to this methodology, any I-beam wing spar model with a wavy corrugated web can be easily designed with minimum mass for desired dimensions and loads.

7.1. Future Work Recommendations

The model is developed for the same thickness along the beam. However, the thicknesses can be adjusted as variable through the free end to improve the design. A new algorithm can be developed by adding the thickness parameters for the optimization.

In addition to the buckling constraint, deflection at the free end can also be given as another constraint for the optimization procedure. Nevertheless, the dominant factor on deflection is flanges, not the web.

REFERENCES

1. The World Bank, *Air transport, passengers carried*, https://data.worldbank.org/indicator/IS.AIR.PSGR?end=2015&start=1970&view=chart, accessed at December 2018.

2. Kumar, T. S. V., A. W. Basha, M. Pavithra and V. Srilekha, "Static & Dynamic Analysis of a Typical Aircraft Wing Structure Using MSC Nastran", *International Journal of Research in Aeronautical and Mechanical Engineering*, Vol. 3, pp. 1–12, 2015.

3. Quora Inc., *Aviation: What is Wing Spar, Ribs?*, 2018, https://www.quora.com/Aviation-What-is-Wing-Spar-Ribs, accessed at December 2018.

4. Sohaib, M., *Parameterized Automated Generic Model for Aircraft Wing Structural Design and Mesh Generation for Finite Element Analysis*, Master Thesis, Linköpings University, 2011.

5. Kumaraswamy, T., S. Nadakuditi and M. S. Gupta, "Analysis and Fabrication of Composite Wing Spar", *International Journal & Magazine of Engineering, Technology, Management and Research*, Vol. 3, pp. 648–661, 2016.

6. Mohamed, H. A. and S. Nithiyakalyani, "Design and Structural Analysis of the Ribs and Spars of Swept Back Wing", *International Journal of Emerging Technology and Advanced Engineering*, Vol. 4, pp. 208–213, 2014.

7. Wan, Z., D. Liu, C. Tang and C. Yang, "Studies on the influence of spar position on aeroelastic optimization of a large aircraft wing", *Science China Technological Sciences*, Vol. 55, pp. 117–124, 2012.

8. Lickley, R. L., *Aircraft Construction: A Review of Modern Stressed Skin Systems*, Wilkinson Rubber Linatex Ltd., 1-4, Great Tower St., London, E.C.3., 1940.

9. *Aviation Maintenance Technician Handbook – Airframe. Chapter 1: Aircraft Structures*, Vol. 1, U. S. Department of Transportation Federal Aviation Administration, 2012.

10. Grbovic, A. and B. Rasuo, "FEM based fatigue crack growth predictions for spar of light aircraft under variable amplitude loading", *Engineering Failure Analysis*, Vol. 26, pp. 50–64, 2012.

11. Suzuki, S., "Multigoal Programming for Structure-Control Design Synthesis with Fuzzy Goals", *JSME International Journal*, Vol. 38, pp. 450–456, 1995.

12. Visnjic, G., D. Nozak, F. Kosel and T. Kosel, "Reducing shear-lag in thin-walled composite I-beam wing spars", *Aircraft Engineering and Aerospace Technology: An International Journal*, Vol. 86, pp. 89–98, 2014.

13. Visnjic, G., D. Nozak, F. Kosel and T. Kosel, "Shear-lag influence on maximum specific bending stiffness and strength of composite I-beam wing spar", *Proceedings of the Institution of Mechanical Engineers, Part G: Journal of Aerospace Engineering*, Vol. 225, pp. 501–511, 2010.

14. Robertson, C. D., *Structural Characterization, Optimization, and Failure Analysis of a Human-Powered Ornithopter*, Master Thesis, University of Toronto, 2009.

15. Fałek, M., E. Szymczyk and J. Jachimowicz, "Study on Possible Replacement of the Aluminum Spar with a Composite Structure Illustrated with the Case of Agricultural Aircraft", *Fatigue of Aircraft Structures*, Vol. 2017, pp. 85–99, 2017.

16. Ferro, C. G., A. Mazza, D. Belmonte, C. Secli and P. Maggiore, "A comparison between 3D Printing and Milling Process for a Spar Cap Fitting (wing-fuselage) of UAV Aircraft", *10th CIRP Conference on Intelligent Computation in Manufacturing Engineering - CIRP ICME '16*, Vol. 62, pp. 487–493, 2017.

17. Maute, K. and M. Allen, "Conceptual design of aeroelastic structures by topology

optimization", *Structural and Multidisciplinary Optimization*, Vol. 27, pp. 27–42, 2004.

18. Kumar, A. R., S. R. Balakrishnan and S. Balaji, "Design of an Aircraft Wing Structure for Static Analysis and Fatigue Life Prediction", *International Journal of Engineering Research and Technology*, Vol. 2, pp. 1154–1158, 2013.

19. Bruce, R. R. J. and S. Priyadharshini, "Initial and Progressive Failure Analysis of a Composite Wing Spar Structure", *Journal of Mechanical Engineering*, Vol. 14, pp. 169–185, 2017.

20. Shabeer, K. P. and M. A. Murtaza, "Optimization of Aircraft Wing with Composite Material", *International Journal of Innovative Research in Science, Engineering and Technology*, Vol. 2, pp. 2471–2477, 2013.

21. Wang, G., J. Zeng, J. Lee, X. Du and X. Shan, "Preliminary Design of a Truss-Braced Natural-Laminar-Flow Composite Wing via Aeroelastic Tailoring", *Journal of Aeroelasticity and Structural Dynamics*, Vol. 3, pp. 1–17, 2015.

22. Ajith, V. S., R. Paramasivam and K. Vidhya, "Study of Optimal Design of Spar Beam for the Wing of an Aircraft", *International Journal of Engineering Development and Research*, Vol. 5, pp. 179–193, 2017.

23. Vinoth, R. A. and T. Raghu, "Topology Design Optimization of Ribs, Spars, Wing Attachment Bulkhead and Nose Landing Gear Bracket", *International Journal of Research in Aeronautical and Mechanical Engineering*, Vol. 3, pp. 16–35, 2015.

24. Lim, J., S. Choi, S. Shin and D. Lee, "Wing Design Optimization of a Solar-HALE Aircraft", *International Journal of Aeronautical and Space Sciences*, Vol. 15, pp. 219–231, 2014.

25. James, K., *Aerostructural Shape and Topology Optimization of Aircraft Wings*, Ph.D. Thesis, University of Toronto, 2012.

26. Arévalo, P. T., *Design Optimization of a Composite Wing Box for High-Altitude Long-Endurance Aircraft*, Master Thesis, Embry-Riddle Aeronautical University, 2014.

27. Park, H., "A study on forced vibration behaviors of composite main wing structure of the 20 seat class small scale WIG craft", *Aerospace Science and Technology*, Vol. 29, pp. 445–452, 2013.

28. Fleuret, C., A. Andreani, E. Laine, J. Grandidier, S. L'heritier and A. Gorge, "Complex wing spar design in carbon fiber reinforced composite for a light aerobatic aircraft", *Mechanics & Industry*, Vol. 17, pp. 614–632, 2016.

29. Li, H., L. Zhu, G. Sun, M. Dong and J. Qiao, "Deflection monitoring of thin-walled wing spar subjected to bending load using multi-element FBG sensors", *Optik*, Vol. 164, pp. 691–700, 2018.

30. Stanford, B. K. and P. D. Dunning, "Optimal Topology of Aircraft Rib and Spar Structures Under Aeroelastic Loads", *Journal of Aircraft*, Vol. 52, pp. 1298–1311, 2015.

31. Bhachu, K. S., R. T. Haftka, G. Waycaster and N. H. Kim, "Probabilistic Manufacturing Tolerance Optimization of Damage-Tolerant Aircraft Structures Using Measured Data", *Journal of Aircraft*, Vol. 52, pp. 1412–1421, 2015.

32. Bhachu, K. S., R. T. Haftka and N. H. Kim, "Quantifying Effect of Uncertainty Sources on Optimum in Tolerance Optimization", *10th World Congress on Structural and Multidisciplinary Optimization*, 2013.

33. Petrašinović, N., D. Petrašinović, B. Rašuo and D. Milković, "Aircraft Duraluminum Wing Spar Fatigue Testing", *FME Transactions*, Vol. 45, pp. 531–536, 2017.

34. Best, P. E., "Analysis and Comparison of I-Beam and Solid Wing Spars", *Sport*

Aviation, pp. 38–42, 1961.

35. Rais-Rohani, M. and Z. Huo, "Analysis and Optimization of Primary Aircraft Structures Based on Strength, Manufacturability, and Cost Requirements", *40th AIAA/ASME/ASCE/AHS/ASC Structures, Structural Dynamics and Materials Conference*, 1999.

36. Diganth, K. B. N. and K. M. Dutt, "Damage Tolerance Evaluation of the Front Spar in a transport aircraft wing", *International Journal of Innovative Research in Science, Engineering and Technology*, Vol. 2, pp. 5048–5055, 2013.

37. Martinez, M. P., A. Messac and M. Rais-Rohani, "Manufacturability Based Optimization of Aircraft Structures Using Physical Programming", *AIAA Journal*, Vol. 39, pp. 517–525, 2001.

38. Xie, Q. and M. Rais-Rohani, "Probabilistic Design Optimization of Aircraft Structures with Reliability, Manufacturability, and Cost Constraints", *4th AIAA/ASME/ASCE/AHS/ASC Structures, Structural Dynamics, and Materials Conference*, 2003.

39. Stepanova, L. N., E. S. Petrova and V. V. Chernova, "Strength Tests of a CFRP Spar Using Methods of Acoustic Emission and Tensometry", *Russian Journal of Nondestructive Testing*, Vol. 54, pp. 243–248, 2018.

40. Horan, P., P. R. Underhill and T. W. Krause, "Pulsed eddy current detection of cracks in F/A-18 inner wing spar without wing skin removal using Modified Principal Component Analysis", *NDT & E International*, Vol. 55, pp. 21–27, 2013.

41. Solovyev, P., A. Gomzin, Y. Pervushin, F. Musin and S. Galyshew, "Structure determination and composite wing spar stress-strain state estimation", *International Conference on Modern Trends in Manufacturing Technologies and Equipment*, Vol. 129, 2017.

42. Cesnik, C. E. S., D. H. Hodges and M. J. Patil, "Aeroelastic Analysis of Composite Wings", *Proceedings of the 37th Structures, Structural Dynamics and Materials Conference*, pp. 1113–1123, 1996.

43. Alsahlani, A., T. Rahulan and N. Abdulhassan, "Composite Structural Analysis of a High Altitude, Solar Powered Unmanned Aerial Vehicle", *International Journal of Mechanical Engineering and Robotics Research*, Vol. 6, pp. 71–76, 2017.

44. Afifi, H. A., E. Nikolaidis, E. K. Afifi and S. N. Gangadharan, "A Combined Approximation Based MATLAB Code for Dynamic Re-Analysis of Aerospace Structures", *Proceedings of the ASME 2009 International Mechanical Engineering Congress & Exposition*, Vol. 13, pp. 97–104, 2009.

45. da Silva, C. M. B. P., *Design and Testing of an Active Aircraft Wing Spar with Bending-Torsion Coupling*, Master Thesis, University of Victoria, 2007.

46. Ajaj, R. M., M. I. Friswell, W. G. Dettmer, G. Allegri and A. T. Isikveren, "Conceptual Modeling of an Adaptive Torsion Wing Structure", *52nd AIAA/ASME/ASCE/AHS/ASC Structures, Structural Dynamics and Materials Conference*, 2011.

47. Blondeau, J., J. Richeson and D. J. Pines, "Design, development and testing of a morphing aspect ratio wing using an inflatable telescopic spar", *44th AIAA/ASME/ASCE/AHS Structures, Structural Dynamics, and Materials Conference*, 2003.

48. Kota, S., J. Hetrick and L. Saggere, *Design of a Variable Stiffness Spar*, CSA Engineering, Inc., Palo Alto, CA, USA, 2017.

49. Ajaj, R. M., M. I. Friswell, M. Bourchak and W. Harasani, "Span morphing using the GNATSpar wing", *Aerospace Science and Technology*, Vol. 53, pp. 38–46, 2016.

50. Woods, B. K. S. and M. I. Friswell, "The Adaptive Aspect Ratio Morphing Wing:

Design Concept and Low Fidelity Skin Optimization", *Proceedings of the ASME 2014 Conference on Smart Materials, Adaptive Structures and Intelligent Systems*, 2014.

51. Ajaj, R. M., E. I. S. Flores, M. I. Friswell, G. Allegri, B. K. S. Woods, A. Isikveren and W. G. Dettmer, "The Zigzag wingbox for a span morphing wing", *Aerospace Science and Technology*, Vol. 28, pp. 364–375, 2013.

52. Marqui, C. D., W. G. R. Vieira, A. Erturk and D. J. Inman, "Modeling and Analysis of Piezoelectric Energy Harvesting from Aeroelastic Vibrations Using the Doublet-Lattice Method", *Journal of Vibration and Acoustics*, Vol. 133, 2011, 011003.

53. Anton, S. R. and D. J. Inman, "Performance modeling of unmanned aerial vehicles with on-board energy harvesting", *Proceedings of SPIE - The International Society for Optical Engineering*, Vol. 7977, 2011, 79771H.

54. Wang, Y. and D. J. Inman, "Simultaneous energy harvesting and gust alleviation for a multifunctional composite wing spar using reduced energy control via piezoceramics", *Journal of Composite Materials*, Vol. 47, pp. 125–146, 2013.

55. Baucom, J. N., J. P. Thomas, W. R. P. III and M. A. Qidwai, "Autophagous structure-power systems", *Proceedings of SPIE - The International Society for Optical Engineering*, Vol. 5387, pp. 96–105, 2004.

56. Robinson, J., S. Doyle, G. Ogawa, , M. Baker, S. De, M. Jrad and R. Kapania, "Aeroelastic Optimization of Wing Structure Using Curvilinear Spars and Ribs (SpaRibs)", *17th AIAA/ISSMO Multidisciplinary Analysis and Optimization Conference*, 2016.

57. Locatelli, D., *Optimization of Supersonic Aircraft Wing-Box Using Curvilinear SpaRibs*, Ph.D. Thesis, Virginia Polytechnic Institute and State University, 2012.

58. Locatelli, D., S. B. Mulani and R. K. Kapania, "Supersonic Wing Box Weight Optimization Using Curvilinear Spars and Ribs (SpaRibs)", *51st AIAA/ASME/ASCE/AHS/ASC Structures, Structural Dynamics, and Materials Conference*, 2010.

59. Calogero, J. P., M. I. Frecker, Z. Hasnain and J. E. H. Jr, "A dynamic spar numerical model for passive shape change", *Smart Materials and Structures*, Vol. 25, 2016, 104006.

60. Wissa, A., N. Guerreiro, J. A. Grauer, J. Hubbard, M. Frecker, C. Altenbuchner, Y. Tummala and R. Roberts, "Flight Testing of Novel Compliant Spines for Passive Wing Morphing on Ornithopters", *54th AIAA/ASME/ASCE/AHS/ASC Structures, Structural Dynamics, and Materials Conference*, 2013.

61. Ajaj, R. M., E. I. S. Flores, M. I. Friswell and F. A. D. D. la O, "Span Morphing Using the Compliant Spar", *Journal of Aerospace Engineering*, Vol. 28, 2015.

62. McCarville, D. A. and R. E. Bahr, "Composite sine wave spar", U.S. Patent 5 919 543, Jul. 6, 1995.

63. Gillespie, T. E., "Reduced Amplitude Corrugated Web Spar", European Patent Application 0814018 A2, Dec. 29, 1997.

64. Engineering ToolBox, *Cantilever Beams - Moments and Deflections.*, 2013, `https://www.engineeringtoolbox.com/cantilever-beams-d_1848.html`, accessed at December 2018.

65. EngineeringCivil.org, *Lateral Torsional Buckling - Factors influencing LTB*, 2017, `https://engineeringcivil.org/articles/civil-engineering/lateral-torsional-buckling-factors-influencing-ltb/`, accessed at December 2018.

66. Teng, J. G., D. Fernando and T. Yua, "Finite element modelling of debonding

failures in steel beams flexurally strengthened with CFRP laminates", *Engineering Structures*, Vol. 86, pp. 213–224, 2015.

67. LUSAS, *Making the Most of Eurocodes for Critical Buckling Analysis*, 2018, `http://www.lusas.com/case/bridge/critical_buckling_analysis.html`, accessed at December 2018.

68. Aerospace Engineering Blog, *The Mystery of Wing Twisting*, 2017, `https://aerospaceengineeringblog.com/the-mystery-of-wing-twisting/`, accessed at December 2018.

69. The LTAS-Computational & Multiscale Mechanics of Materials (CM3) laboratory, *Fracture Mechanics Online Class - Brittle and Ductile Materials*, 2015, `http://www.ltas-cm3.ulg.ac.be/FractureMechanics/?p=overview_P3`, accessed at December 2018.

70. Çalışkan, S., *Mechanical Properties of Non-Crimp Fabric (NCF) Fiberglass Reinforced Composite Materials Manufactured by Using Vacuum Infusion Process*, Master Thesis, Boğaziçi University, 2009.

71. Budiansky, B. and N. Fleck, "Compressive kinking of fiber composites: A topical review", *Applied Mechanics Reviews*, Vol. 47, pp. 246–250, 1994.

72. Karbhari, V., *Non-Destructive Evaluation (NDE) of Polymer Matrix Composites: Techniques and Applications*, Woodhead Publishing, 2013.

73. Choo, V. K. S., *Fundamentals of Composite Materials*, Knowen Academic Press, Dover, DE, USA, 1990.

74. Korkut, S., *Statik ve Dinamik Yükler Altında Kompozit Plakaların Hasar Durumlarına Karşı Davranışlarının İncelenmesi*, Master Thesis, İstanbul Technical University, 2017.

75. Tsai, S. W. and E. M. Wu, "A General Theory of Strength for Anisotropic Materials.", *Journal of Composite Materials*, Vol. 5, pp. 58–80, 1971.

76. SIMSOLID Corporation, *New Material Non-Linear Analysis Now Available in SIMSOLID*, 2018, `https://www.simsolid.com/2017/11/new-material-non-linear-analysis-now-available-in-simsolid/`, accessed at January 2019.

77. Vasios, N., *Nonlinear Analysis of Structures - The Arc Length Method: Formulation, Implementation and Applications*, Harvard University, Cambridge, MA, USA, 2015.

78. de Wec, O. and I. Y. Kim, *Design Optimization - Structural Optimization [Powerpoint slides]*, 2004, `http://web.mit.edu/16.810/www/16.810_L8_Optimization.pdf`.

79. Akbulut, M. and F. O. Sonmez, "Design optimization of laminated composites using a new variant of simulated annealing", *Computers and Structures*, Vol. 89, pp. 1712–1724, 2011.

80. Ledesma, S., G. Aviña and R. Sanchez, C. M. Tan (Editor), *Simulated Annealing*, chap. Practical Considerations for Simulated Annealing Implementation, pp. 401–420, I-Tech Education and Publishing, Vienna, Austria, 2008.

81. Henderson, D., S. H. Jacobson and A. W. Johnson, F. Glover and G. A. Kochenberger (Editors), *Handbook of Metaheuristics*, chap. The theory and practice of simulated annealing, pp. 287–319, Springer, Boston, MA, USA, 2006.

82. Gider, B., *Sine Wave Spar - Remarks on sizing [Powerpoint slides]*, 2017.

83. *Hürkuş Gelişmiş Eğitim / Hafif Taarruz Uçağı*, Türk Havacılık ve Uzay Sanayii, Kahramankazan, Ankara, Türkiye, 2018.

84. Shared Hierarchical Academic Research Computing Network, *SHELL181*, `https://www.sharcnet.ca/Software/Ansys/17.0/en-us/help/ans_elem/Hlp_E_SHELL181.html`, accessed at December 2018.

85. Kiymaz, G., E. Coskun, C. Cosgun and E. Seckin, "Transverse load carrying capacity of sinusoidally corrugated steel web beams with web openings", *Steel and Composite Structures*, Vol. 10, pp. 69–85, 2010.

86. *SINBEAM (Corrugated Web Beam)*, Zeman & Co Gesellschaft mbH, 2012.

87. Shared Hierarchical Academic Research Computing Network, *ARCLEN*, `https://www.sharcnet.ca/Software/Ansys/16.2.3/en-us/help/ans_cmd/Hlp_C_ARCLEN.html`, accessed at December 2018.

88. Quilter, A., "Composites in Aerospace Applications", *IHS White Paper*, 2001.

89. Kaddour, A. S., M. J. Hinton, P. A. Smith and S. Li, "Mechanical properties and details of composite laminates for the test cases used in the third world-wide failure exercise", *Journal of Composite Materials*, Vol. 47, pp. 2427–2442, 2013.

90. *Eurocode 3: Design of steel structures - Part 1-5: General rules - Plated structural elements (EN 1993-1–5, Annex D)*, European Committee for Standardization, 2006.

91. Timoshenko, S. and S. W. Krieger, *Theory of Plates and Shells*, McGraw-Hill Company, 2 edn., 1959.

92. *Beam Design Formulas with Shear and Moment Diagrams*, American Forest & Paper Association, Washington, DC, USA, 2007.

93. Erkol, V., *Shape Optimization of Notched Parts for Maximum Fatigue Life*, Master Thesis, Boğaziçi University, 2016.

94. Fischer, F. J. C., M. Beyrle, A. H. Thellmann, M. Endrass, T. Stefani, T. Gerngross

and M. Kupke, “Corrugated composites: production-integrated quality assurance in carbon fiber reinforced thermoplastic sine wave beam production”, *Advanced Manufacturing: Polymer & Composites Science*, Vol. 3, pp. 10–20, 2017.

APPENDIX A: SHEAR STRENGTH OF WAVY CORRUGATED WEBS

The calculation of the transverse force capacity of I-beams with wavy corrugated web is given by EN 1993-1-5 Annex D [90] in detail. The most general equation of the transverse shear load bearing capacity V_{Rd} is defined as follows.

$$V_{Rd} = \chi_c \frac{f_{yw}}{\gamma_{M1}\sqrt{3}} h_w t_w \tag{A.1}$$

where χ_c is the smaller of the local buckling of plates $\chi_{c,l}$ and the buckling of the web $\chi_{c,g}$ reduction values. f_{yw} is the yield strength of the material the web is made of, h_w and t_w are the height and the thickness of the web, respectively, and γ_{M1} is the global safety factor. The reduction factor for the local buckling of plates $\chi_{c,l}$ is calculated using the equation given below.

$$\chi_{c,l} = \frac{1.15}{0.9 + \overline{\lambda_{c,l}}} \leq 1.0 \tag{A.2}$$

As seen in Eq. A.2, if $\chi_{c,l}$ is greater than 1.0, it is defined as 1.0. It can only get value as 1.0 or less. $\overline{\lambda_{c,l}}$ is formulated as follows.

$$\overline{\lambda_{c,l}} = \sqrt{\frac{f_y}{\tau_{cr,l}\sqrt{3}}} \tag{A.3}$$

where f_y is the yield strength of the material of the plates and $\tau_{cr,l}$ is the critical stress value for local buckling that can be calculated using the following equation.

$$\tau_{cr,l} = \left(5.34 + \frac{as}{h_w t_w}\right) \frac{\pi^2 E}{12(1-\nu^2)} \left(\frac{t_w}{s}\right)^2 \tag{A.4}$$

where a is the height of the projected amplitude, s is the half of the length of the corrugation wave, E and ν are the elastic modulus and Poisson's ratio of the material of the web.

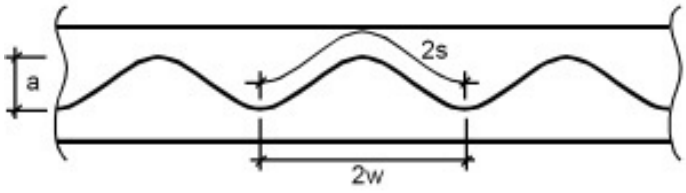

Figure A.1. Critical web dimensions [86].

s is determined by some developed formula in different resources that are given below.

$$s = \int_0^w \left(\sqrt{1 + \left[\frac{\pi a}{w} sin\left(\frac{2\pi x}{w} \right) \right]^2} \right) dx \tag{A.5}$$

Eq. A.5 is given in a technical document SINBEAM [86]. On the other hand, the unfolded length s is also more simply formulated by Timoshenko and Woinowsky-Krieger [91] as given below.

$$s = w \left(1 + \frac{\pi^2 a^2}{16 w^2} \right) \tag{A.6}$$

As seen in Figure A.1 w is the half of the wavelength.

The reduction factor for the buckling of the web $\chi_{c,g}$ is calculated by the equation below.

$$\chi_{c,g} = \frac{1.5}{0.5 + \overline{\lambda}_{c,g}^2} \leq 1.0 \tag{A.7}$$

Likewise $\chi_{c,l}$, $\chi_{c,g}$ is also considered as 1.0 while it is greater than 1. For this

reason, it can only be 1.0 or less, too. $\overline{\lambda_{c,g}}$ is found using the equation given below.

$$\overline{\lambda_{c,g}} = \sqrt{\frac{f_{yw}}{\tau_{cr,g}\sqrt{3}}} \tag{A.8}$$

where the transverse buckling stress $\tau_{cr,g}$ is found by the equation below.

$$\tau_{cr,g} = \frac{32.4}{t_w h_w^2} \sqrt[4]{D_x D_z^3} \tag{A.9}$$

where D_x and D_z are the rigidities. To calculate the reduction factor for the buckling of the web, it is considered as an orthotropic plate having them as rigidity values. They are calculated for $D_x << D_z$ condition as follows.

$$D_x = \frac{E t_w^3}{12(1-\nu^2)} \frac{w}{s} \tag{A.10}$$

$$D_z = \frac{E I_z}{w} \tag{A.11}$$

where I_z is the second moment of inertia of a profiled section w. It is formulated in two ways in two different resources. The first resource is SINBEAM [86] document as mentioned before. According to that I_z can be calculated using the equation given below.

$$I_z = \int_0^w \left(\frac{1}{12} t_w^3 + t_w \left[\frac{a}{2} sin\left(\frac{2\pi x}{w} \right) \right]^2 \right) dx \tag{A.12}$$

Except Eq. A.12, Timoshenko and Woinowsky-Krieger [91] formulated I_z as follows.

$$I_z = \frac{a^2 t_w}{8} \left[1 - \frac{0.81}{1 + 2.5\left(\frac{a}{4w}\right)^2} \right] \tag{A.13}$$

APPENDIX B: BEAMS UNDER THREE-POINT BENDING

As in this study, beams under three-point bending with a concentrated load at their center have the same shear reaction forces along the beam in absolute value and linearly increasing moments towards the center. To be understood clearly, a general schema is given below.

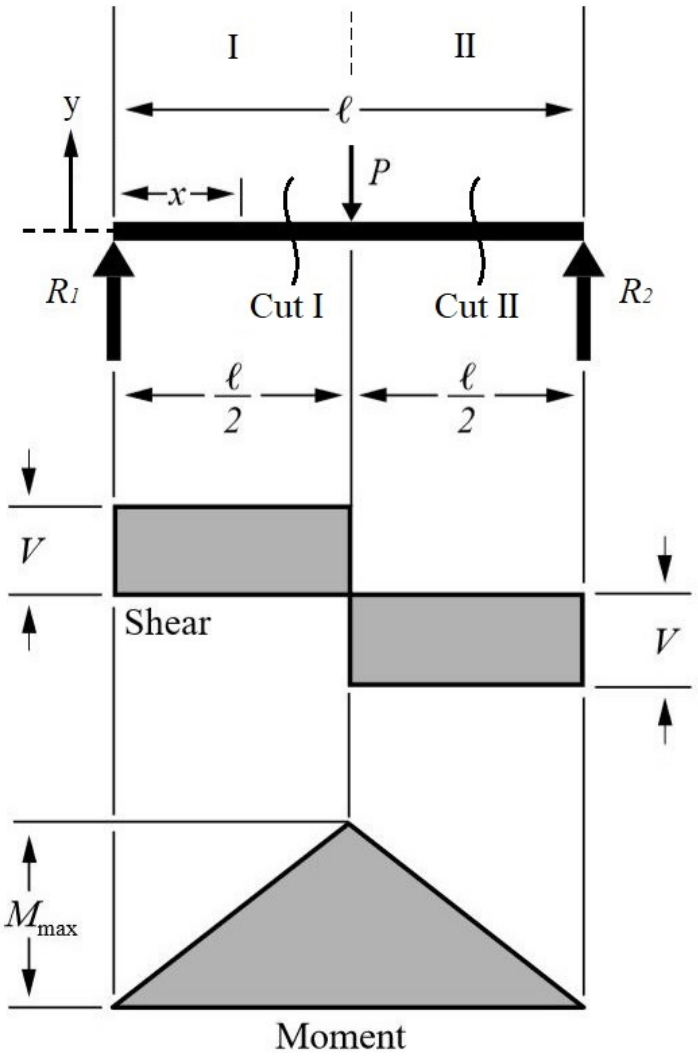

Figure B.1. Shear-moment diagram of beams under three-point bending with force applied from the center [92].

P is the concentrated load applied from the center of the beam, R_1 and R_2 values are the reaction forces of the supports in the y-direction, ℓ is the length of the beam, and V and M are the sectional shear force and moment, respectively.

Total forces and moments in all directions have to be 0 in static systems. Otherwise, the systems begin to move. By using this rule, sectional shear forces and moments can be calculated.

Initially, reaction forces of the supports are calculated as follows.

$$\sum F_y = 0 \tag{B.1}$$

$$R_1 + R_2 - P = 0 \tag{B.2}$$

$$R_1 + R_2 = P \tag{B.3}$$

If the second support point is handled as reference point for moment calculations, the following equations are obtained.

$$\sum M_z = 0 \tag{B.4}$$

$$R_1\ell - P\frac{\ell}{2} = 0 \tag{B.5}$$

$$R_1\ell = P\frac{\ell}{2} \tag{B.6}$$

$$R_1 = \frac{P}{2} \tag{B.7}$$

If R_1 is replaced with $P/2$ in Eq. B.3, R_2 can be found as follows.

$$\frac{P}{2} + R_2 = P \tag{B.8}$$

$$R_2 = \frac{P}{2} \tag{B.9}$$

As a result, reaction forces are found equal to each other due to their equal distances to the applied load. Therefore, they are handled as R after now.

To find the sectional shear force and moment, the beam is considered as cut through the height from the region I as presented in Figure B.1 firstly. The new part is given in the figure below.

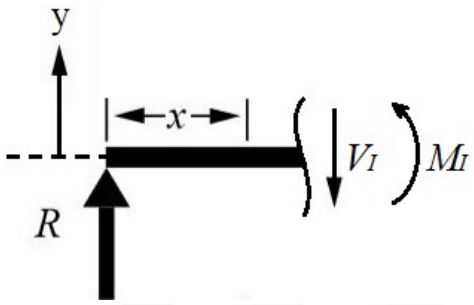

Figure B.2. Sectional shear force and moment of the beam after being cut from the region I.

As seen in Figure B.2, there are two forces R and V_I, and a moment M_I acting on the beam. V_I and M_I are the sectional shear force and moment in the first region of the beam. Calculation of their values is given step by step below.

$$\sum F_y = 0 \tag{B.10}$$

$$R - V_I = 0 \tag{B.11}$$

$$V_I = R \tag{B.12}$$

$$V_I = \frac{P}{2} \tag{B.13}$$

If the location of the reaction force R is considered as the reference point, reaction moment can be calculated as follows.

$$\sum M_z = 0 \tag{B.14}$$

$$V_I x - M_I = 0 \tag{B.15}$$

$$M_I = V_I x \tag{B.16}$$

$$M_I = \frac{P}{2} x \tag{B.17}$$

The other side of the beam is also examined by the second cut. The beam cut by the second point is shown in Figure B.3

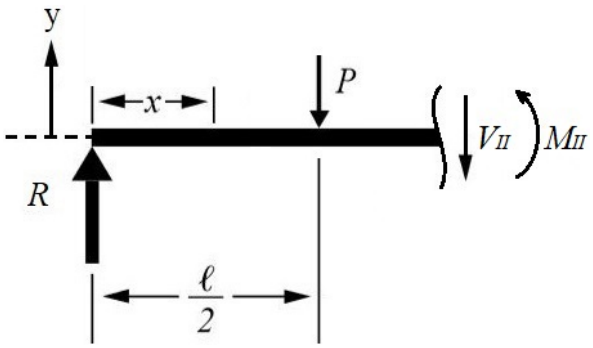

Figure B.3. Sectional shear force and moment of the beam after being cut from the region II.

As can be seen in Figure B.3, there are three forces R, P and V_{II}, and a moment M_{II} acting on the beam. V_{II} and M_{II} are the sectional shear force and moment in the second region of the beam. They are calculated by the equations given below.

$$\sum F_y = 0 \tag{B.18}$$

$$R - P - V_{II} = 0 \tag{B.19}$$

$$V_{II} = R - P \tag{B.20}$$

$$V_{II} = \frac{P}{2} - P \tag{B.21}$$

$$V_{II} = -\frac{P}{2} \tag{B.22}$$

V_{II} is found as $P/2$ with a negative sign because its direction is opposite of the acting concentrated load P. Lastly, the reaction moment in the second region is

calculated by considering the location of the reaction force R as the reference point.

$$\sum M_z = 0 \tag{B.23}$$

$$P\frac{\ell}{2} + V_{II}x - M_{II} = 0 \tag{B.24}$$

$$M_{II} = P\frac{\ell}{2} + V_{II}x \tag{B.25}$$

$$M_{II} = P\frac{\ell}{2} - \frac{P}{2}x \tag{B.26}$$

$$M_{II} = \frac{P}{2}(\ell - x) \tag{B.27}$$

APPENDIX C: FLOWCHART OF THE OPTIMIZATION ALGORITHM

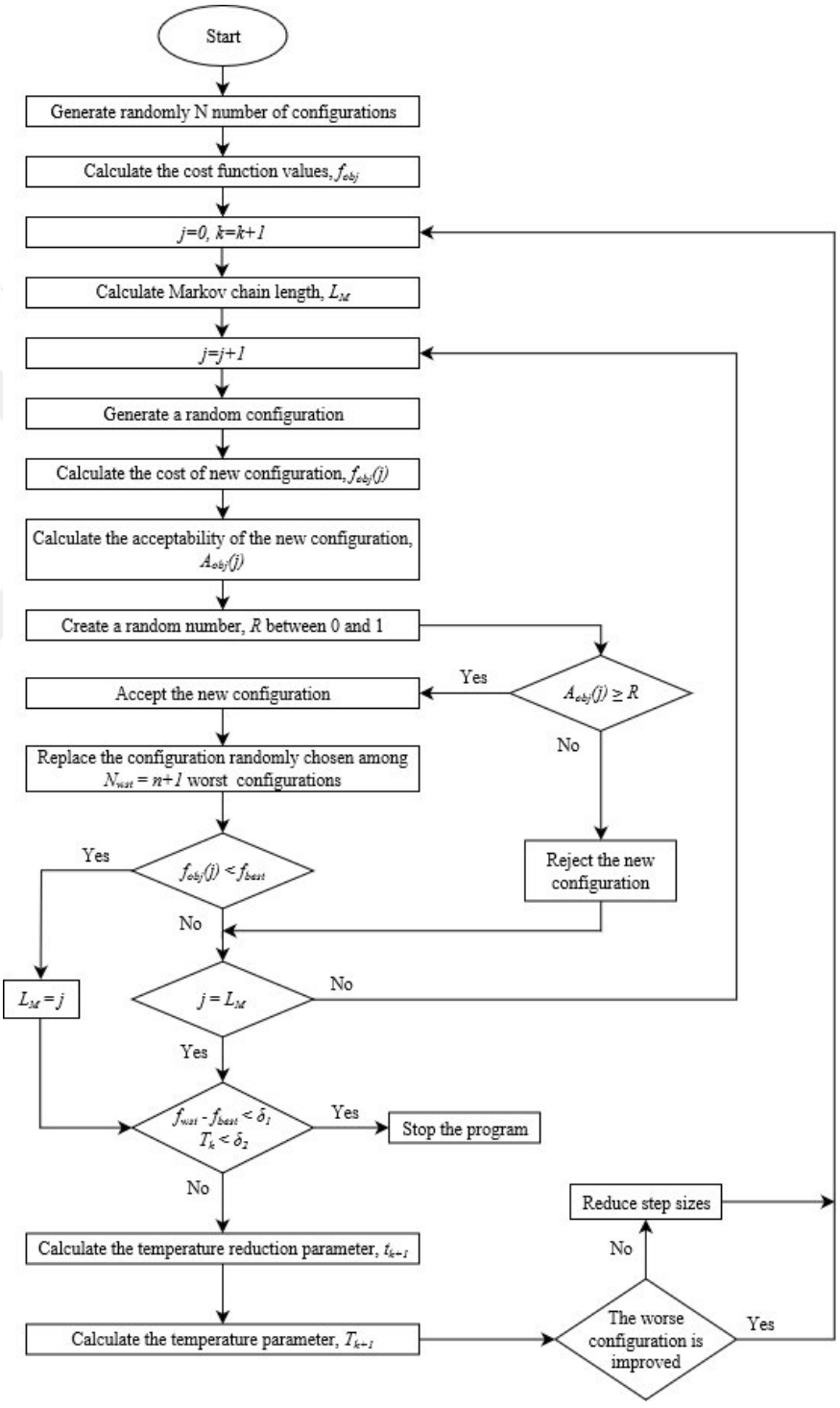

Figure C.1. Flowchart of the optimization algorithm [93].

APPENDIX D: MANUFACTURING

Fischer *et al.* [94] developed an automated production technique for carbon-fiber reinforced composite I-beams with a corrugated web. It can be adapted to manufacture the optimized wing spar.

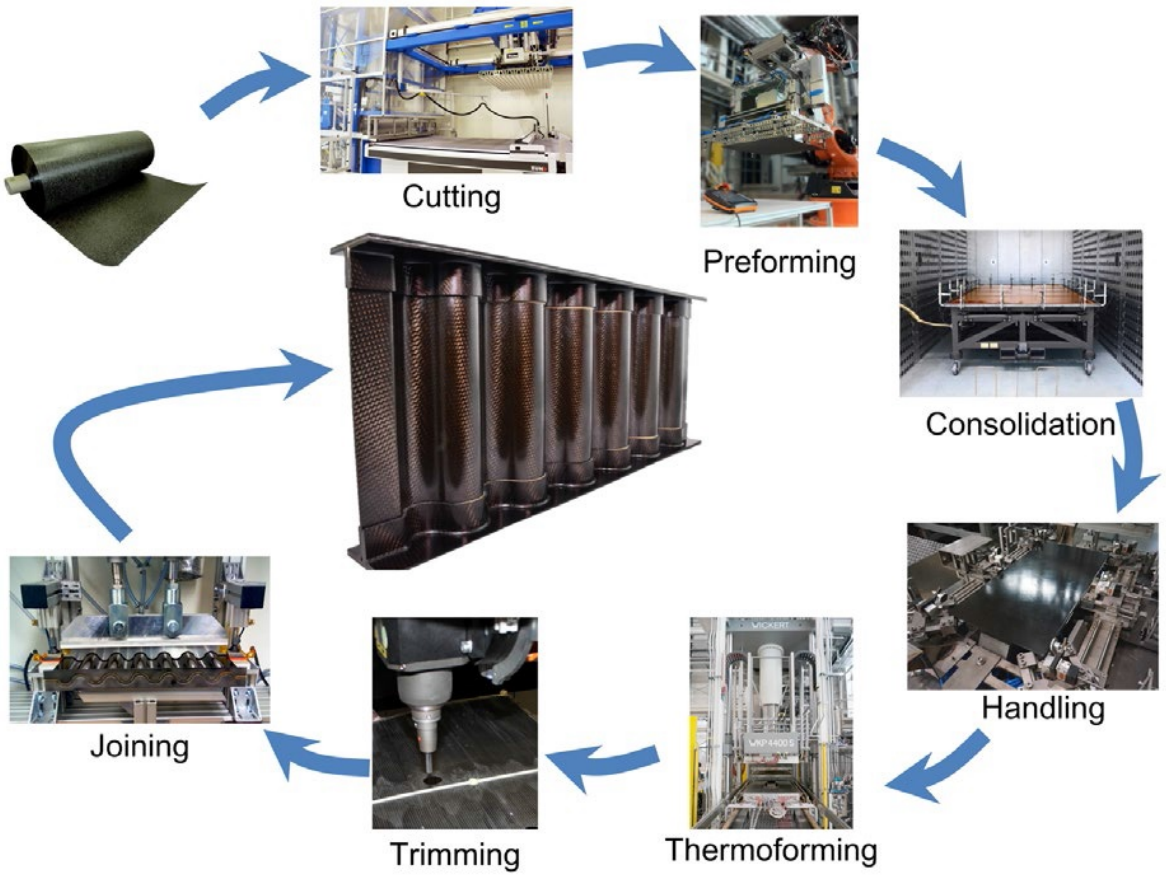

Figure D.1. All manufacturing phases of a carbon-fiber reinforced composite I-beam with corrugated web [94].

As seen in Figure D.1, the production begins with cutting the carbon-fiber fabric. After this process, plies of thermoplastic prepregs are stacked and locally joined by using the ultrasonic spot welding. Then, a vacuum consolidation process is applied by stacking the materials as in Figure D.2.

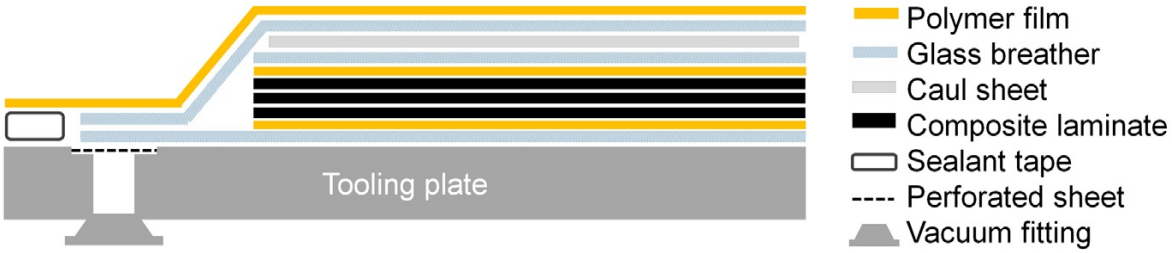

Figure D.2. Vacuum bag setup for consolidation process [94].

Before the last stage assembly, the press forming is performed as a combination of more than one substep as presented in Figure D.3.

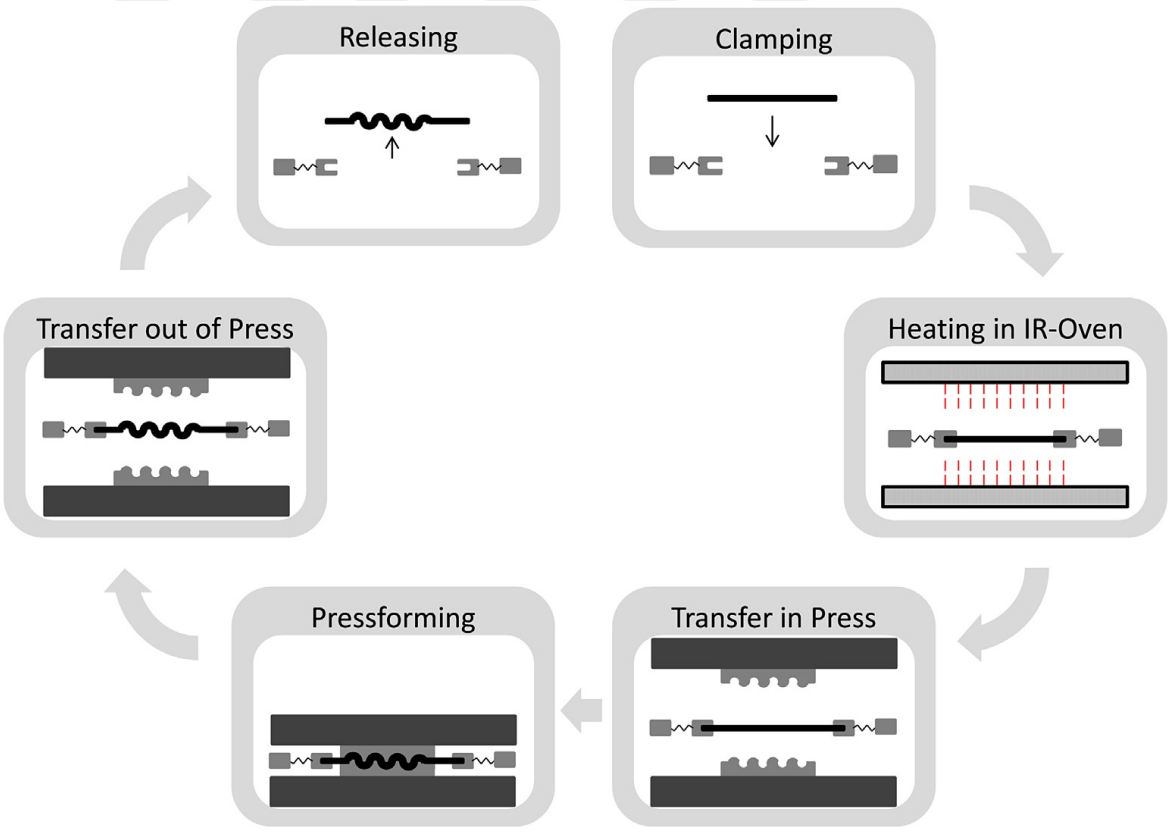

Figure D.3. Press forming process diagram [94].

At last, all the parts including the joint elements made of carbon fiber-reinforced polyetherimide, can be seen in Figure D.4, are assembled using edge links.

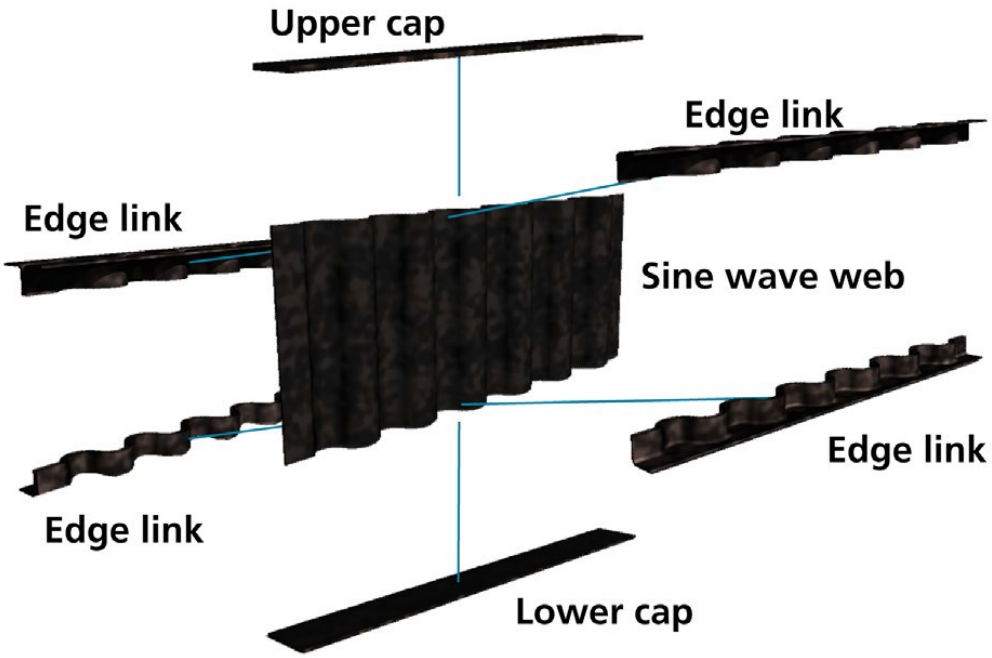

Figure D.4. Components of the beam [94].

The final product is shown in Figure D.5



Figure D.5. Final product [94].

The press mold can be adapted to the optimized beam web shape and edge links can also easily be manufactured using 3D printing methods.